

# UC Merced

## UC Merced Electronic Theses and Dissertations

### Title

A Multi-Faceted Approach to Improving the Tribological Performance of Sliding Contacts

### Permalink

<https://escholarship.org/uc/item/5xr5j402>

### Author

Vellore, Azhar

### Publication Date

2021

### Copyright Information

This work is made available under the terms of a Creative Commons Attribution-NonCommercial-NoDerivatives License, available at <https://creativecommons.org/licenses/by-nc-nd/4.0/>

Peer reviewed|Thesis/dissertation

University of California, Merced

A Multi-Faceted Approach to  
Improving the Tribological  
Performance of Sliding Contacts

by

Azhar Vellore

A dissertation submitted in partial satisfaction of the  
requirements for the degree of  
Doctor of Philosophy

In

Mechanical Engineering

Committee in charge:

Professor Ashlie Martini, Advisor  
Professor Mehmet Z. Baykara  
Professor Min Hwan Lee  
Professor James Palko

© 2021 Azhar Vellore  
All rights are reserved.

This dissertation of Azhar Vellore is approved:

---

Ashlie Martini, Advisor

Date

---

Mehmet Z. Baykara

Date

---

Min Hwan Lee

Date

---

James Palko

Date

University of California, Merced

© 2021 Azhar Vellore



I dedicate this dissertation to my beautiful daughter, my supportive wife, my dear brother and my loving parents without whom I could not have accomplished this mammoth undertaking.

# CURRICULUM VITAE

## EDUCATION

- M.S. Mechanical Engineering, State University of New York at Buffalo, 2015
- B. Tech Mechanical Engineering, VIT University, Vellore, India, 2008

## PUBLICATIONS

- Azhar Vellore, Sergio Romero Garcia, Duval A Johnson, and Ashlie Martini. “Ambient and Nitrogen Environment Friction Data for Various Materials Surface Treatments for Space Applications”. In: *Tribology Letters* 69.10 (2021).
- Yongfeng Li, Chaoji Chen, Jianwei Song, Chunpeng Yang, Yudi Kuang, Azhar Vellore, Emily Hitz, Mingwei Zhu, Feng Jiang, Yonggang Yao, et al. “Strong and Superhydrophobic Wood with Aligned Cellulose Nanofibers as a Waterproof Structural Material”. In: *Chinese Journal of Chemistry* (2020).
- Azhar Vellore, Sergio Romero Garcia, Nicholas Walters, Duval A Johnson, Andrew Kennett, Matthew Heverly, and Ashlie Martini. “Ni-Doped MoS<sub>2</sub> Dry Film Lubricant Life”. In: *Advanced Materials Interfaces* 7.22 (2020), p. 2001109.
- Tian Li, Yao Zhai, Shuaiming He, Wentao Gan, Zhiyuan Wei, Mohammad Heidarinejad, Daniel Dalgo, Ruiyu Mi, Xinpeng Zhao, Jianwei Song, Jiaqi Dai, Chaoji Chen, Ablimit Aili, Azhar Vellore, Ashlie Martini, Ronggui Yang, Jelena Srebic, Xiaobo Yin, and Liangbing Hu. “A radiative cooling structural material”. In: *Science* 364.6442 (2019), pp. 760–763.
- Azhar Vellore, Nicholas Walters, and Ashlie Martini. “Grease Lubrication of Self-Mated 60NiTi Bearing Materials”. In: *Frontiers in Mechanical Engineering* 5 (2019), p. 13.
- Yubing Zhou, Chaoji Chen, Shuze Zhu, Chao Sui, Chao Wang, Yudi Kuang, Upamanyu Ray, Dapeng Liu, Alexandra Brozena, Ulrich H Leiste, Nelson Quispe, Hua Guo, Azhar Vellore, Hugh A Bruck, Ashlie Martini, Bob Foster, Jun Lou, Teng Li, and Hu Liangbing. “A printed, recyclable, ultra-strong, and ultra-tough graphite structural material”. In: *Materials Today* 30 (2019), pp. 17–25.
- Lelia Cosimbescu, Azhar Vellore, Uma Shantini Ramasamy, Samantha A Burgess, and Ashlie Martini. “Low molecular weight polymethacrylates as multi-functional lubricant additives”. In: *European Polymer Journal* 104 (2018), pp. 39–44.
- Jun Liu, Sergey Suslov, Azhar Vellore, Zhencheng Ren, Auezhan Amanov, Young-Sik Pyun, Ashlie Martini, Yalin Dong, and Chang Ye. “Surface nanocrystallization by ultrasonic nano-crystal surface modification and its effect on gas nitriding of Ti6Al4V alloy”. In: *Materials Science and Engineering: A* 736 (2018), pp. 335–343.
- Laura Pen˜a-Para´s, Hongyu Gao, Demo´filo Maldonado-Corte´s, Azhar Vellore, Patricio Garcia-Pineda, Oscar E Montemayor, Karen L Nava, and Ashlie Martini. “Effects of substrate surface roughness and nano/micro particle additive size on friction and wear in lubricated sliding”. In: *Tribology International* 119 (2018), pp. 88–98.

- Jianwei Song, Chaoji Chen, Shuze Zhu, Mingwei Zhu, Jiaqi Dai, Upamanyu Ray, Yiju Li, Yudi Kuang, Yongfeng Li, Nelson Quispe, Yonggang Yao, Amy Gong, Ulrich H Leiste, Hugh A Bruck, Jy Zhu, Azhar Vellore, Heng Li, Marilyn L Minus, Zheng Jia, Ashlie Martini, Teng Li, and Liangbing Hu. “Processing bulk natural wood into a high-performance structural material”. In: *Nature* 554.7691 (2018), pp. 224–228

## PRESENTATIONS

- Wear Life of Ni-doped MoS<sub>2</sub> Dry Film Lubricants for Space Applications - Oral Presentation at STLE Annual Meeting, May 2021.
- Tribology for Space Applications - Invited speaker at Materials and Biomaterials Science and Engineering (MBSE) graduate group at UC Merced, Sep 2020.
- How to Lubricate Mechanisms in Space - Online Poster and short talk at WeSST (Web Seminar Series on Tribology), Jun 2020.
- Investigating Wear Mechanisms of MoS<sub>2</sub> Dry Film Lubricant - Oral Presentation at STLE Virtual Students Conference, May 2020.
- Grease Lubrication of Self-Mated 60NiTi Bearing Materials - Poster presentation at STLE Annual Meeting, May 2019.
- Surface Engineering for Low Friction and Wear - Oral presentation at STLE Northern California Section Meeting, Jun 2018.
- Lubricated Sliding of Textured Surfaces with Nanoparticle Additives - Poster presentation at STLE Annual Meeting, May 2018.
- Atomistic Modeling and Tribology of Functionalized Silver Nanoparticles as Lubricant Additives - Poster presentation at STLE Annual Meeting, May 2017.
- Atomistic Modeling of Cold Sprayed Titanium Coatings - Poster presentation at STLE Annual Meeting, May 2016.

## AWARDS

- 2<sup>nd</sup> Place - UC Merced Grad Slam – March 2021
- UC Merced Graduate Dean’s Dissertation Fellowship – Spring 2021
- 1<sup>st</sup> Place, WeSST Tribology Online Poster Competition – June 2020
- National Science Foundation (NSF) Grant for Research Internship – Oct 2018
- 1<sup>st</sup> Place, Student Poster Competition, STLE 73rd Annual Meeting – May 2018
- Northern California STLE Section Research Scholarship – Spring 2018

# Table of Contents

Curriculum vitae .....	i
List of Figures .....	v
List of Tables .....	ix
Acknowledgements.....	x
Abstract.....	xi
 <b>Chapter 1. Introduction</b> .....	 1
1.1 Tribology .....	1
1.2 Elements of Tribo-Contact.....	2
1.2.1 Surface Properties .....	3
1.2.2 Material Properties .....	7
1.2.3 Lubricating Medium.....	8
1.3 Dissertation outline .....	15
 <b>Chapter 2. Surfaces</b> .....	 18
2.1 Ultrasonic Nanocrystal Surface Modification .....	18
2.2 Electropulsing Assisted Ultrasonic Nanocrystal Surface Modification .....	20
 <b>Chapter 3. New Materials</b> .....	 24
3.1 Introduction.....	24
3.2 60NiTi (Nitinol).....	24
 <b>Chapter 4. Liquid Lubricants</b> .....	 38
4.1 Introduction.....	38
4.2 Multifunctional Polymer Additives.....	38
 <b>Chapter 5. Dry Film Lubricants</b> .....	 44
5.1 Introduction.....	44
5.2 Carbon-based lubricants.....	44
5.3 Polymers .....	45
5.4 Transition metal dichalcogenides (TMDs).....	45
5.5 Undoped and Ni-doped MoS <sub>2</sub> Wear Mechanism Study.....	47

5.5.1 Introduction .....	47
5.5.2 Methodology .....	49
5.5.3 Results and Discussion .....	51
5.5.4 Conclusion.....	62
<b>Chapter 6. Summary and Future Work.....</b>	<b>64</b>
6.1 Summary .....	64
6.2 Future Work.....	66
6.3 Concluding Remarks.....	69
<b>References.....</b>	<b>71</b>

## List of Figures

<b>Figure 1. 1.</b> Wall painting from 1880 B.C. on the Egyptian tomb of Djehutihotep, showing a figure of a person pouring a liquid in front of the sliding statue. ....	1
<b>Figure 1. 2.</b> Generalized model showing the elements of a tribo-contact. ....	2
<b>Figure 1. 3.</b> A typical machine-fabricated surface showing different levels of surface texture [5]. ....	3
<b>Figure 1. 4.</b> (a) Contact at macro and microscale showing interacting asperities. (b) Contact at a single asperity at nanoscale showing atomic interactions. ....	4
<b>Figure 1. 5.</b> Plot showing strong correlation of hardness and wear resistance in metals. ....	5
<b>Figure 1. 6.</b> Plot showing strong correlation between surface energies of many metals and non-metals and their respective hardness. ....	6
<b>Figure 1. 7.</b> Showing a spherical body pushed against a flat surface and released. ...	8
<b>Figure 1. 8.</b> a) Plot showing the effect of fracture toughness on coefficient of friction for a diamond pin on ceramic materials including SiC, Si <sub>3</sub> N <sub>4</sub> , Al <sub>2</sub> O <sub>3</sub> and ZrO <sub>2</sub> (b) Relation between the reciprocal of wear rate and the quantity $Kc^{1/2}H^{5/8}$ for different ceramic materials. ....	9
<b>Figure 1. 9.</b> Plot showing the inverse relationship between different lubricant viscosities and temperature. ....	10
<b>Figure 1. 10.</b> Describing permanent and temporary viscosity loss due to shear induced elongation and scission of a polyalkyl methacrylate (PAMA) molecule model. ....	11
<b>Figure 1. 11.</b> A liquid drop on the left with strong cohesive forces (contact angle, $\theta > 90^\circ$ ) and strong adhesive forces from solid surface ( $\theta < 90^\circ$ ) on the right. ....	12
<b>Figure 1. 12.</b> (a) Hard metal loaded on a soft metal (small $\tau$ , large $A_r$ ). (b) Two similarly hard metals (large $\tau$ , small $A_r$ ). (c) Two similarly hard metals separated by a soft metal film on one surface (small $\tau$ and $A_r$ ). ....	13
<b>Figure 1. 13.</b> Graph showing inverse relationship between coefficient of friction and applied load in the case of indium film on steel substrate. ....	14
 <b>Figure 2. 1.</b> Schematic showing the UNSM process where a pin with hemispherical tip strikes the sample at ultrasonic frequency and scans the entire area. ....	18
<b>Figure 2. 2.</b> Measured (a) scratch hardness and (b) scratch depth, after scratch tests at 1 N normal load. ....	19
<b>Figure 2. 3.</b> Schematic showing electropulsing-assisted UNSM process. ....	20
<b>Figure 2. 4.</b> Wear scars from each specimen type (a) Control (b) UNSM (c) EP-UNSM. ....	21
<b>Figure 2. 5.</b> (a) Wear volume comparison (b) Wear depth comparison. ....	22
<b>Figure 2. 6.</b> Optical microscopy images of NiTi cross-sections from different specimen types. Image courtesy: University of Akron. ....	23
 <b>Figure 3. 1.</b> Schematic diagram illustrating the wear calculation for a flat wear scar. ....	28

<b>Figure 3. 2.</b> Schematic diagram illustrating wear calculation for the ball samples..	28
<b>Figure 3. 3.</b> Test results for SKF LGMT2 including (a) friction traces, (b) interferometer image of the ball wear scar, (c) and (d) optical microscope and interferometer images of the flat wear scar, and (e) and (f) SEM micrographs of flat wear scar. All wear images correspond to the test shown in blue in (a). .....	29
<b>Figure 3. 4.</b> Test results for Braycote 601EF including (a) friction traces, (b) interferometer image of the ball wear scar, and (c) and (d) optical microscope and interferometer images of the flat wear scar. All wear images correspond to the test shown in blue in (a). .....	31
<b>Figure 3. 5.</b> Test results for Braycote 602EF including (a) friction traces, (b) interferometer image of the ball wear scar, (c) and (d) optical microscope and interferometer images of the flat wear scar, and (e) and (f) SEM micrographs of flat wear scar. All wear images correspond to test shown in blue in (a).....	32
<b>Figure 3. 6.</b> Test results for Rheolube 374A including (a) friction traces, (b) interferometer image of the ball wear scar, (c) and (d) optical microscope and interferometer images of the flat wear scar, and (e) and (f) SEM micrographs of flat wear scar. All wear images correspond to the test shown in red in (a). .....	33
<b>Figure 3. 7.</b> Test results for Rheolube 2000including (a) friction traces, (b) interferometer image of the ball wear scar, and (c) and (d) optical microscope and interferometer images of the flat wear scar. All wear images correspond to the test shown in black in (a). .....	34
<b>Figure 3. 8.</b> Wear volume averaged over the three 30 m test for each grease as measured from the (a) flat and (b) ball. Error bars reflect the standard error of three tests. ....	35
 <b>Figure 4. 1.</b> Average COF for each sample where the error bars represent the standard deviation of the results from multiple tests. ....	41
<b>Figure 4. 2.</b> Average wear volume for each sample where the error bars represent the standard deviation. ....	42
 <b>Figure 5. 1.</b> Crystal structure of graphite showing ABAB stacking [35]. ....	44
<b>Figure 5. 2.</b> Showing aerospace components coated with MoS <sub>2</sub> based DFL, Microseal 200-1.....	46
<b>Figure 5. 3.</b> SEM micrographs of a) undoped and b) Ni-doped MoS <sub>2</sub> coating morphologies showing columnar structures consistent with Type I coatings and flat tops resulting from burnishing. ....	51
<b>Figure 5. 4.</b> Representative CoF traces at a) 300 MPa and 1 ms <sup>-1</sup> , b) 500 MPa and 0.77 ms <sup>-1</sup> , c) 800 MPa and 0.44 ms <sup>-1</sup> , and d) 1100 MPa at 0.1 ms <sup>-1</sup> for undoped and Ni-doped MoS <sub>2</sub> coatings run until coating failure. ....	52
<b>Figure 5. 5.</b> EDS compositional maps showing partially worn (left wear track), unworn (center region), and fully worn (right wear track) regions of undoped MoS <sub>2</sub> coating. The partial and fully worn tracks were generated in sliding tests at 300 MPa contact pressure after 18000 and 80000 cycles, respectively. ....	53

<b>Figure 5. 6.</b> EDS compositional maps showing two fully worn wear tracks and unworn regions on a Ni-doped MoS <sub>2</sub> coating. The left and right tracks were generated in sliding tests at 500 MPa contact pressure after 34 000 and 43 000 cycles, respectively. ....	53
<b>Figure 5. 7.</b> Wear life of undoped and Ni-doped MoS <sub>2</sub> at different contact pressure/sliding speed conditions. The results are plotted against pressure on the abscissa, but the speed is also different for each case. Ni dopant improves wear life compared to the undoped samples at low pressures. ....	54
<b>Figure 5. 8.</b> Wear profiles for (a) undoped MoS <sub>2</sub> at 300 MPa and 1 ms <sup>-1</sup> , b) undoped MoS <sub>2</sub> at 1100 MPa and 0.1 ms <sup>-1</sup> , c) Ni-doped MoS <sub>2</sub> at 300 MPa and 1 ms <sup>-1</sup> , and d) Ni-doped MoS <sub>2</sub> at 1100 MPa and 0.1 ms <sup>-1</sup> showing the evolution of the wear tracks during the run-in tests. ....	55
<b>Figure 5. 9.</b> Wear depth as a function of cycle during run-in tests at 300 and 1100 MPa contact pressures on undoped and Ni-doped MoS <sub>2</sub> . Wear tracks are shallower (less wear) on the Ni-doped sample at both pressures. ....	56
<b>Figure 5. 10.</b> SEM micrographs of (a) undoped and (b) doped MoS <sub>2</sub> coatings after 10 cycles at 1100 MPa and 0.1 ms <sup>-1</sup> . The images on the right show close-up views of the partially worn material. These images show representative features where the undoped coatings exhibit cracking and delamination. ....	57
<b>Figure 5. 11.</b> SEM micrographs of the regions between the cracked or delaminated columnar zone for a) undoped and b) Ni-doped MoS <sub>2</sub> coating after 10 cycles at 1100 MPa and 0.1 ms <sup>-1</sup> . The material underneath the failed columnar zone is distinctly rougher for the Ni-doped coating. ....	58
<b>Figure 5. 12.</b> SEM micrographs of dense flakes of MoS <sub>2</sub> within or near the wear track from run-in tests of (a, b) Ni-doped coatings after 10 cycles, c) an undoped coating after 250 cycles, and d) a Ni-doped coating after 250 cycles. All images from tests at 1100 MPa and 0.1 ms <sup>-1</sup> . ....	59
<b>Figure 5. 13.</b> Wear width as a function of cycle during run-in tests at 300 and 1100 MPa contact pressures on undoped and Ni-doped MoS <sub>2</sub> . Wear tracks widths are larger at the higher pressures. In all cases, the width increases gradually with sliding cycles. ....	60
<b>Figure 5. 14.</b> (a) Average lateral force during progressive load scratch tests on doped and undoped samples. Lines represent the average of three tests and the band represents standard deviation. SEM images and Mo/Fe signals from EDS taken at the start of the test on (b) undoped (c) Ni-doped coatings. ....	61
<b>Figure 5. 15.</b> SEM micrographs of a) undoped and b) Ni-doped MoS <sub>2</sub> coatings during a representative progressive load scratch test (at ≈ 62 N load). The doped and undoped coatings are distinctly different at the edges of the wear tracks (e.g., the regions identified by the dashed lines). ....	62
<b>Figure 5. 16.</b> Schematic illustration of the proposed wear process that occurs through densification followed by cracking and, for Ni-doped MoS <sub>2</sub> , delamination. The flakes generated during the cracking and/or delamination process lubricate the contact subsequently as they are continuously supplied as the wear track widens and more flakes are made available to facilitate sliding. ....	62



<b>Figure 6. 1.</b> (a) CAD Model of the controlled environment chamber. (b) Final assembly after retrofitting on tribometer including all peripherals. ....	67
<b>Figure 6. 2.</b> Pin-on-disk sliding tests on Ni-doped MoS <sub>2</sub> showing the effect of nitrogen environment on the friction coefficient compared with ambient air tests with and without the chamber.....	68
<b>Figure 6. 3.</b> Interferometry data of the wear track from nitrogen environment test showing wear depth after 200K cycles, in comparison to the coating thickness. ....	68

## List of Tables

<b>Table 1.</b> Summary of greases used in this study. ....	27
<b>Table 2.</b> Specific wear rates calculated from 30 m tests. ....	36
<b>Table 3.</b> Polymer analog and benchmark solutions studied in this research. ....	40
<b>Table 4.</b> Experimental parameters used in the ball-on-disk tests.....	50

## ACKNOWLEDGEMENTS

I would like to express my sincere gratitude to my advisor and mentor, Professor Ashlie Martini, for supporting and guiding me through this work. She is not only an educator with expertise in tribology and mechanical design but also a thorough professional, who has taught me the importance of time management, public speaking, communication skills and most importantly staying focused.

Duval Johnson, a former graduate student of Professor Martini has been a wonderful colleague and collaborator with a wealth of mechanical engineering knowledge and experience. I will always cherish the discussions, technical and otherwise I had with him during the course of my PhD.

I would like to thank Tushar Khosla (Application Scientist, Rtec Instruments) and Geetanjan Bhandari (Application Engineer, Rtec Instruments) for their wonderful support with diagnosing tribometer issues and quick turn around with repair and resolution. Also, huge thanks to Vishal Khosla, CEO of Rtec Instruments for the amazing opportunity to intern at Rtec.

My sincere thanks to Professor Mehmet Baykara and Professor David Strubbe for their valuable suggestions and insights during my MoS<sub>2</sub> research.

And lastly, thanks to Martini Research Group members Mickael Ades, Nicholas Walters, Sergio Romero Garcia, Arash Khajeh, Rimei (Amanda) Chen, Mohammad Vazirisereshk, Xiaoli Hu and Uma Shantini Ramasamy for being a wonderful company and making this journey enjoyable!

# **A Multi-Faceted Approach to Improving the Tribological Performance of Sliding Contacts**

Azhar Vellore, Ph.D.

University of California, Merced, 2021

Advisor: Professor Ashlie Martini

As we strive to increase the energy efficiency of mechanical systems, it is necessary to find different avenues to reduce energy losses. Sliding contacts are part of most mechanical systems, and they are a major source of energy dissipation due to friction and wear. Sliding friction and wear can be mitigated using a multitude of strategies, including advanced surface modification techniques, new materials that exhibit better mechanical properties and novel lubricants (both liquid and solid). In this dissertation, new approaches to each of these strategies were studied using tribological experiments at application-relevant conditions. In the advanced surface modification strategy, surface properties of Ultrasonic Nanocrystalline Surface Modified (UNSM) Ti6Al4V alloy were characterized, revealing improved scratch resistance. Also, wear tests on Electropulsing-assisted UNSM treated NiTi alloy revealed improved wear resistance compared to untreated alloy. In the new materials strategy, the friction and wear performance of 60NiTi, a relatively new material exhibiting excellent hardenability, elastic recovery, and corrosion resistance, especially suited for space applications, was studied and its performance was characterized in the presence of various greases. This study provided a necessary first step to a complete evaluation of the friction and wear performance of self-mated 60NiTi contacts. In the liquid lubricants approach, novel liquid lubricants with low molecular weight polyalkylmethacrylate additives functioning as viscosity index improvers, friction modifiers and anti-wear additives were studied for their tribological performance. Their friction performance was found to be on par with two commercial benchmarks, an anti-wear additive and a fully-formulated oil, obviating the need to add dedicated friction modifiers, potentially leading to cheaper lubricants. And, lastly, in the solid lubricants approach, the wear life of undoped and Ni-doped sputtered MoS<sub>2</sub> coatings was investigated in ambient air conditions. Ni-doped MoS<sub>2</sub> coatings outlasted their undoped counterpart particularly at low pressures, where a delamination-driven debris formation was found to favor longer wear life in Ni-doped coatings. Also wear evolution during run-in revealed that both undoped and Ni-doped MoS<sub>2</sub> appear to wear through the coating thickness at the center of the contact very early on, but microstructural studies revealed that new lubricious debris generated from the sides of the wear track provided continuous lubrication until the coatings failed much later. Overall, this research evaluated the performance and investigated the mechanisms of novel techniques to improve friction and wear behavior of tribological contacts using experimental methods. The results demonstrated viability of these techniques for enabling better energy efficiency in many different possible applications.

# Chapter 1. Introduction

## 1.1 Tribology

Tribology is the study of friction, lubrication, and wear. The word tribology is relatively new, first coined by Professor H. Peter Jost in 1966, derived from the Greek word *tribos* which translates to *rubbing*. Although the term is new, the concept itself dates back to 3<sup>rd</sup> millennium BC [1] when some form of primitive lubrication was applied to prevent wear of wooden drill sticks used to light fires by rotating against another piece of wood. Another notable example is often

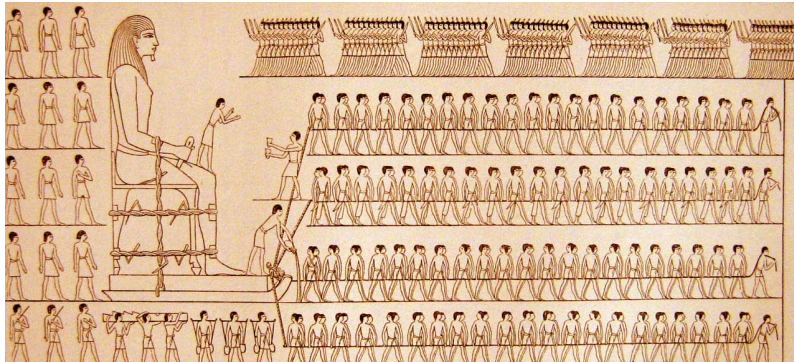


**Figure 1. 1.** Wall painting from 1880 B.C. on the Egyptian tomb of Djehutihotep, showing a figure of a person pouring a liquid in front of the sliding statue.

cited from ancient Egypt, where a tomb drawing [2] shown in Figure 1.1, suggests huge statues were transported by wetting the sand with water.

There are three key aspects of tribology: friction, wear, and

lubrication. Friction is the opposing force experienced when two bodies slide against each other. Due to its opposing nature, a portion of the supplied energy is expended to overcome it. Friction is non-recoverable and is dissipated in the form of heat, noise, or wear of the surfaces in contact. Wear is the gradual deformation or removal of material at the interface of sliding surfaces caused by friction between moving components. It leads to failure of the components and results in the need for replacement of parts. Lubrication is the technique of using a medium to reduce both friction and wear, by creating a separation between the moving surfaces and allowing the components to slide against each other with lower resistance. Modern civilization is filled with moving components, ranging from the crown of a watch to wheels of a car, with application environments ranging from terrestrial to deep space. Overcoming friction and minimizing wear in all these cases has now become so crucial, that our way of life would literally grind to a halt without the methods that led to incremental tribological improvements achieved over the centuries. These methods primarily include modifying surface conditions, formulating better lubricants and developing novel materials employed in a moving interface. Every device, machine or a process which consists of moving components costs extra energy to either overcome friction or to manufacture and replace worn

parts. A massive study undertaken in 2017 [3] found that 23% of global energy consumption originates from tribological contacts and, of that, 20% is used to overcome friction. This not only puts tremendous strain on available energy resources, but also creates large amounts of greenhouse gases which cuts down on our already meagre efforts to curb global warming.

## 1.2 Elements of Tribo-Contact

A tribo-contact is the interface of two surfaces sliding relative to one another. Tribo-contacts may range from a single point contact observed in atomic force microscopy (AFM) at the nano scale to a piston-ring and cylinder contact at the mesoscale. Tribo-contacts may be lubricated or unlubricated and depending on the application, may aim for more friction or less. For example, the goal of an automobile engineer is to increase friction between the surface of a tire and surface of the road for better traction, however, the goal is to reduce friction between pistons and cylinders inside the engine both to burn less fuel and prevent excessive wear and tear of the components. So, in order to design mechanical components which are both energy efficient and long-lasting, it is necessary to understand the elements of a tribo-contact and then, developing techniques to optimize its tribological characteristics to produce best performance for its intended application.

We start by breaking down a tribo-contact, in this case, a sliding interface, into its constituents using a simplified model as described in Figure 1.2.

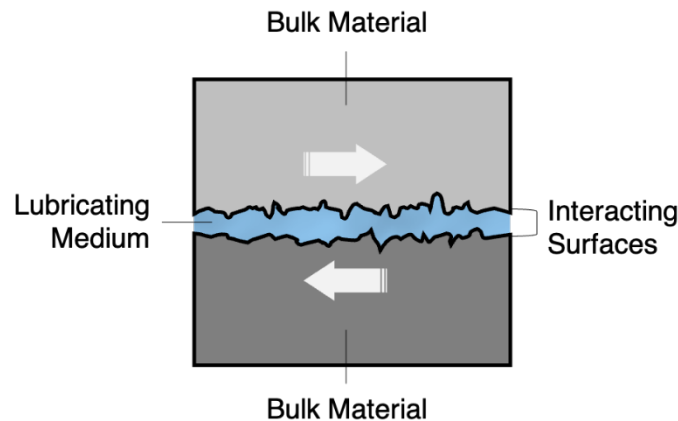


**Figure 1. 2.** Generalized model showing the elements of a tribo-contact.

It consists of two bodies having unique *materials*, with their respective *surfaces* sliding relative to one another with a *lubricating medium* in between them. Each of these constituents i.e., materials, surfaces and lubricant have unique properties which may or may not complement each other and affect the

overall tribological behavior of a contact. Hence, it is first important to discuss and understand these elements to be able to optimize them or find novel strategies to further improve energy efficiency of mechanical systems consisting of such contacts.

### 1.2.1 Surface Properties

All mechanical systems consist of components with interacting surfaces. Surfaces are one of the most important constituents of a tribological contact as that's where any two components come in to contact and the first interaction between any material and its environment takes place. Surface interactions at the component level can be traced down to interactions at the atomic level. The efficiency of a mechanical system depends on the surface interactions between its components and the surface interactions between components depend on their surface properties. These surface properties include but may not be limited to structural or topographic, mechanical and physicochemical properties.

#### 1.2.1.1 Structural or Topographical Properties

Most mechanical components are machine fabricated, which typically generates a unique surface topography or surface texture depending on the machining process. Surface texture is defined as '*repetitive or random deviation from the nominal surface that forms the three-dimensional topography of the surface*' [4]. Surface texture is uniquely defined at different scales i.e., at micro and nanoscales, it is called as roughness and at the macroscale it is called as waviness.

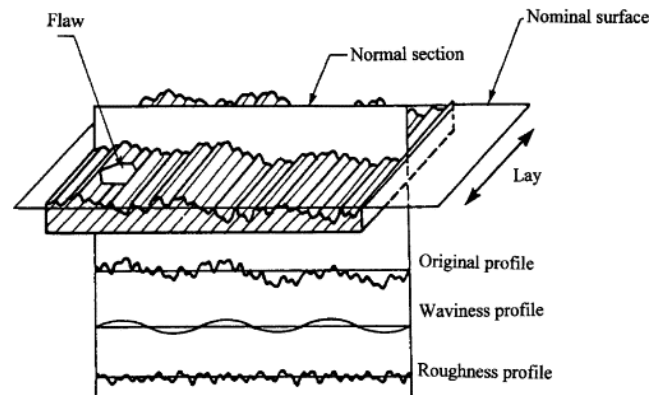


**Figure 1. 3.** A typical machine-fabricated surface showing different levels of surface texture [5].

Roughness consists of hills and valleys (height or amplitude parameters) which are highly local with short wavelengths (spatial parameter) whereas waviness consists of surface deviations with longer wavelengths, see Figure 1.3. Surface

texture also includes lay and flaws, where lay is the primary direction of machining pattern (in machined surfaces) and flaws are unplanned defects in the texture. Machined surfaces appear to be ‘flat’ at macroscale, however, at the micro and nanoscale the topography is very rough. Therefore, the actual interaction between two component surfaces occurs between individual asperities at the microscale and crystallographic planes at the nanoscale respectively as shown in Figure 1.4.

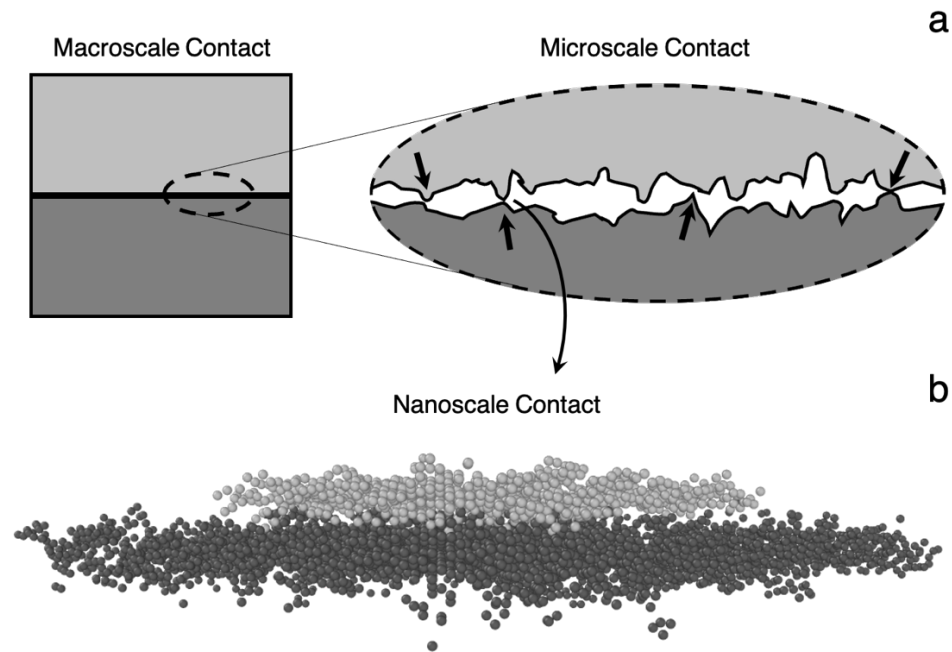


**Figure 1. 4.** (a) Contact at macro and microscale showing interacting asperities. (b) Contact at a single asperity at nanoscale showing atomic interactions.

When a normal load is applied, more and more asperities touch each other some deforming elastically and some plastically. When these surfaces slide relative to one another, adhesion and deformation forces, both resisting motion, develop between the asperities, contributing to the net friction force [6]. Thus, it is generally understood that rougher surfaces result in more asperity-asperity interactions generating greater friction force due to the deformation component of the asperity interactions. However, friction force doesn't monotonously decrease with decreasing roughness because other factors such as the mechanical properties of the materials have a significant effect on friction as well.

### 1.2.1.2 Mechanical Properties

The mechanical properties of materials in a tribo-contact play a significant role in the friction and wear behavior of the tribo-system. These properties include



but are not limited to hardness, modulus of elasticity and elastic limit, fracture toughness and residual stresses.

Hardness of a material is defined as its resistance to plastic deformation brought about locally by indentation or abrasion. It is typically measured by indenting a sample material with a sharp indenter made of diamond or very hard reference material under a fixed normal load and measuring the residual surface area of the impression. The hardness is then calculated as the ratio of the load and residual surface area of the indent. In metals and ceramics, hardness directly affects friction force, i.e., the deformation component of friction is lower when sliding against a harder material. In metals, wear resistance is highly correlated to hardness, see Figure 1.5 [7].

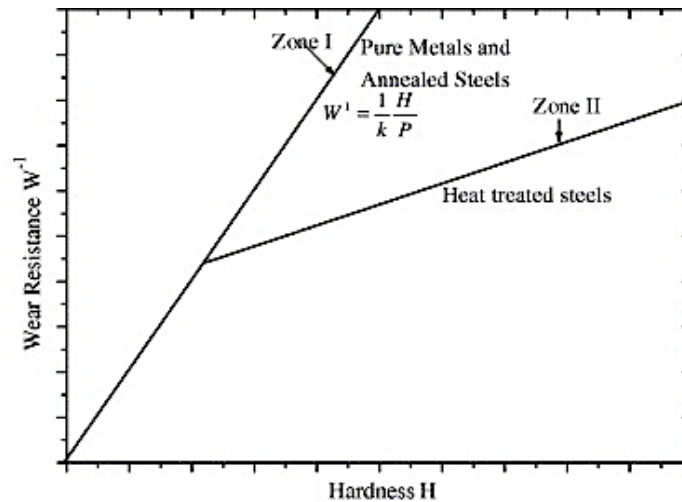
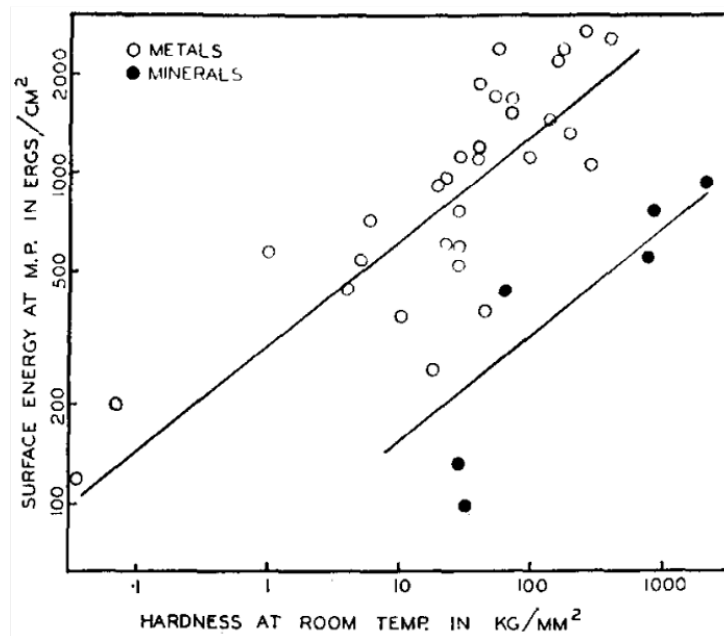


Figure 1. 5. Plot showing strong correlation of hardness and wear resistance in metals.

However, wear resistance does not monotonously increase with hardness, for instance, some ceramics are extremely hard, but have very low fracture toughness, (a measure of resistance to brittle failure) which causes brittle wear. The role of fracture toughness is discussed subsequently. That brings us to one of the most frequently used wear models, referred to as Archard's wear law. According to this, in a single asperity sliding contact, the volume of worn material is proportional to the energy dissipated due to friction forces during sliding [8]. Although originally applicable to adhesive wear modes, it has been extended to model other wear modes including abrasion [9] and fretting wear [10].

Residual stresses are externally induced stresses on the surface of materials typically occurring either during manufacturing processes employed in generating the surface, temperature gradients or structural changes due to phase transformations, to name a few. Residual stresses are generally

classified into tensile and compressive stresses. Tensile stresses are often undesirable because of their tendency to facilitate crack propagation and causing premature failure. Compressive stresses on the other hand are beneficial and often induced intentionally to either reduce tensile stresses or to produce a net compressive residual stress[11]. This is done by different surface treatment methods including shot peening, high pressure torsion, ultrasonic nanocrystalline surface modification (UNSM) etc., which fall under a class of techniques called severe plastic deformation (SPD). These compressive stress inducing techniques are known to improve the wear resistance of surfaces of bulk materials [12] and coatings [13, 14]. However, the effect of SPD on friction coefficient is found to be material dependent [15, 16].



**Figure 1. 6.** Plot showing strong correlation between surface energies of many metals and non-metals and their respective hardness.

### 1.2.1.3 Physicochemical Properties

Surface energy is a physicochemical property which strongly affects other surface phenomena including interfacial adhesion and bonding, and as a result, friction. Surface energy is defined as the energy per unit area required to cleave a solid body, creating two new surfaces [18]. These exposed surfaces consist of unsaturated bonds ready to react with atoms in the bulk or other species in the environment. This reactive nature of surfaces is responsible for different chemical phenomena including, formation of oxide layer due to the presence of atmospheric oxygen, or formation of adhesive bonds with another

surface in contact. Higher surface energy results in stronger bonds with the counter-body during sliding, thus, increasing the adhesive component of friction and in fact, one way lubricants reduce friction is by reducing surface energies of the interacting solids. Interestingly, the surface energies of many metals have been found to be in good correlation to their hardness, see Figure 1.6 [17]. Oxide layers are known to reduce friction and wear at low loads by acting as a lubricating film and protecting the underlying surface from further wear [19]. At high loads or with continuous sliding however, the oxide film gets depleted, causing increased friction subsequently. Additionally, the surface energy also influences chemical reactions at the interface, between the sliding surfaces or between the surfaces and lubricant. These reactions and their by-products if any can be beneficial or detrimental to the tribo-contact depending on the materials involved, load and speed conditions, and environmental factors like temperature and ambient atmosphere. For example, high surface energy is found to induce polymerization reactions in  $\alpha$ -pinene molecules between dehydroxylated silica surfaces, which causes an increase in friction coefficient [20].

### **1.2.2 Material Properties**

The bulk material properties in a tribo-contact significantly affect its tribological behavior. These properties mainly include shear strength, elastic modulus, and fracture toughness.

Shear strength of a material is its ability to resist failure or deformation due to shear forces. Part of the friction forces developed between two surfaces sliding relative to each other is due to shear forces acting on each surface. A direct implication is that materials with low shear strength offer low resistance to deforming forces at the sliding interface resulting in low friction coefficient. Such materials are often used as solid lubricants, for example, polytetrafluoroethylene (PTFE) is a low shear strength polymer exhibiting low coefficient of friction (0.05-0.1) and is mixed with other harder polymers like polyether ether ketone (PEEK) resulting in a material which is both strong and lubricious [21]. However, low shear strength also implies, the material cannot resist shear induced wear, that's why such materials cannot be used as bulk materials for tribo-components.

Modulus of elasticity or Young's modulus of a material is its resistance to deform elastically, quantified by the slope of the linear part of a stress-strain curve. Elastic limit is the maximum stress under which the material can recover elastically, and any further increment in stress will cause permanent deformation. Elastic properties of materials play a major role in a tribo-contact,

more particularly affecting the real area of contact. For example, when a spherical body is pushed against a flat surface and released, the contact area shrinks due to both materials recovering elastically, Figure 1.7 [22].

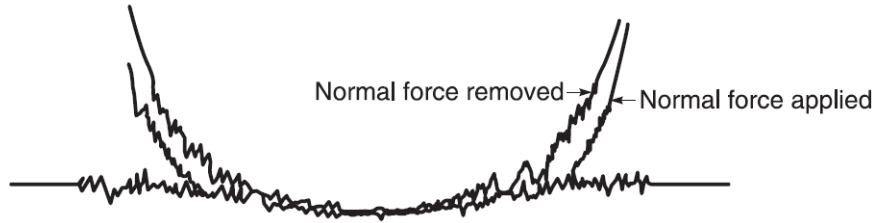


Figure 1. 7. Showing a spherical body pushed against a flat surface and released.

The recovery is smaller in materials with lower modulus and vice versa, implying that the area over which adhesion occurs is strongly influenced by elastic properties of the materials which has direct ramifications for friction and wear.

Fracture toughness (often denoted as  $K_{IC}$ ) is a measure of a material's resistance to brittle failure through crack propagation, during application of external stress. Brittle materials including ceramics, glass and many polymer materials have low fracture toughness allowing cracks to propagate rapidly causing material failure before any significant plastic deformation. Fracture toughness strongly affects the tribological properties of materials, for example, coefficient of friction has been found to decrease sharply with increasing toughness in brittle materials like ceramics, see Figure 1.8(a) [23]. Wear resistance is also a function of fracture toughness in addition to hardness. Higher hardness is not sufficient guarantee for higher wear resistance, as low fracture toughness allows rapid crack growth, eventually causing wear. The plot in Figure 1.8(b) [24] shows a direct relation between the reciprocal of wear rate (wear resistance) at constant load with the quantity  $K_{IC}^{1/2}H^{5/8}$  for different ceramics, implying, for a given hardness, higher toughness causes less wear.

### 1.2.3 Lubricating Medium

Using a lubricating medium to improve relative motion between two bodies in contact is one of the earliest known friction reducing strategies. Lubricants reduce friction force by creating a physical separation between the sliding bodies and enable smooth motion with low friction force. By separating the contacting bodies, they also reduce wear of the materials in contact improving the durability and reducing the occurrence of failure.

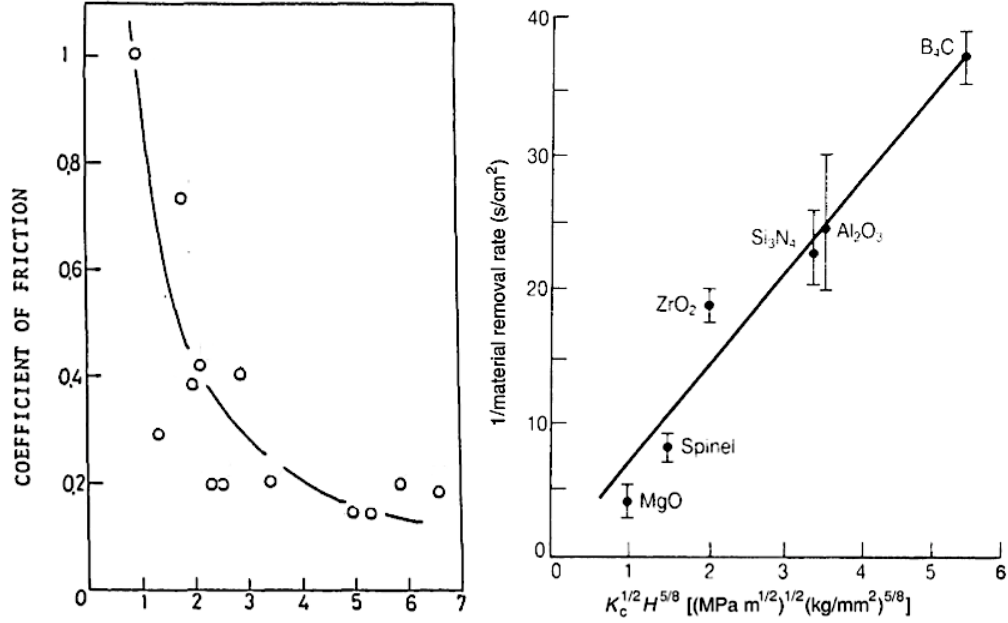


**Figure 1. 8.** a) Plot showing the effect of fracture toughness on coefficient of friction for a diamond pin on ceramic materials including SiC,  $Si_3N_4$ ,  $Al_2O_3$  and  $ZrO_2$  (b) Relation between the reciprocal of wear rate and the quantity  $K_c^{1/2} H^{5/8}$  for different ceramic materials.

Lubricants are currently available in all forms i.e., liquids, solids, and gases. Typical examples of liquid lubricants include mineral oils, vegetable oils and synthetic oils. Solid lubricants are available in power form or semisolids in the form of grease or solid-liquid suspension. Examples include graphite/graphene or molybdenum disulfide ( $MoS_2$ ) powders and coatings, mineral oil greases, silicone greases etc. Gaseous lubricants including Helium, Nitrogen or Air are used to lubricate bearings in some special applications [25]. Our discussion will mainly be confined to liquid and solid lubricants.

### 1.2.3.1 Liquid Lubricants

Liquid lubricants typically consist of more than 90% base oil and remaining 10%, a combination of different additives. Some rheological properties of liquid lubricants strongly affecting their tribological behavior include viscosity, viscosity index, shear stability, volatility, surface tension and oxidation stability. Only some of these properties are addressed by the base oil and for further enhancements, multiple additives specifically targeting different properties are added. In the following paragraphs, we will briefly discuss how some of these rheological properties affect the tribological performance of liquid lubricants.

## Viscosity and Viscosity Index

Viscosity of a lubricant is defined as the resistance to deformation or flow, i.e., a lubricant with low viscosity flows easily compared to a higher viscosity lubricant. In a tribo-contact, lubricant viscosity directly affects its ability to keep the surfaces separated under external load, i.e., higher the viscosity, better the separation ability, which is also referred to as its load bearing ability; therefore, higher viscosity lubricant reduces material contact and as a result friction and wear. So, it is very important that the viscosity is maintained throughout the duty cycle of components. However, viscosity of liquid lubricants (and liquids in general) is temperature dependent, where viscosity decreases with increasing temperature, see Figure 1.9 [26, 27].

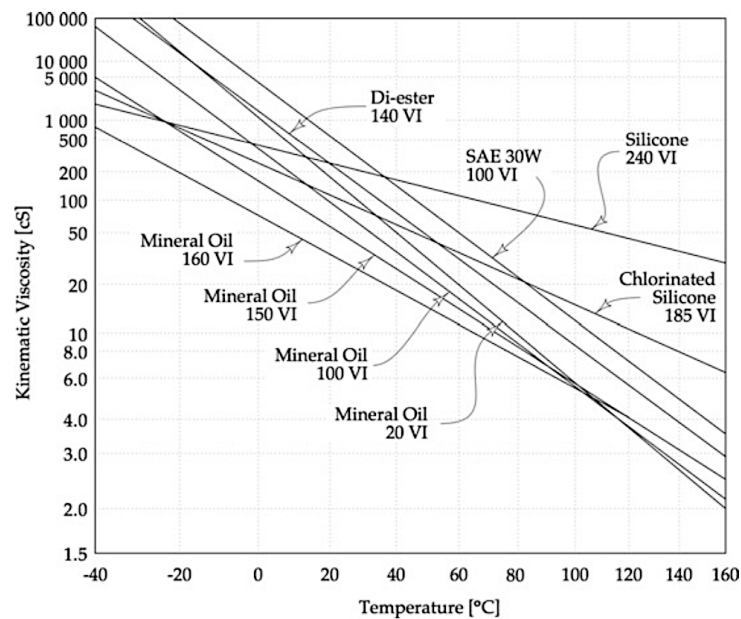


**Figure 1. 9.** Plot showing the inverse relationship between different lubricant viscosities and temperature.

Most oil lubricated mechanical systems operate at higher than room temperatures and consequently, the lubricating oil gradually loses its viscosity either temporarily or permanently during its operation. The reverse also holds true, where decreasing temperatures (in colder geographies, space, or distant planets) increases the viscosity. If the lubricating oil is too thick, for example cold starting a car engine in winter, it might not be able to flow fast enough to lubricate the engine parts in time or the pump requires more power to create enough flow. This might lead to fuel wastage or in extreme cases seizure of critical parts. So, it is of utmost importance to know how much change in viscosity a given lubricant undergoes, for a given change in temperature to

maintain normal operational performance of a mechanical system. As shown in Figure 1.9, the rate of viscosity drop with temperature varies from lubricant to lubricant, so, to compare the viscosity-temperature stability of different lubricants, a quantity called Viscosity Index (VI) is used. It is a dimensionless quantity which measures a fluid's change in viscosity with respect to a given change in temperature. Higher VI indicates less tendency of the fluid's viscosity to change with temperature, that means more consistency in performance. Between two oils, all other properties being similar, the oil with higher VI is a better choice.

### Shear Stability

Shear stability of polymer-based lubricant is its resistance to shear thinning, i.e., temporary, or permanent viscosity loss at high shear rates. The loss is temporary when the shearing results in changes in the polymer configuration in the lubricant (generally at low shear rates), however, if it leads to scission of polymer chains (at high shear rates), then the loss is permanent as depicted in Figure 1.10 [28].

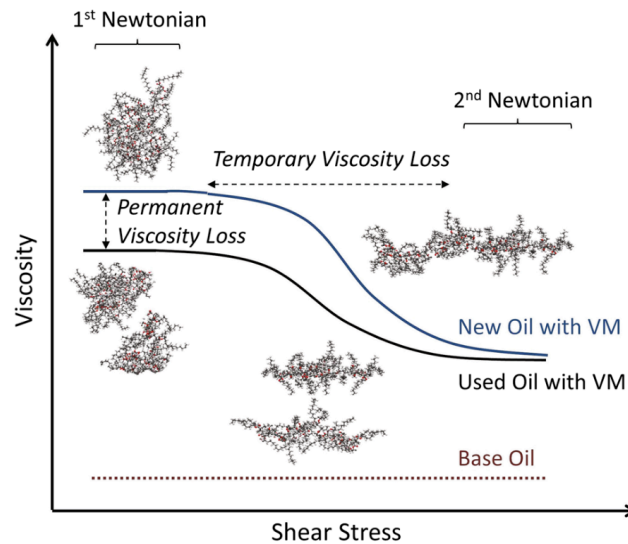


**Figure 1. 10.** Describing permanent and temporary viscosity loss due to shear induced elongation and scission of a polyalkyl methacrylate (PAMA) molecule model.

The permanent viscosity loss is known to be self-limiting i.e., as the polymers break into sufficiently small sizes, there is little further degradation. So, as seen in Figure 1.10, the loss is drastic initially, followed by a slowdown and finally plateauing after a critical polymer chain size/weight is attained. Temporary shear thinning is known to occur through alignment of polymer chains with the flow direction or through disruption of micelles (compact

spheres of polymer chains). This loss of viscosity is reversed when the shear rate is decreased.

### Surface tension and Wettability

Surface tension is the net lateral force per unit length on a liquid's surface molecules, a result of dominant cohesive forces from inner liquid molecules. It gives a liquid the tendency to minimize its surface area. Wetting of a lubricant on solid surfaces is strongly related to its surface tension. Greater the surface tension, greater a liquid's ability to hold its shape and lesser its spread on the solid surface.

Wettability is defined as a liquid's ability to spread and maintain contact with a solid surface. It mainly depends on the net effect of cohesive forces (surface tension) within the liquid and adhesive forces between the liquid and solid [29]. When a liquid drop is in close proximity to another solid, for example, with a stronger affinity (adhesion) for the liquid molecules, the liquid spreads along the solid surface until the cohesive and adhesive forces are balanced; this is referred to as wetting. Instead of spreading over the surface, if the liquid tends to keep a spherical form, it is referred to as non-wetting, see Figure 1.11. [29] Wettability of a lubricant greatly affects its tribological performance. For example, recent studies have revealed that liquid-solid wettability can significantly influence hydrodynamic lubrication behavior at the micro/nano scale [30, 31]. Another study showed that for a lubricant to function well, at least one surface of the tribo-pair should be wettable [32].

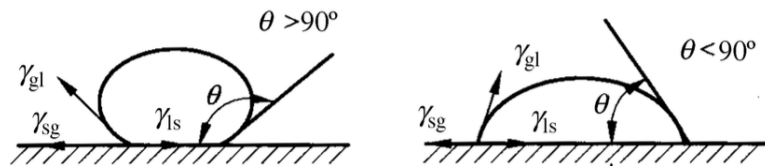


**Figure 1. 11.** A liquid drop on the left with strong cohesive forces (contact angle,  $\theta > 90^\circ$ ) and strong adhesive forces from solid surface ( $\theta < 90^\circ$ ) on the right.

#### 1.2.3.2 Solid Lubricants

Solid lubricants are low-shear strength solids that include soft metals, inorganic, organic and self-lubricating composite materials, which are generally used in the form of coatings, powders or as fillers in a composite [33]. Solid lubricants are used in situations where liquid lubrication is not feasible, including very high/low temperatures, highly corrosive environments or in vacuum conditions like space. They are also used in mechanical systems lacking effective sealing, or with no pumping system for liquid lubricant flow. Examples of some categories of popular solid lubricants include carbon based



(e.g., graphite, diamond-like carbons (DLCs)), transition metal dichalcogenides (e.g., molybdenum disulfide ( $\text{MoS}_2$ ), tungsten disulfide ( $\text{WS}_2$ )), polymers and polymer composites (PTFE and PTFE-polymer composites) and many soft metals (e.g., silver, indium, gold) etc. In addition to low friction and wear, solid lubricants are expected to exhibit a range of other characteristics, including, high strength, thermal and chemical stability, fatigue life, adhesive strength etc.

In the following, we will discuss the theory and analytical equations through which Bowden and Tabor explained solid lubrication on hard elastic materials [34] and the conditions necessary for best tribological performance.

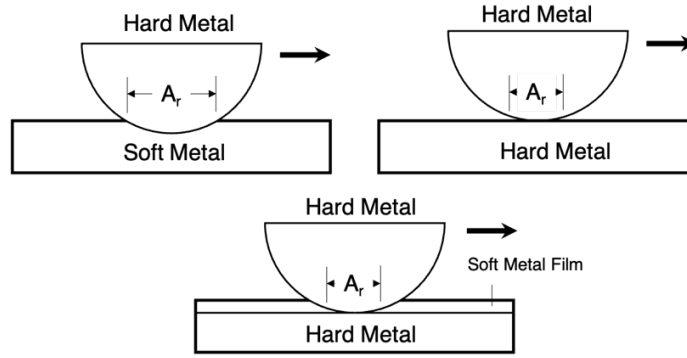


**Figure 1.12.** (a) Hard metal loaded on a soft metal (small  $\tau$ , large  $A_r$ ). (b) Two similarly hard metals (large  $\tau$ , small  $A_r$ ). (c) Two similarly hard metals separated by a soft metal film on one surface (small  $\tau$  and  $A_r$ ).

Now, consider a sliding tribo-pair of hard elastic solids, one of them coated with a solid lubricant having shear strength  $\tau$ , and real contact area,  $A_r$ , between them. Then, for an applied normal load  $L$ , and resulting friction force  $f$ , the coefficient of friction,  $\mu$ , can be written as,

$$\mu = \frac{F}{L} = \frac{A_r \cdot \tau}{L} = \frac{\tau}{P} = \frac{\tau_o}{P} + \alpha \quad (1)$$

where,  $\tau_o$  is the interfacial shear strength and  $\alpha$  is a pressure -dependent parameter pertaining to the shear strength and the lowest possible friction coefficient for a friction pair. According to Eq. 1, the friction coefficient is the ratio of shear strength to contact pressure,  $P$ , and a solid lubricant can reduce the friction coefficient by having a low shear strength  $\tau_o$  and resulting in a higher contact pressure (small contact area,  $A_r$ ). This is illustrated in Figure 1.12 [35]. This model was validated by Bowden and Tabor by showing that indium metal, which is much softer than steel, can act as a solid lubricant.

Another interesting observation from the indium study was that, although both oil lubricated and unlubricated steels showed independence between  $\mu$

and applied load  $L$ , there was a marked decrease in  $\mu$  with increasing  $L$  for indium film on steel as shown by the plot in Figure 1.13.

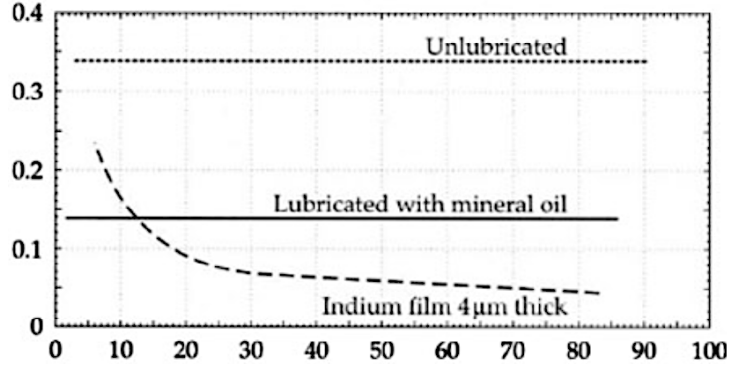


**Figure 1. 13.** Graph showing inverse relationship between coefficient of friction and applied load in the case of indium film on steel substrate.

This behavior is partly explained by the illustration in Figure 1.12, whereby, the increase in friction force due to a modest increase in contact area at higher loads was significantly outweighed by the increase in contact pressure. This was also explained analytically using a Hertzian elastic sphere-on-flat contact model where coefficient of friction can be expressed as,

$$\mu = \tau_o \pi \left( \frac{3R}{4E^*} \right)^{\frac{2}{3}} L^{-\frac{1}{3}} + \alpha \quad (2)$$

where,  $R$  is the radius of sphere and  $E^*$  is the reduced modulus of elasticity. The inverse relationship between  $\mu$  and  $L$  is evident in Eq.2, where  $\mu \propto L^{-1/3}$ . This means, for an elastic contact, friction coefficient will decrease with increasing normal load. This relation has been experimentally verified in multiple solid lubricants including  $\text{MoS}_2$  (doped with  $\text{Sb}_2\text{O}_3$ ), diamond-like nanocomposite (DLN) coatings, ultra-nanocrystalline diamond (UNCD) coatings [35]. So, the best conditions for low friction in solid lubricant coatings is to have a hard substrate to provide load support and keep the contact area small, wherein the coating provides a low shear strength interface. However, this inverse relationship has not been found to hold true at microscopic loads in the order of  $\mu\text{N}$  and  $\text{nN}$ , observed in  $\text{MoS}_2$  [36, 37] and DLN coatings [38].

Another mechanism by which solid lubricants reduce friction and wear is, formation of tribo-film or transfer film on the counter-face. Tribo-films are known to reduce friction and wear by preventing direct contact between the sliding surfaces [39–41] and by a continuous supply of low shear strength material at the interface. Some solid lubricants are known to function without tribo-films, for example, near frictionless carbon (NFC) exhibits ultralow

friction coefficient of  $\sim 0.005$  by passivation of contacting surfaces induced by hydrogenated carbon atoms[42].

Film thickness of solid lubricants is also known to have a significant effect on their tribology. It has been predicted theoretically and verified experimentally [43] that for solid lubricants such as oxides, soft metals and  $\text{MoS}_2$  in a resin, there exists an optimum range of film thickness ( $0.01\text{-}100\text{ }\mu\text{m}$ ) that exhibits low friction and wear. Beyond a thickness of about  $10\text{ }\mu\text{m}$ , it has been found that the load is carried by the film instead of the substrate and the contact behaves as if there is no substrate. This increases the real contact area, resulting in more friction, while the increase in wear is caused by formation of large wear particles.

In this section we discussed different constituents of a sliding tribo-contact including surfaces, bulk materials and lubricants and their properties which play a significant role in the tribological behavior of such a contact. In order to further push the boundaries of mechanical efficiency, a multi-pronged approach to improving friction and wear behavior of sliding interfaces by devising novel engineering techniques and understanding wear mechanisms at the fundamental level is necessary and this dissertation aims to achieve this.

### **1.3 Dissertation outline**

This work aims to better understand the friction and wear mechanisms at play in a lubricated tribo-contact and effect further advancements in its friction and wear performance. Our approach is targeted towards optimizing various constituents of a tribo-contact i.e., surfaces, bulk materials and lubricants using novel strategies for each constituent respectively. Subsequent chapters will begin by briefly discussing some state-of-the-art optimization strategies for each constituent and identify areas of improvement. This will form the motivation for different studies in this dissertation, wherein we will discuss in detail, our novel approach, methodology and results of experiments performed as part of these strategies.

Surface treatments are often applied to materials to enhance their tribological properties including hardness, wear resistance and reduce friction. Gas nitriding is one such treatment which has been found to result in undesirable effects including phase transformation and surface deterioration in Ti6Al4V alloy. Additionally, Ti6Al4V alloy is known to be less conducive to forming processes at ambient or low temperatures leading to higher processing costs. These issues are addressed by a new surface treatment technique called

Ultrasonic Nanocrystal Surface Modification (UNSM) is a new surface treatment technique which involves imparting compressive residual stresses on the surface using a severe plastic deformation process. In Chapter 2, we perform tribological experiments including scratch and wear resistance testing to study how UNSM surface treatment may be able to address the undesirable effects of gas nitriding and also improve formability in Ti6Al4V alloy.

Bearing materials are predominantly hardened steels and ceramics, however, these materials have both advantages and disadvantages for a given application. Novel materials which are not only on par with current materials but are also able to address their shortcomings need to be explored and investigated for developing more efficient mechanical systems. In Chapter 3, we discuss the tribological characteristics of a relatively new material, 60NiTi (also known as Nitinol) in the presence of aerospace grease lubricants, evaluated using linear reciprocating sliding friction tests, interferometry, optical and scanning electron microscopy. These studies are helpful to understand how this material will behave in gears and bearings lubricated by greases not specifically designed for 60NiTi.

Developing next generation liquid lubricants requires further improvements in additives. Additives are chemicals added to liquid lubricants to improve certain aspects of lubrication. One area of improvement is developing multifunctional additives that can do the job of both viscosity and friction modifiers with similar or better performance compared to current formulations, thereby increasing benefits for the same cost. In Chapter 4, we study the friction and wear performance of low molecular weight polyalkylmethacrylates developed by Pacific Northwest National Lab (PNNL), which are designed to perform as multifunctional additives including viscosity index improvers, friction modifiers and anti-wear additives.

Further, with increasing duration of space missions, it has become necessary to study and develop dry film lubricants (DFLs) that are more reliable, predictable, and can last longer in space. But pre-launch testing of spacecraft components often deteriorates the life of dry film lubricants which needs to be estimated, so it can be known beforehand if it can last for the mission, thus avoiding costly failures. In Chapter 5, we discuss the tribological performance evaluation of a multifunctional additive, designed to mitigate both viscosity loss due to increased temperature and friction and wear, using unidirectional sliding friction tests and interferometry. We also discuss and compare the wear life of undoped and Ni-doped MoS<sub>2</sub> DFL (a popular spacecraft lubricant) evaluated using unidirectional sliding friction tests. We investigate the wear

mechanisms responsible for improved wear life in Ni-doped MoS<sub>2</sub> using interferometry, scanning electron microscopy and energy dispersive spectrometry.

Finally, building upon the results in Chapter 5, we propose future experimental work in Chapter 6 that aims to develop a cumulative damage model for sputtered MoS<sub>2</sub> DFLs, which will enable more accurate prediction of coating life that can be expected in vacuum of space after components coated with these DFLs are tested on earth ambient conditions resulting in partial consumption of the coating life.

## Chapter 2. Surfaces

### 2.1 Ultrasonic Nanocrystal Surface Modification

Microstructural characteristics of polycrystalline materials, particularly grain-size greatly influences their mechanical properties. Grain sizes of 10  $\mu\text{m}$  or more are considered as coarse grains, 1-10  $\mu\text{m}$  as fine grains and  $<1$   $\mu\text{m}$  as ultrafine grains. According to the well-known Hall-Petch relationship, strength of a metal increases with decreasing grain size due to increase in number of grain boundaries, which hinder the movement of dislocations [44]. Conventional metal forming processes are not able to easily generate ultrafine grains in manufactured components due to limited capability in imparted compressive stresses [45–49], calling for alternative processes. Severe plastic deformation (SPD) is a class of techniques that can produce ultrafine grains by imparting high levels of compressive stresses without altering the material geometry or chemical composition. Different SPD methods have been developed separately for bulk metals, sheet metals and tubular components [12]; some of the well-known ones include, equal channel angular pressing, high pressure torsion, shot peening, surface mechanical attrition treatment, and ultrasonic nanocrystal surface modification (UNSM) techniques.

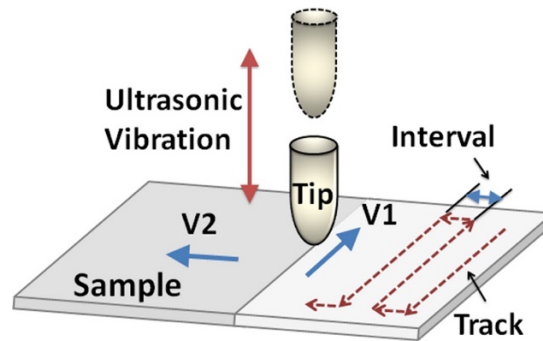


**Figure 2. 1.** Schematic showing the UNSM process where a pin with hemispherical tip strikes the sample at ultrasonic frequency and scans the entire area.

UNSM is a relatively new method in the category of SPD techniques which has been shown to improve surface micro-hardness and wear resistance of different materials including steel [50–52], titanium and its alloys [53–57], magnesium alloys [58, 59] and bulk metallic glasses [60]. This method consists of striking a surface with a ball or hemispherical pin at ultrasonic frequency as shown in Figure 2.1, imparting severe plastic deformation to the surface, resulting in a micro-layer of refined grains under compressive residual stresses with enhanced mechanical properties including strength and hardness.

Titanium and its alloys have attributes like high strength, high-temperature performance, corrosion resistance and biocompatibility, which makes them popular engineering materials for applications including aerospace, automotive and bioengineering. Despite such desirable properties, they suffer from drawbacks like high friction and wear and poor hardness which must be addressed for wider applicability. Surface treatment methods like boronizing, oxidation and nitriding, have been used to improve the surface properties of Ti-based materials enabled by the formation of surface compound layers of borides, oxides and nitrides which exhibit high hardness, corrosion, and wear resistance [61–63]. Gas nitriding is one such technique, although widely used, has been found to result in undesirable effects including phase transformation, surface deterioration, grain growth and precipitation [64–67] when performed at high temperatures, and calls for further process optimization.

In this work, the effectiveness of UNSM as a pretreatment process for gas-nitriding to improve scratch resistance was investigated. Gas-nitrided (at two temperatures 700 °C and 800 °C) specimens with and without UNSM treatment were provided by University of Akron. The specimens were substrates of  $\alpha/\beta$  titanium alloy Ti6Al4V with composition of 0.08 wt% carbon, 5.5-6.75 wt% titanium and 0-0.3 wt% other components and UNSM was performed as per procedure described in [68]. The scratch hardness tests were performed following ASTM standard G171-03 [69] using a Rtec Multifunction Tribometer. A constant normal load of 1 N was applied on a diamond sphero-conical tip indenter of radius 200  $\mu\text{m}$  while moving the sample 5mm laterally at a constant speed of 0.2 mm/s.

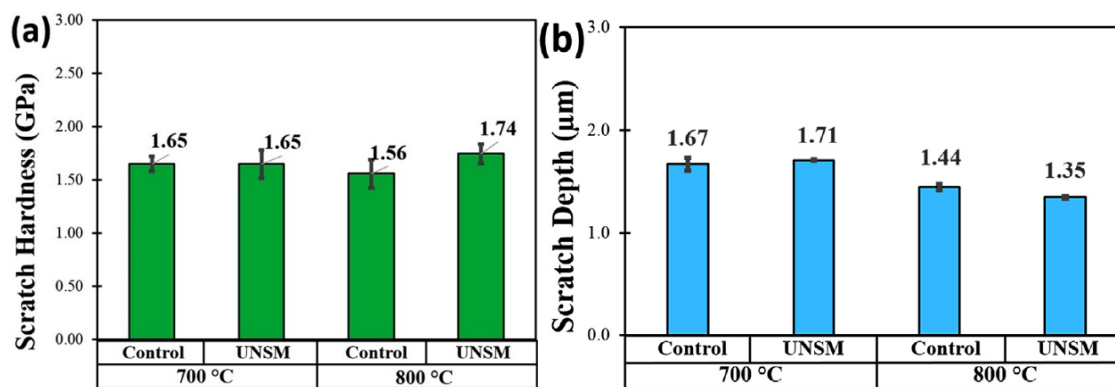


**Figure 2. 2.** Measured (a) scratch hardness and (b) scratch depth, after scratch tests at 1 N normal load.

The width of the scratch was then measured using white light interferometer images and the scratch hardness was calculated as  $HS_p = kP/w^2$ , where  $P$  is the applied normal force (gf),  $w$  is the scratch width ( $\mu\text{m}$ ),  $HS_p$  is the scratch

hardness number (GPa), and  $k$  is a geometric constant that takes the value 24.98 for the unit system used here. The scratch hardness number of each sample was determined as an arithmetic mean of a total of nine determinations (that is, 3 scratches and 3 width measurement locations per scratch). The scratch hardness test results are plotted in Figure 2.2.

The nitriding depth in 700 °C and 800 °C specimens of the control (without UNSM) and UNSM conditions are 0.1  $\mu\text{m}$ , 0.2  $\mu\text{m}$ , 1.2  $\mu\text{m}$  and 1.9  $\mu\text{m}$  respectively. The results reveal that the scratch hardness of Ti6Al4V after nitriding at 800 °C with UNSM pretreatment is higher than that of the sample without pretreatment (Figure 2.2(a)), which possibly originates from the thicker nitride layer assisted by the nano-grains. In all the other cases, the scratch depth (Figure 2.2(b)) was higher than the nitriding layer thickness possibly resulting in similar performances.

## 2.2 Electropulsing Assisted Ultrasonic Nanocrystal Surface Modification

Alloys of titanium are also known to be less conducive to forming processes at ambient or low temperatures which leads high processing costs [70]. To address this during UNSM, high static load and a large amplitude are necessary. However, this results in high surface roughness resulting in poor wear and corrosion resistance. Thermal assisted SPD could address this problem; however, it lowers the metal's yield strength and reduces its resistance to wear in addition to formation of oxide layers, induced thermal stresses and also causing microstructural changes.

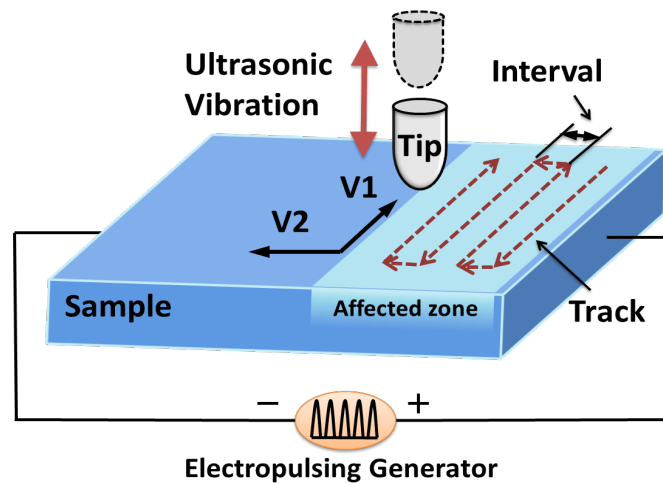


**Figure 2. 3.** Schematic showing electropulsing-assisted UNSM process.

Electrically-assisted-manufacturing (EAM) is another approach to improve metal formability, wherein a strong electric field is applied during deformation



of metals as described in Figure 2.3. Applying high density electrical pulses have been found to introduce both thermal and electronic effects on the deformation of solid metals [71]. This electropulsing induced high energy input method is an emerging technique in engineering treatments [72]. Electropulsing has been shown to improve ductility of metals [70, 73] and also enable faster movement of dislocations [74, 75]. In another study, the microhardness at high strain rate was found to significantly improve in Ti6Al4V when assisted by electropulsing during ultrasonic shocks [76]. These studies indicate that electropulsing can be a promising method to improve metal formability.

In this study, we evaluate and compare the wear performance of electropulsing-assisted UNSM specimen of NiTi alloy with a UNSM specimen fabricated without electropulsing and a control sample without any surface treatment. Tests were performed following an adaptation of the ASTM G133-05 standard for linear reciprocating ball-on-flat sliding wear tests, with modifications necessitated by limitations of the available test instrumentation. The ASTM standard recommends lubricated wear testing with a ball of diameter 9.53 mm at 150 °C, 10 mm stroke length, 10 Hz oscillating frequency, 400 m total sliding distance and a constant normal load of 200 N. However, our tests were performed with a 9.53 mm diameter ball at room temperature, 6 mm stroke length, 0.4 Hz oscillating frequency, a 100 sliding distance and a 25 N constant normal load. For each specimen, three tests were run in ambient air conditions.

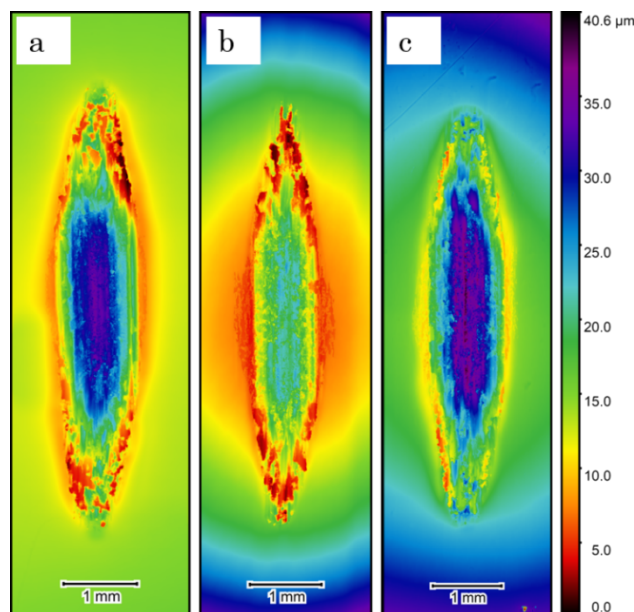


**Figure 2. 4.** Wear scars from each specimen type (a) Control (b) UNSM (c) EP-UNSM.

The representative wear scars from each specimen type are shown in Figure 2.4. To measure wear volume, the white light interferometer was used to capture high quality 3D images of wear scars on the specimen after the tests. Prior to imaging, the surfaces were thoroughly cleaned with acetone. The wear volume was calculated as an average of the cross-sectional area of six profiles along the wear scar multiplied by the length of the scar. The length of the scar only includes the constant width portion. The cross-sectional area of wear scar was defined as the difference between the areas above and below the average height of the surface [77].

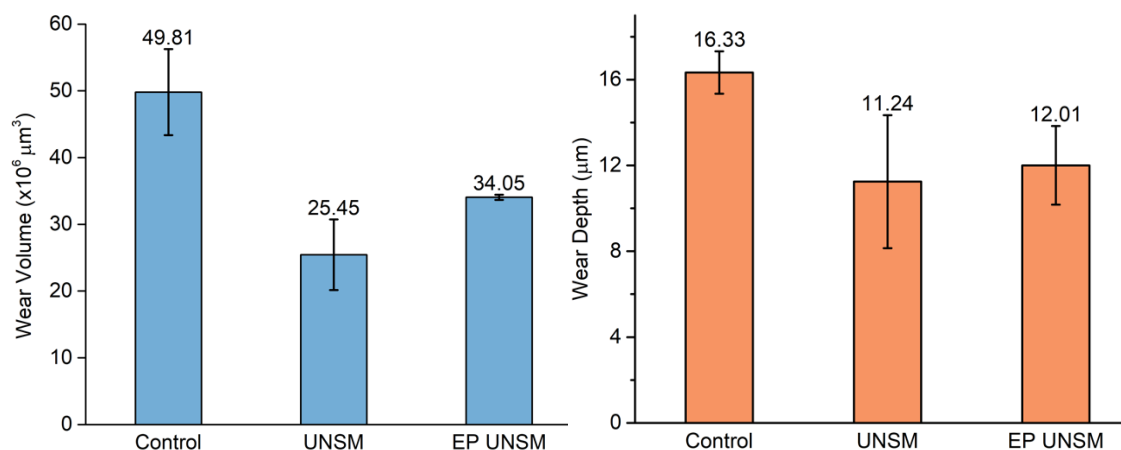


**Figure 2. 5.** (a) Wear volume comparison (b) Wear depth comparison.

The wear performance results are presented in Figure 2.5(a) and the depth of wear in all specimen types are compared in Figure 2.5(b). The values shown are average of 3 tests per specimen, with the standard deviation represented by the error bar. It is clear from the wear volume comparison that both UNSM and EP-UNSM resulted in higher wear resistance (lower wear volume) of the NiTi alloy surface. The wear depth results in Figure 2.5(b) also corroborated this result. Note that the wear depth of both UNSM and EP-UNSM specimens is within their respective surface treatment depths of 30  $\mu\text{m}$ . Although, contrary to expectations, EP-UNSM treatment did not result in better wear resistance compared to UNSM process. This could be explained by the formation of fine local recrystallized grains, corroborated in the optical microscopy images of cross-section of NiTi compared from different specimens by University of Akron, shown in Figure 2.6. These local recrystallized fine grains are known to increase ductility with the help of the high-density electrical pulses. This increase in ductility, which is considered to be less favorable to wear resistance [70], is the likely source of increased wear volume in EP-UNSM specimens.

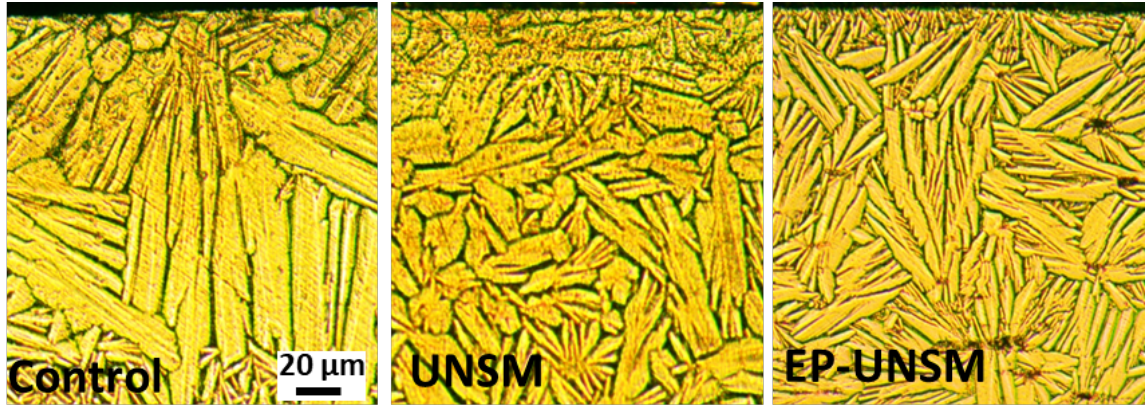


**Figure 2. 6.** Optical microscopy images of NiTi cross-sections from different specimen types. Image courtesy: University of Akron.

This study shows that electropulsing-assisted UNSM is a viable method to enhance formability of NiTi alloy with similar wear performance compared to UNSM treatment which itself improves the wear resistance of untreated NiTi alloy.

Overall, these studies show that UNSM can be an effective surface engineering technique to improve the tribological properties of Ti alloys which are otherwise known to exhibit poor wear resistance, limiting their applicability.

## Chapter 3. New Materials

### 3.1 Introduction

The material properties of bodies in a tribo-contact are as essential as the lubricant and surface properties in the tribological performance of a system. As discussed in Chapter 1 and 2, material properties including hardness, elastic modulus, strength, toughness, and micro-structural properties including grain size, phase composition and chemical compatibility with lubricant molecules greatly influence the friction and wear behavior of a tribo-system. It has been well documented that in most metals in general and ferritic metals in particular, hardness and wear resistance are closely related, where harder materials resist abrasive wear better [78, 79]. It has also been shown that a combined effect of hardness and compressive strength is a better indicator of wear resistance of a material, where two similarly hard materials WC and TiC had very different wear behavior [80]. Grain size has been shown to play a crucial role in improving tribological properties, where, with grain sizes in the 15 to 100 nm range in nanocrystalline aluminum, the hardness-grain size data could be well represented by Hall-Petch relationship, consequently reducing friction and wear with smaller sizes [81].

New material compositions and multiphase alloys are being developed which can exhibit enhanced mechanical as well as tribological properties. For example, recently developed Al-Si eutectic alloy is being widely adopted in military, automobile, and general engineering industries [82, 83], where addition of hard Si particles to the soft Al matrix has been found to improve its wear resistance by dispersion hardening [84]. Nanocomposite tribological coatings have been designed and studied to combine toughness improvement by nanocrystalline structures, have functionally gradient interfaces and incorporate nanoscale lubricant reservoirs to be able to respond to changing environmental conditions [85]. Material requirements for components exposed to extreme conditions, including shock loads during rocket launch, and drastic temperature cycling from cryogenic to excess of many hundreds of degrees centigrade, cannot be met by single phase materials and novel multiphase materials are currently being explored to perform in these conditions.

### 3.2 60NiTi (Nitinol)

Bearing materials are predominantly hardened steel, austenitic stainless steel, and ceramics, as well as sometimes non-ferrous alloys and plastics. These materials have both advantages and disadvantages for a given application. For example, hardened steels are cheap but suffer from weak corrosion resistance;

austenitic steels are corrosion resistant but not very hard; ceramics are very light and hard but extremely brittle; and non-ferrous alloys are cheap to produce but cannot withstand high pressures and temperatures. However, some bearing applications require materials with different combinations of these properties. One material being considered for this purpose is 60NiTi, a Nickel-Titanium alloy that consists of 60 wt. % Ni and 40 wt. % Ti. 60NiTi is non-magnetic and has high hardness (can be hardened to 62 HRC) with elasticity twice that of steel, excellent corrosion resistance, tensile strength comparable to ceramics, and is 15% lighter than steel [86]. This combination of properties makes 60NiTi a potential alternative bearing material [87, 88]. One application where 60NiTi is being considered for bearings is moving components in space vehicles, where the materials have to exhibit high hardness, moderate elastic modulus, and large recoverable strain to enable components to resist impact loads that occur during launch [87].

Most potential applications for 60NiTi include tribo-contacts lubricated by oil or grease. Thus, there is a need to understand the lubrication performance of 60NiTi in rolling and sliding contacts, which are the primary contact modes in bearings and gear applications. Some studies have been performed using unformulated oils, to minimize the number of variables and to enable isolation of lubrication mechanisms. Unformulated lubricant friction and wear tests have been performed using castor oil, seed oil, turbine oil and paraffin oil [89] where castor oil was found to exhibit lower friction and wear compared to the other oils. Similar studies showed that, at low contact pressures, a 60NiTi pin and 52100 steel sliding contact lubricated by castor oil can exhibit ultra-low friction (friction coefficient of 0.008) [89–91]. This result was later found to be strongly dependent on surface roughness, with the lowest friction only achievable with an average surface roughness of less than 20 nm [92]. Experiments using a 60NiTi pin sliding on 52100 steel were carried out with poly-alpha-olefin (PAO) oil and showed that the lubricant decreased the friction coefficient from 0.6 to 0.1 (relative to dry sliding) and improved wear resistance [93]. Tests with a linear reciprocating tungsten carbide ball on a 60NiTi plate using castor oil lubrication identified plastic deformation-induced abrasion as the primary wear mode [94]. In another study, it was found that friction and wear resistance of 60NiTi is worse than that of 440C stainless steel under castor oil lubrication with a sliding tungsten carbide ball [95]; in a follow-up study, the authors suggested this was due to 60NiTi exhibiting microscopic brittleness at the contact which allowed propagation of tensile microcracks leading to more wear [96].

Studies with fully formulated oils have also been performed. A spiral orbit tribometer was used to characterize multiply-alkylated cyclopentane (MAC) oil [87, 88, 97–99] and perfluorinated polyether (PFPE) oils [98, 99]. The MAC oil (commercial name Pennzane 2001A) and PFPE oils (Krytox 143 AC and Castrol Brayco 815Z) are commonly used in space applications. These studies showed that fully-formulated oils can successfully lubricate 60NiTi on 440C [98] and self-mated 60NiTi rolling-sliding contacts [99]. It was also found that 60NiTi is amenable to conventional oil lubrication with a low constant coefficient of friction (CoF) and that this contact exhibits lubricant degradation rates similar to iron-based materials (440C and 52100 steels) [99]. Further, linear reciprocating wear testing was used to study synthetic gear oil in sliding contacts [94, 95]. These studies showed that a tungsten carbide ball sliding on a 60NiTi flat exhibited higher wear and friction than on a 440C flat, although the reasons for this difference are still not fully understood [95].

To date there have been few studies of 60NiTi sliding against a similarly hard material (either a hardened steel or self-mated) with fully formulated oils or greases. Also, to the best of our knowledge, there have been no grease lubricated sliding contact studies using self-mated 60NiTi. Such studies are necessary to understand how this material will behave in gears and bearings lubricated by greases containing additives not specifically designed for 60NiTi. In this paper, we characterize the friction and wear of self-mated 60NiTi contact in pure sliding, boundary lubrication, conditions chosen to capture material wear behavior under extreme conditions, i.e., when the contact is lubricant-starved and ceases rolling. Tests are performed with greases consisting of different base oil types and thickener types to enable direct comparison between the greases. Results are then analyzed to explore the friction and wear mechanisms exhibited by grease-lubricated, self-mated 60NiTi in sliding contacts.

Five different greases were used in this study, as summarized in Table 1. Three of these (Braycote 601EF, Braycote 602EF and Nye Rheolube 2000) are currently being used in space/vacuum applications where low outgassing and low volatility are necessary. Nye Rheolube 374A is used in the aviation industry and SKF LGMT2 is a general-purpose grease used in automotive bearings, conveyor belts, small electric motors, etc. This combination of greases was selected to provide performance data for self-mated 60NiTi tribo-contacts in space/vacuum applications as well as for terrestrial applications. It should be noted that the base fluids of some greases tested here are the same as those of formulated oils characterized in previous studies of self-mated rolling-sliding contact, i.e., the base oil in Braycote 601EF and Braycote 602EF is

Castrol Brayco 815Z and the base oil in Nye Rheolube 2000 is Pennzane 2001A [87, 88, 97–99].

**Table 1.** Summary of greases used in this study.

<b>Grease</b>	<b>Base Fluid</b>	<b>Thickener Type</b>
SKF LGMT2	Mineral Oil	Lithium Soap
Braycote 601EF	Perfluorinated polyether, PFPE (Castrol Brayco 815Z)	Polytetrafluoroethylene Particles
Braycote 602EF (Contains MoS <sub>2</sub> )	Perfluorinated polyether, PFPE (Castrol Brayco 815Z)	Polytetrafluoroethylene Particles
Nye Rheolube 374A	Polyalphaolefin, PAO	Lithium Soap
Nye Rheolube 2000	Multiply-alkylated cyclopentane, MAC (Pennzane 2001A)	Sodium Soap

Ball and flat samples used in this study were 60NiTi-Hf, an alloy containing one atomic percent Hafnium, and were donated by the NASA Glenn Research Center (subsequently referred to simply as 60NiTi). The flat samples were polished in two steps using an Allied High Tech Metprep 3 polisher, first with silicon carbide abrasive pads and second with a polycrystalline diamond abrasive in a hexylene glycol suspension for final surface finish. The average roughness of the ball and flat were 46 nm and 6 nm, respectively, as measured using a white light interferometer. Prior to each test, the surfaces of the ball and flat were thoroughly cleaned with acetone and, if fluorinated oil was present, with Vertrel XF. The flat was also ultrasonically cleaned in heptane for 5 min. Approximately 0.5 g of grease was evenly spread along the ball path on the flat prior to testing.

The tribological performance of the greases was measured using an Rtec Instruments Multi-Function Tribometer. Tests were performed following an adaptation of the ASTM G133-05 standard for linear reciprocating ball-on-flat sliding wear tests, with modifications necessitated by limitations of the available test instrumentation. The ASTM standard recommends lubricated wear testing with a ball of diameter 9.53 mm at 150 °C, 10 mm stroke length, 10 Hz oscillating frequency, 400 m total sliding distance and a constant normal load of 200 N which corresponds to 1.6 GPa maximum Hertz contact pressure for a self-mated 60NiTi contact. However, our tests were performed with a 4.76 mm diameter ball at room temperature, 10 mm stroke length, 0.25 Hz oscillating frequency, two sliding distances (short 30 m and long 100 m) and a



11.49 N constant normal load corresponding to a maximum Hertz contact pressure of 1 GPa. For each grease, three tests were run with a 30 m sliding distance and one test with a 100 m sliding distance. All tests were performed in atmosphere with a measured relative humidity between 35–50%.

Images of the worn surfaces were obtained from a white light interferometer onboard the tribometer (with data processed using Gwyddion), a Leica (Model DM 2500M) optical microscope, and a Zeiss Gemini 500 scanning electron microscope (SEM). To measure wear volume, the white light interferometer was used to capture high quality 3D images of wear scars on the balls and flats after the 30 m sliding tests. Prior to imaging, the surfaces of the ball and flat were thoroughly cleaned with acetone and heptane, as well as Vertrel XF if fluorinated oil was present, as described in the previous section.

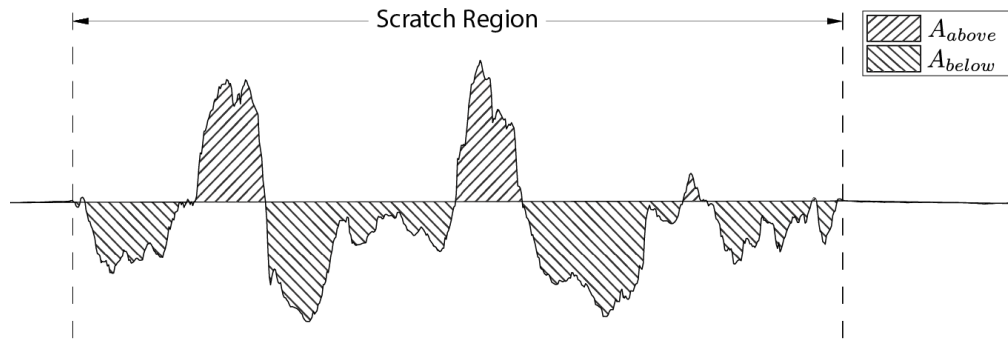


**Figure 3. 1.** Schematic diagram illustrating the wear calculation for a flat wear scar.

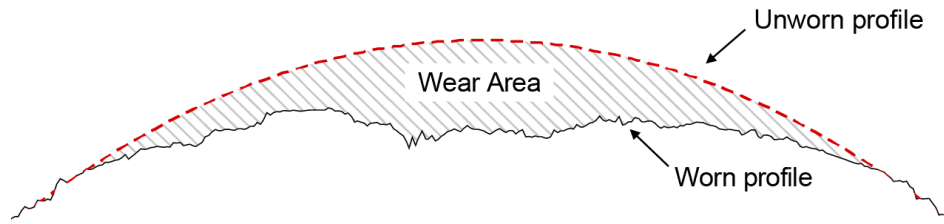


**Figure 3. 2.** Schematic diagram illustrating wear calculation for the ball samples.

The volume of the wear scars on the flats was calculated as an average of the cross-sectional area of six profiles along the wear scar multiplied by the length of the scar. The cross-sectional area of the wear scar was defined as the difference between the areas above and below the average height of the surface [77], as shown in Figure 3.1. It should be noted that protruding features will increase the area above the average surface height and decrease the wear volume. For small wear cases, the ball wear volume was calculated from the difference between the volume of an unworn ball and that of a worn ball over the entire scar area, as illustrated in Figure 3.2. In some cases, the wear on



the ball was too severe to calculate with this approach, so a spherical cap approximation was used to estimate wear volume geometrically [100]. Specific wear rates were calculated as the wear volume divided by total sliding distance (30 m) and normal load (11.49 N).

The friction and wear behavior are analyzed for self-mated 60NiTi sliding contact with each grease. First, the CoF is shown as a function of sliding distance

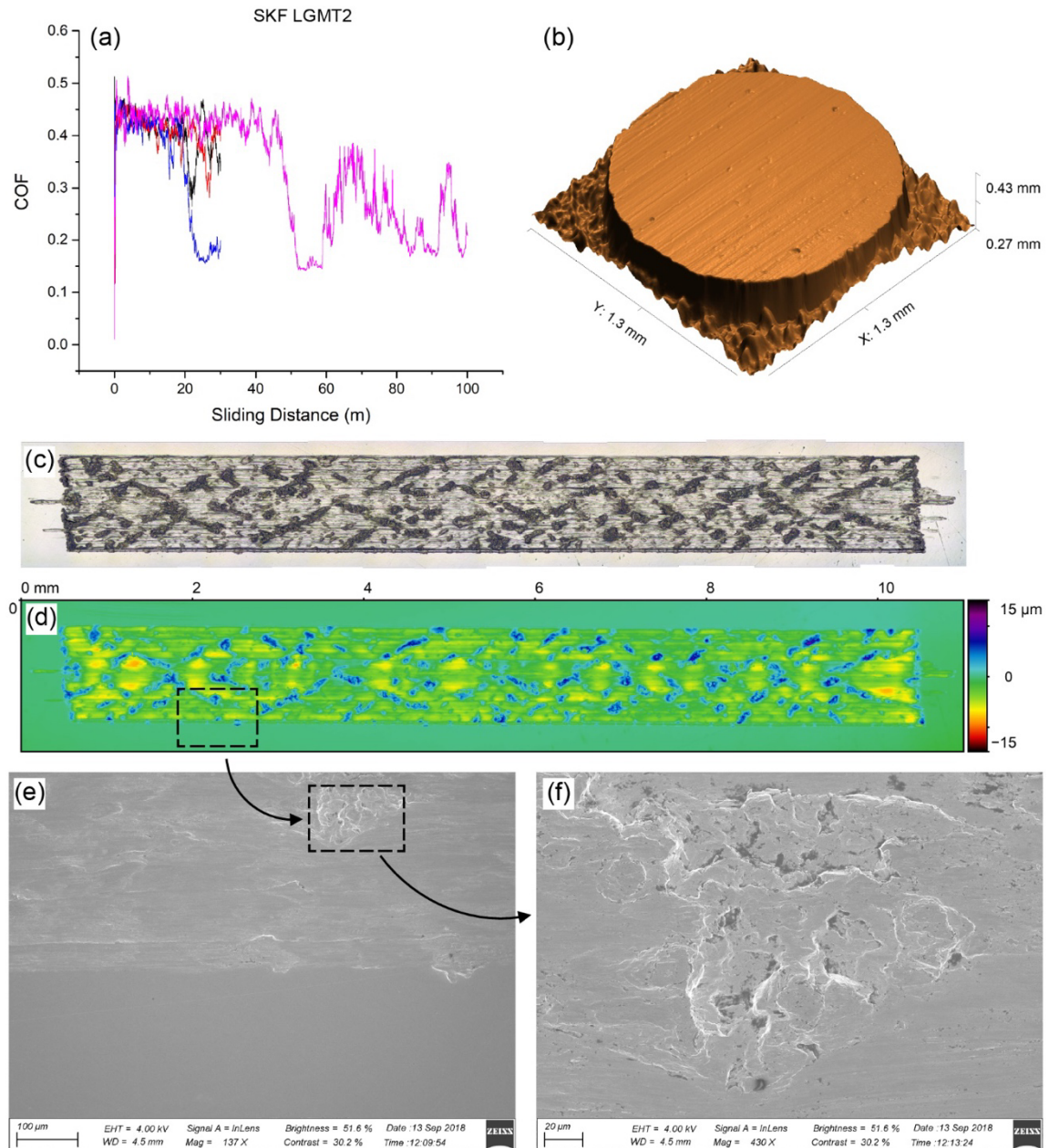


**Figure 3. 3.** Test results for SKF LGMT2 including (a) friction traces, (b) interferometer image of the ball wear scar, (c) and (d) optical microscope and interferometer images of the flat wear scar, and (e) and (f) SEM micrographs of flat wear scar. All wear images correspond to the test shown in blue in (a).

nce for four tests (three at 30 m and one at 100 m). The friction traces of the three 30 m tests are shown as red, black, and blue, and the 100 m tests are shown in magenta. Then, representative wear scars on the ball and the flat are shown from one of the 30 m sliding distance tests for each grease. Wear analyses include interferometer images of the ball wear scar, interferometer, and optical microscope images of flat wear scar, and in some cases, SEM images of the region within the wear scar on the flat.

Test results for the SKF LGMT2 are shown in Figure 3.3. The CoF in Fig. 3.3(a) is initially high ( $\sim 0.45$ ) for all four cases. In one of the 30 m cases, the friction decreases around 20 m of sliding. This decrease is also exhibited by the 100 m case, albeit around 40 m of sliding. Overall, the friction is never observed to be consistently low with this grease (CoF in the range of 0.15 to 0.4). Figure 3.3(b) shows the wear scar on the ball with severe scoring marks parallel to the sliding direction, indicating predominantly abrasive wear [101]. The corresponding scar on the flat shows faint abrasive wear marks and protruding features, as indicated by blue regions in the interferometer image (Fig. 3.3(d)) and dark regions in the optical microscope image (Fig. 3.3(c)).

The observed protruding features are likely adhered wear debris. Two regions are magnified in the SEM micrographs in Figures 3.3(e) and 3.3(f) which show that the size of the adhered features range from a few tens to hundreds of microns, indicating this behavior is prevalent across different scales of asperity contact. The large amount of material adhesion is possibly a result of galling [77], which would be consistent with the behavior of titanium and its some of its alloys [98, 102] in sliding. Despite the signs of adhesive wear on the flat, the scoring marks on the ball suggest abrasive wear. To explain this, we postulate that wear debris adheres to the flat, then it is work-hardened due to the severe test conditions and finally this hard material on the flat abrades the relatively softer ball.

Test results for Braycote 601EF are shown in Figure 3.4. The CoF traces in Figure 3.4(a) for this grease are consistent across the four tests. In all cases, there is a short run-in period followed by low friction (average CoF of 0.14 after 10 m of sliding) with intermittent friction peaks, possibly due to wear followed by removal of worn material from the wear track. The longer duration test (100 m sliding distance) shows that the height and frequency of these friction peaks decrease with sliding distance. Ball wear, shown in Figure 3.4(b), was very low, with a groove in the center of the scar and mild abrasive marks around it. Unlike the SKF LGMT2, there were no protruding features found on the flat wear scar shown in Figures 3.4(c) and 3.4(d), which suggests this contact is

dominated by abrasive wear [101] as evidenced by the longitudinal grooves shown in Fig. 3.4(d).

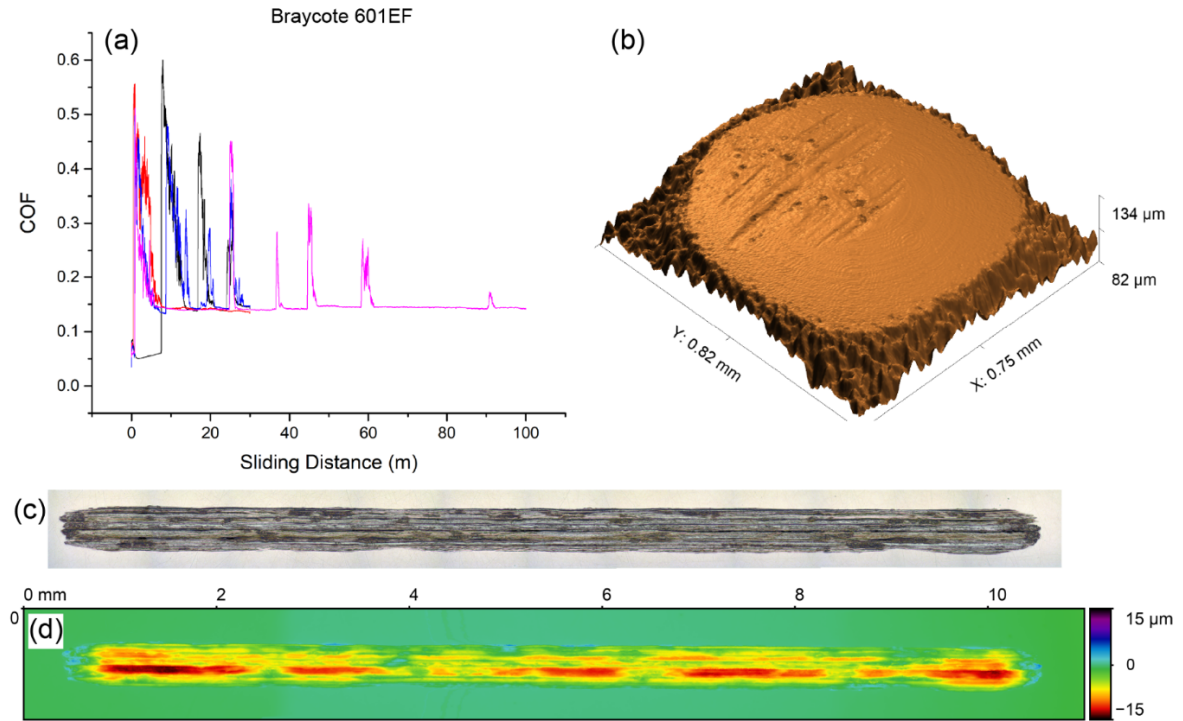


**Figure 3. 4.** Test results for Braycote 601EF including (a) friction traces, (b) interferometer image of the ball wear scar, and (c) and (d) optical microscope and interferometer images of the flat wear scar. All wear images correspond to the test shown in blue in (a).

One outcome of this is that, although the width of the wear scar on the flat is much smaller than that with the SKF LGMT2 shown in Fig. 3.3(d), the wear depth is greater (more red and dark red regions) for Braycote 601EF, because there is no adhered material.

Test results for Braycote 602EF are shown in Figure 3.5. The CoF traces for the 30 m tests are similar to those from the Braycote 601EF, but with fewer friction peaks. Also, the mean CoF after 10 m of sliding is slightly lower at 0.13, possibly due to the presence of MoS<sub>2</sub> additive in the grease. The wear on the ball (Figure 3.5(b)) and flat (Figure 3.5(c) and 3.5(d)) are also similar to those of Braycote 601EF, characterized by narrow, sometimes deep wear features, indicating abrasive wear. SEM micrographs of the flat wear scar for this grease contain many micron-sized dark spots, as shown in Figure 3.5(e) and 3.5(f).

Since the SEM was performed after ultrasonicing the sample in a heptane bath for 5 min and drying with forced air, it is unlikely these are residual spots of grease. Compositional analysis using energy-dispersive x-ray spectroscopy

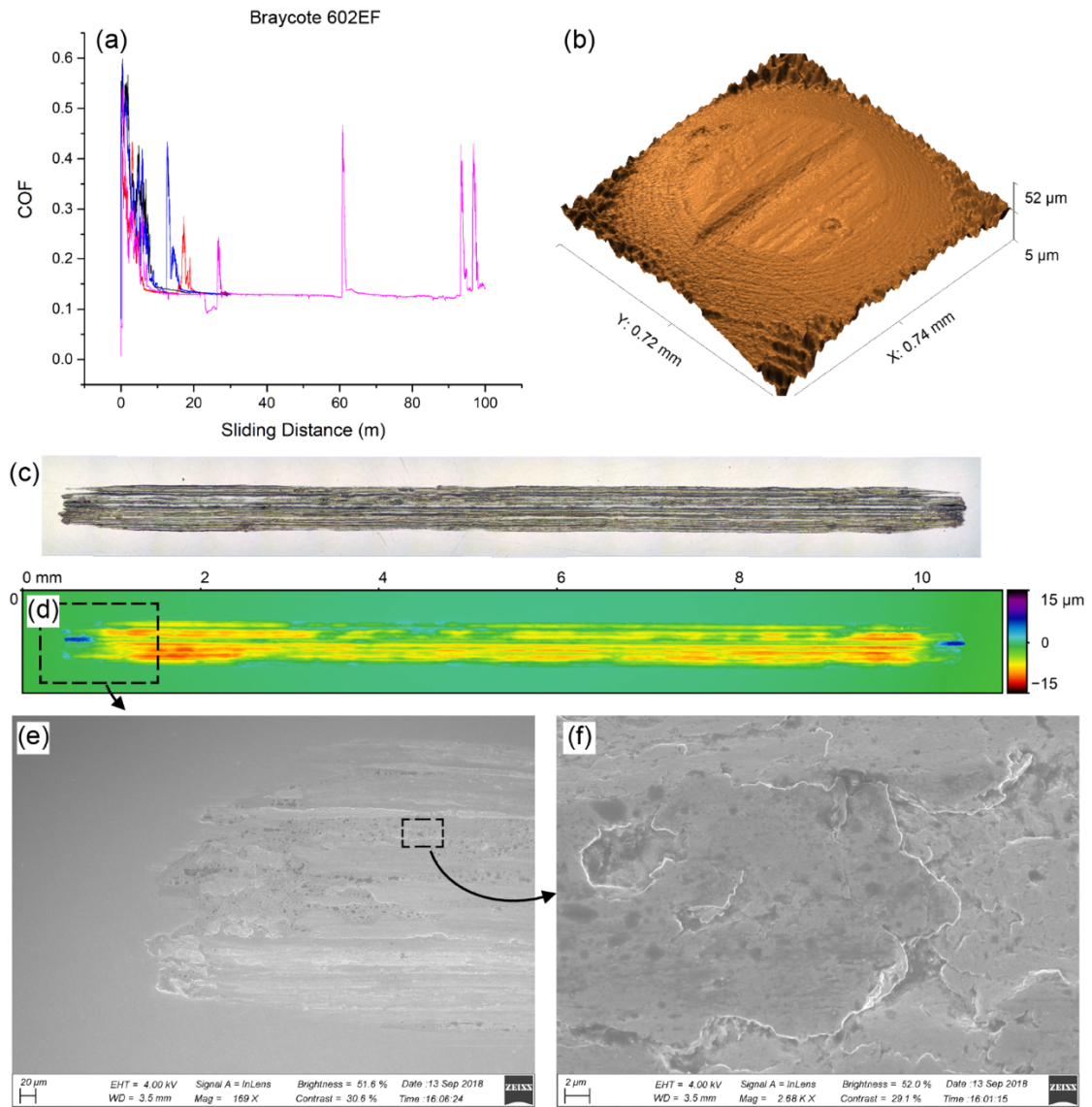


**Figure 3. 5.** Test results for Braycote 602EF including (a) friction traces, (b) interferometer image of the ball wear scar, (c) and (d) optical microscope and interferometer images of the flat wear scar, and (e) and (f) SEM micrographs of flat wear scar. All wear images correspond to test shown in blue in (a).

(EDAX) was performed on these scars to investigate the dark spots, but the results did not conclusively explain their origin. Similar spots were observed with the Braycote 601EF, but were significantly less in superficial density compared to Braycote 602EF,

Test results with Rheolube 374A are shown in Figure 3.6. The CoF traces in Figure 3.6 (a) exhibit a decrease in friction in the first 7 m of sliding, after which the friction is erratic and relatively high (average friction of 0.22 as calculated after 15 m of sliding). This behavior is similar to that of SKF



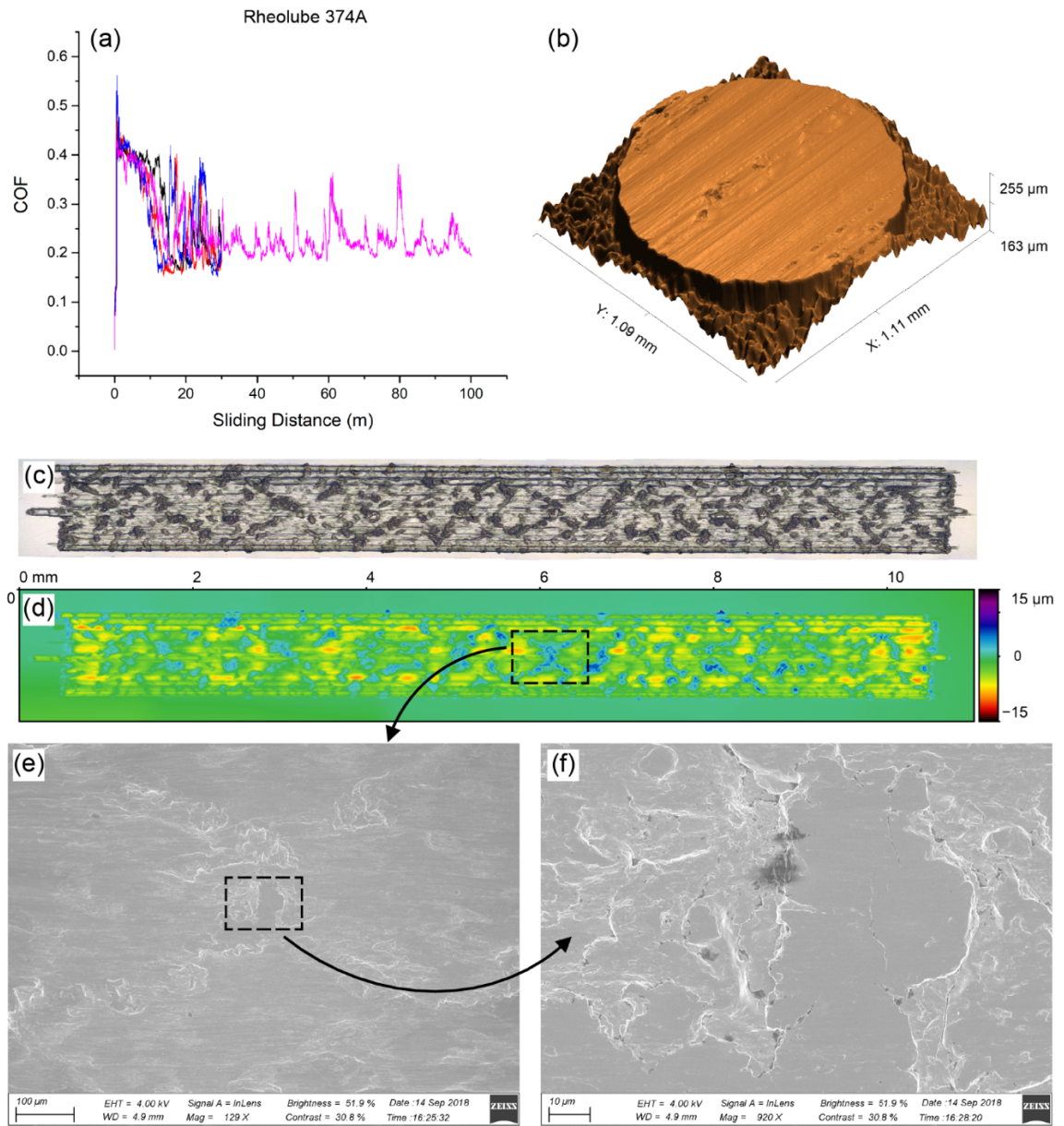


**Figure 3. 6.** Test results for Rheolube 374A including (a) friction traces, (b) interferometer image of the ball wear scar, (c) and (d) optical microscope and interferometer images of the flat wear scar, and (e) and (f) SEM micrographs of flat wear scar. All wear images correspond to the test shown in red in (a).

LGMT2, but the friction decreases with sliding distance more quickly with the Rheolube 374A. The longer duration test exhibits the same trends as those run for 30 m, with a rapid friction decrease leading to erratic friction with an average value of 0.22 after 15 m. The interferometer image of the ball wear

scar in Figure 3.6 (b) shows significant wear and abrasive wear marks, similar to the SKF LGMT2. Also, the wear scars shown in Figures 3.6(c) and 3.6(d) suggest a combination of adhesive and abrasive wear, as evidenced by protruding features that are higher than the original surface (blue in the interferometer image) and abrasive scoring marks (yellow streaks). Therefore, the mechanisms of wear may be similar for the SKF LGMT2 and Rheolube 374A. SEM micrographs of the protruding features from the wear scar are shown in Figures 3.6 (e) and 3.6 (f) and suggest that the material adhered to the flat has been sheared and flattened due to cyclic shear stresses.

Test results with the Rheolube 2000 are shown in Figure 3.7. This grease exhibits a high CoF (between 0.4 and 0.5) until 25 to 30 m of sliding, after which it drops to a constant value of 0.13, as shown in Figure 3.7 (a). The inter-

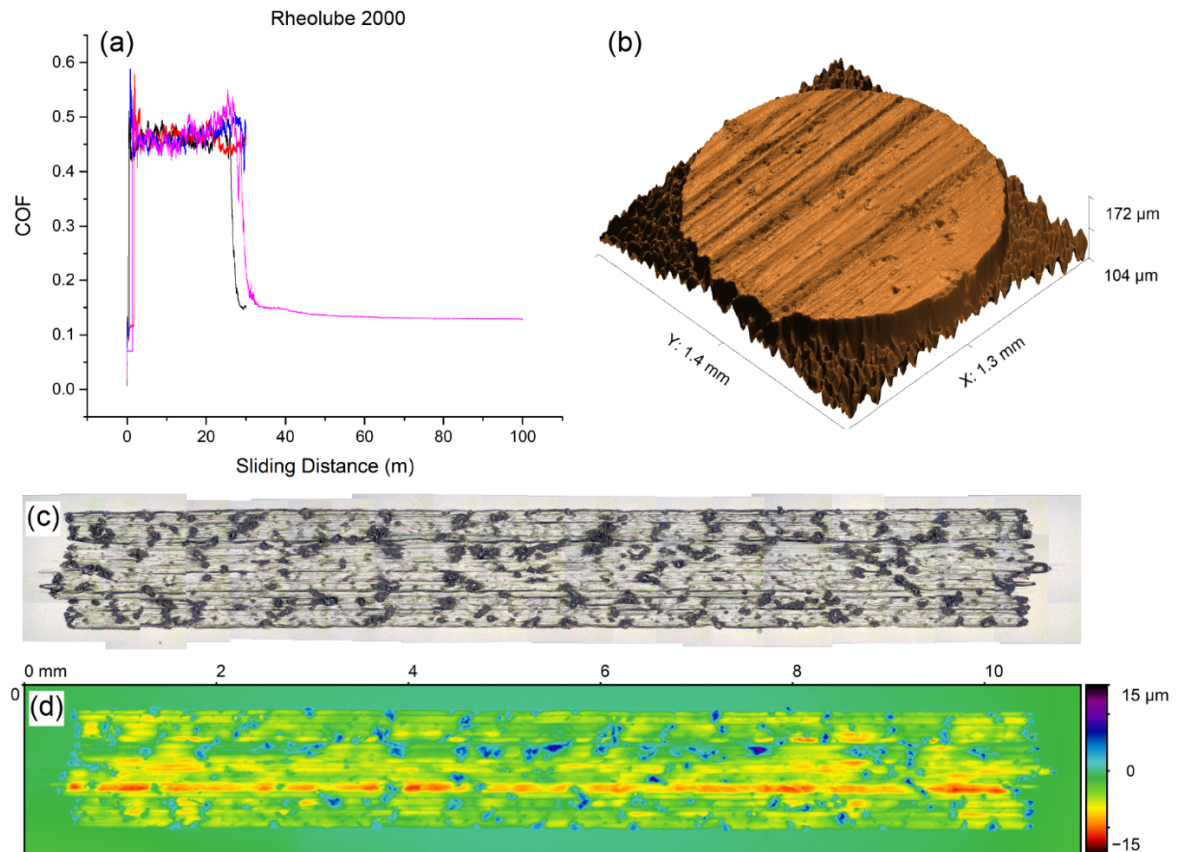


**Figure 3. 7.** Test results for Rheolube 2000 including (a) friction traces, (b) interferometer image of the ball wear scar, and (c) and (d) optical microscope and interferometer images of the flat wear scar. All wear images correspond to the test shown in black in (a).

Interferometer image of the ball wear scar in Figure 3.7 (b) shows severe abrasive wear, similar to that observed with Rheolube 374A and SKF LGMT2. The

Rheolube 2000 ball wear scar differs, however, in that it exhibits micro-sized pits along with the scoring marks. The flat wear scar width and appearance resemble the Rheolube 374A with protruding features and mild abrasive scoring marks. However, unlike the Rheolube 374A and SKF LGMT2, here the presence of adhered material inside flat wear scar and severe abrasion on ball did not result in high, erratic friction in the 100 m test.

To compare the wear behavior of each grease quantitatively, we calculated the wear volume of the ball and flat from the 3D interferometer images of the wear scars after all three 30 m tests. The results are shown in Figure 3.8. The wear volume comparison shows that flat wear (Figure 3.8 (a)) is nearly the same in all cases, except for Rheolube 2000 which has nearly twice the wear of the other greases. However, the similarity in the wear volume is misleading since the SKF LGMT2 and Rheolube 374A wear tracks are wide with significant adhered material, while the flat wear scars of the two Braycote greases are narrower and deeper. The difference in wear performance is more obvious in the comparison of ball wear, shown in Figure 3.8 (b). The two Braycote greases have an order of magnitude lower wear than the other greases. This is followed by the Rheolube 374A, and then the SKF LGMT2 and Rheolube 374A that have the most ball wear. For SKF LGMT2 and Rheolube 374A, the ball wear is greater than that of the flat, likely due to material that adheres to the flat during testing.

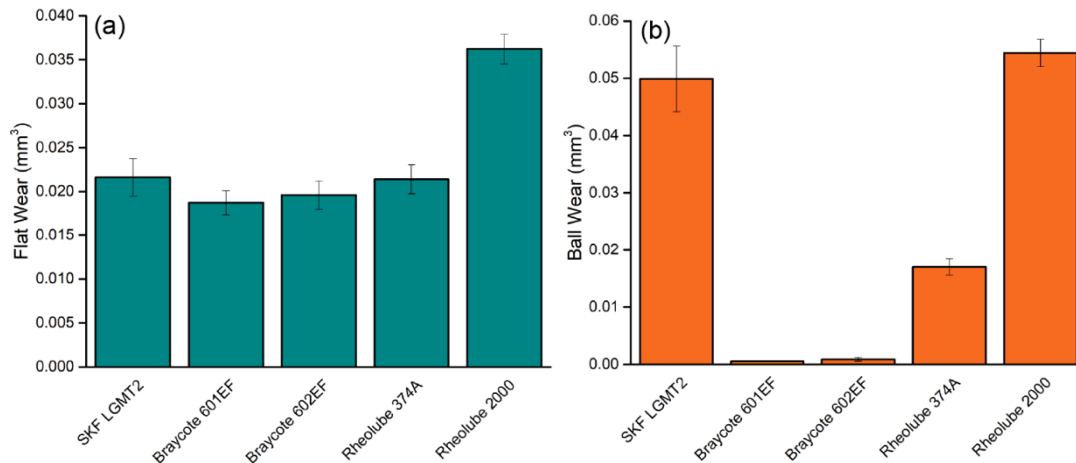


**Figure 3. 8.** Wear volume averaged over the three 30 m test for each grease as measured from the (a) flat and (b) ball. Error bars reflect the standard error of three tests.

The specific wear rates with each grease for the ball, the flat and for both surfaces from the 30 m tests are summarized in Table 2. The trends in specific wear rate for the ball and flat reflect the trends observed in Figure 3.8. Also, the flat wear rates in our tests are comparable to those reported in other

studies [94–96] with 60NiTi sliding against tungsten carbide ball with castor oil or fully-formulated PAO gear oil. The combined wear rates enable direct comparison of the greases and show that, in terms of wear, the greases tested here compare as follows: Nye Rheolube 2000 < SKF LGMT2 < Nye Rheolube 374A < Braycote 602EF  $\approx$  Braycote 601EF.

**Table 2.** Specific wear rates ( $\times 10^{-5}$  mm<sup>3</sup>/m · N) calculated from the 30 m tests.

<b>Grease</b>	<b>Flat</b>	<b>Ball</b>	<b>Combined</b>
SKF LGMT2	6.3 $\pm$ 1.1	14.4 $\pm$ 1.7	20.7 $\pm$ 2.0
Braycote 601EF	5.4 $\pm$ 0.7	0.2 $\pm$ 0.1	5.6 $\pm$ 0.7
Braycote 602EF	5.7 $\pm$ 1.2	0.3 $\pm$ 0.1	5.9 $\pm$ 1.2
Nye Rheolube 374A	6.2 $\pm$ 0.7	4.9 $\pm$ 0.4	11.1 $\pm$ 0.8
Nye Rheolube 2000	10.5 $\pm$ 0.9	15.8 $\pm$ 0.7	26.3 $\pm$ 1.1

The results from this study can be analyzed in the context of previous reports of 60NiTi tribo-performance. First, our Rheolube 2000 tests can be compared to spiral orbit tribometer measurements of self-mated 60NiTi using Pennzane 2001A oil lubrication [97], which is the base fluid in Rheolube 2000. Unlike the results shown in Figure 3.7, the previous study reported that 60NiTi is amenable to lubrication with Pennzane 2001A and rolling-sliding contact was measured with a low, steady CoF of approximately 0.06 and no material adhesion. The Hertz contact pressure was  $\sim$ 1 GPa in both studies, so the differenced are likely due to the severity of the test conditions, i.e., our tests are pure sliding which is much more severe than rolling-sliding contact. Another comparison can be made related to the adhered material features we observed in the flat wear tracks for SKF LGMT2, Rheolube 374A and Rheolube 2000. These features are similar to those found in the flat wear tracks after sliding a tungsten carbide ball on 60NiTi in unlubricated conditions at similar contact pressures [95]. The composition of the protruding features was measured using energy dispersive x-ray spectroscopy and showed that the material mainly consisted of Ni, Ti, O, and a negligibly small amount of ball material, which suggested that the protruding features did not form due to material transfer from ball to flat. In our study of self-mated 60NiTi, it is likely that the protruding features consist of material that was originally from both the ball and the flat. However, no such features were observed in the rolling-sliding spiral orbit tribometer tests for self-mated 60NiTi lubricated with Pennzane 2001A oil [97]. These observations suggest that the protruding



features observed in this study may have formed while the ball was sliding against the flat in starved lubrication conditions. It is known that grease lubricated contacts are susceptible to starved lubrication conditions when the grease is unable to supply the contact with a sufficient amount of oil [103–106], which would explain the similarity between our tests and the unlubricated tests from [95].

Overall, the PFPE-based vacuum greases (Braycote 601 and 602 EF) performed the best, with the lowest friction and wear. Of those two, the 602EF exhibited slightly lower average friction and wear, possibly due to the presence of the  $\text{MoS}_2$  additive, but the difference was not statistically significant. Comparing the other three greases, the mineral-oil-based general purpose grease (SKF LGMT2) and MAC-based vacuum grease (Rheolube 2000) performed the worst, exhibiting high friction throughout the test and significant wear. The PAO-based high temperature grease (Rheolube 374A) was moderate in both friction and wear. The results of this study are the first step towards a complete evaluation the friction and wear performance of self-mated 60NiTi contacts. Future investigations should include rolling-sliding contacts and other pressure conditions. A comprehensive set of data for 60NiTi will facilitate use of this material for more and a wider variety of potential bearing applications.

## Chapter 4. Liquid Lubricants

### 4.1 Introduction

Using a liquid lubricating medium to improve relative motion between two bodies in contact is one of the earliest known friction reducing strategies. Liquid lubricants reduce friction force by creating a physical separation between the contacting bodies and allow smoother relative motion due to their low shear strength. By separating the contacting bodies, they also reduce wear of the materials in contact improving the durability and reducing the occurrence of failure.

Liquid lubricants range from organic liquids, including mineral oils and vegetable oils, to inorganic solids of polytetrafluoroethylene (PTFE), graphene etc. Typically, liquid lubricants consist of more than 90% base oil and remaining 10%, a combination of different additives. Additives are used to either enhance an existing property of the base oil or introduce a new property essential for a given application. Different types of additives are in use currently including additives for viscosity (viscosity modifiers, pour point depressants), lubricity (anti-wear additives, friction modifiers, extreme pressure agents), controlling chemical breakdown (detergents, antioxidants, rust inhibitors, metal deactivators) and contamination control (dispersants, anti-foam agents, anti-misting agents) [107].

Other commonly used additives are viscosity index improvers (VIIs), which mitigate the decrease of viscosity with temperature, and friction modifiers (FMs), that reduce friction in boundary and mixed lubrication or provide a stable friction profile. Most VIIs are high molecular weight polymers, designed to reduce viscosity losses at high temperatures. But VIIs also suffer from permanent shear thinning, i.e., cleavage of long polymer chains due to shear thus reducing their effectiveness. Therefore, new VIIs are needed to achieve the benefits of viscosity index improvement, friction and wear reduction yet having low molecular weight for superior shear stability.

### 4.2 Multifunctional Polymer Additives

The effectiveness and efficiency of lubricant and hydraulic fluids is largely determined by additives, chemicals that are introduced into lubricant formulations to improve specific aspects of performance. Some of the most commonly used additives are viscosity index improvers (VIIs), which mitigate the decrease of viscosity with temperature, and friction modifiers (FMs), that reduce friction in boundary and mixed lubrication or provide a stable friction profile. Typical VIIs are relatively high molecular weight polymers that reduce

viscosity losses with increasing temperatures. There are several different types of FMs, including organic friction modifiers, functionalized polymers, soluble organo-molybdenum additives and, more recently, dispersed nanoparticles [108]. It has been demonstrated that polymeric molecules with the right amount of polarity can adsorb onto metal surfaces and promote surface-polymer protective layers [109, 110]. This mechanism is particularly beneficial in the mixed and boundary lubrication regimes, where the engine encounters large frictional losses. Functionalized polymer additives have gained popularity in recent years owing to their organic/ashless and more environmentally friendly nature, as opposed to phosphorus, zinc and sulfur small molecule analogs [111].

In the past, polymeric systems intended to be a dual additive were explored: a VII and FM [112]. Those polymers were designed to have a relatively high molecular weight as their primary function was as viscosity index improvers. However, another consideration for VIIs is shear thinning, a common phenomenon among high molecular weight polymers due to mechanical cleavage of chemical bonds during shear [113–116]. Furthermore, the architecture of the polymer has a significant influence on the stability of the polymer under shear stress, with the linear architecture being the least stable and dendritic or hyperbranched being the most stable [117, 118].

Previous studies have shown that functionalized polyalkylmethacrylates (PAMA)s also formed boundary films if the polymer had a block topology, rather than if it was randomly distributed; however, recent work demonstrated that enough polarity can overcome a topology bias [112, 119]. The topology of the polymer will influence the interaction with metal surfaces and therefore the conformation of the polymer near or on the surface. Block copolymers have been shown to induce mushroom and brush conformations, while random copolymers lead to a pancake conformation [14]. Indeed, functionalized PAMAs reduced friction significantly in the mixed and near boundary lubrication regimes [120].

This work focuses on investigating the friction and wear performance of a multifunctional additive designed by PNNL to achieve the combined benefits of viscosity index improvers, friction modifiers and anti-wear additives with excellent shear stability using low molecular weight polymers. Homopolymers of dodecyl methacrylate, 2-ethylhexyl methacrylate and co-polymers of functional methacrylates (polar) were synthesized via a free radical process, to generate a wide range of molecular weights with the lower molecular weight fraction being more efficient towards friction/wear reduction while the larger

molecular weight portion would be contributing towards a higher viscosity index. The polymers were added to the base oil at a fixed concentration of 12.5% w/w and then characterized in terms of their friction and wear. The performance of these polymer analogs was compared to that exhibited by two benchmarks: a commercial VII and a fully-formulated oil containing a previously developed VII polymer [111].

Polymers used in this study, designated AW-1 through AW-6 (shown in Table 3), were dissolved into 4Yubase at a concentration of 12.5% w/w. This fixed concentration was chosen to reach kinematic viscosities between 30 and 60 cSt at 40 °C, and VIs near 200. The performance of these multifunctional analogs was compared to benchmarks B-1 and B-2, where B-1 was a polyalkylmethacrylate diluted at 4.1% w/w concentration (donated by Evonik) and B-2 was a fully formulated blend, containing 1.5% w/w viscosity index improver. All analogs were blended at concentrations which yielded similar kinematic viscosities at 40 °C between 30 and 60 cSt.

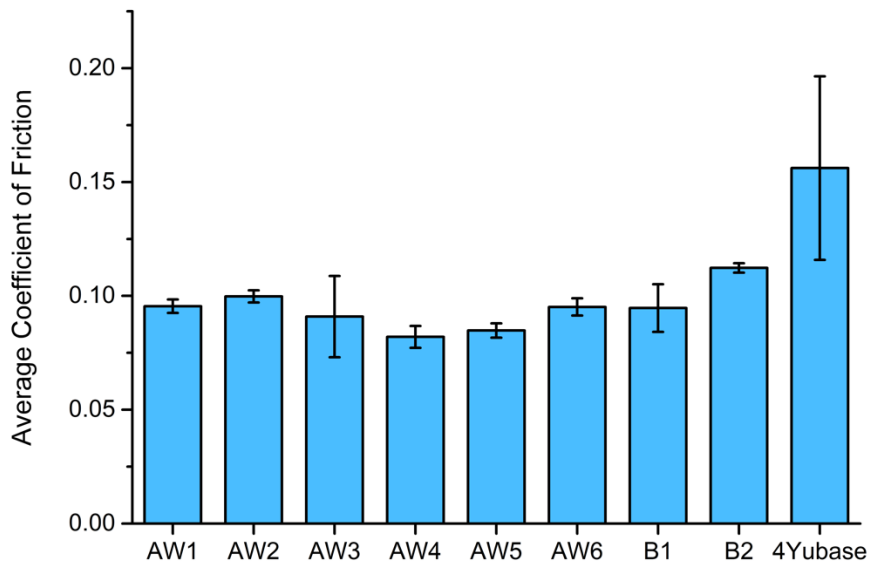
**Table 3.** Polymer analog and benchmark solutions studied in this research.

<b>Sample</b>	<b>Composition</b>	<b>Concentration in 4Yubase</b>
AW-1	PA12MA-DMAEMA	12.50%
AW-2	PA12MA-MEMA	12.50%
AW-3	PA12MA	12.50%
AW-4	PEHMA	12.50%
AW-5	PA12MA-EHMA-DMAEMA (low AIBN)	12.50%
AW-6	PA12MA-EHMA-DMAEMA (high AIBN)	12.50%
B-1	N/A	4.10%
B-2	N/A	1.50%

The friction and wear properties of the different lubricant samples were evaluated at 100 °C using a ball-on-disk setup on an Rtec Instrument Multi-Function Tribometer. Both ball and disk were of 52100 alloy steel material. The ball was 9.53mm in diameter and the ball and disk had an average surface roughness of 50 nm and 23 nm, respectively. Prior to each test, the surfaces of ball and disk were thoroughly cleaned with acetone. Approximately 0.5 mL of sample was evenly distributed onto the disk surface for testing. A constant normal load of 40 N, which correspond to a maximum Hertz contact pressure

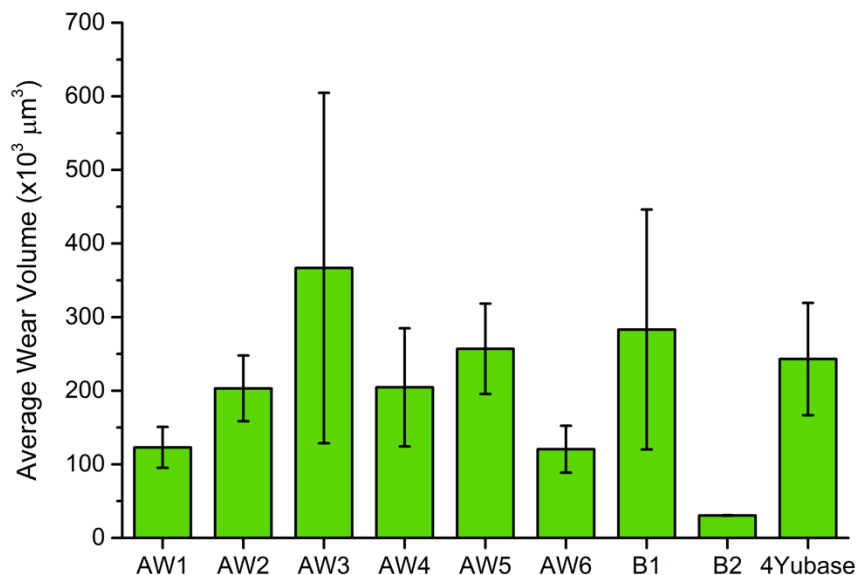
of 1.6 GPa, was applied on the ball. The disk was then rotated at a constant speed of  $80 \text{ mms}^{-1}$ , and the ball was slid for a total distance of 336 m. Each test was repeated at least three times. To verify that the tests were conducted under the boundary lubrication regime, a Stribeck curve was generated for one of the samples by varying speed and at a constant normal load of 40 N. The test conditions corresponded to the plateau region of the Stribeck curve, consistent with a boundary lubrication regime. In this regime, the CoF should be independent of viscosity. During the experiment, the instantaneous CoF of each compound was recorded throughout the experiment at a frequency of 10 data points per second. The average CoF was then calculated by averaging over all instantaneous CoFs, excluding data from the initial run-in distance, of 70 m. At the end of each run, the wear scar on the ball was cleaned with acetone and 0.05M EDTA solution to remove wear debris and tribo-film if any, prior to imaging [121]. High quality 3D images of the wear scar were then captured using a white light interferometer that was built-in to the tribometer. The white light interferometer recorded raw pixel height data, which provided detailed information on the topography of the ball and wear scar. By fitting the raw topography data to a spherical shape fitting tool, the expected initial geometry of the ball could be obtained. Wear was then calculated from the difference in height between the initial geometry of the ball and its projection on the ball with the wear scar, multiplied by the pixel area.

Figure 4.1 summarizes the average CoF at  $100^\circ\text{C}$  for each analog. Most the samples exhibit good repeatability from test to test (standard deviation less than 7% of the mean value), except AW-3 and the base oil, for which more



**Figure 4. 1.** Average COF for each sample where the error bars represent the standard deviation of the results from multiple tests.

variation is observed. The polymer analogs and benchmark fluids all exhibit average CoF values between 0.08 and 0.11, better than the pure base oil, and comparable to the range of CoFs observed with typical fully-formulated lubricants [108, 122]. Therefore, the results indicate that the polymers can reduce friction in boundary lubrication at least as well as traditional friction modifiers. At the end of each test, the surface of the ball was analyzed under a white light interferometer to capture a 3D image of the wear scar. The detailed topographic information was used to estimate a wear volume. Figure 4.2 shows the average wear volume for each sample. The average wear volume of the polymer compounds ranges from 121 to  $367 \times 10^3 \mu\text{m}^3$ , which is comparable to the average wear exhibited by benchmark B-1 ( $132 \times 10^3 \mu\text{m}^3$ ) but higher than that of B-2 ( $31 \times 10^3 \mu\text{m}^3$ ). This is expected since B-2 is a fully formulated oil additized with ZDDP anti-wear package, while the other solutions contain base oil and polymer only, without an anti-wear package.



**Figure 4. 2.** Average wear volume for each sample where the error bars represent the standard deviation.

Although the polymer analogs did not perform as well as the fully formulated benchmark B-2, as expected, their ability to reduce wear could be evaluated by comparing results to the base oil and between the various polymer analogs. On average, all analogs except AW-3 and AW-5 exhibited less wear than the base oil, indicating that the new compounds can provide wear protection. Also, since AW-3 is the most nonpolar analog and displays the highest wear among the polymer candidates, the results suggest polarity plays a substantial role in the ability of polymers to reduce wear. The lowest wear among the polymer analogs is exhibited by AW-1, AW-2, AW-4, and AW-6. Of these, the first three are the

most polar of the six analogs tested, which supports the hypothesis that polar polymers are more effective at reducing wear. However, AW-6, one of the more polar analogs tested, also exhibited lower wear. This may be explained by its relatively low  $M_w$ ; the  $M_w$  of AW-6 is half that of the next smallest polymer. Therefore, these results indicate that low molecular weight and low polarity may enable polymer to improve wear performance. This may be a direction to pursue in future research to identify polymers that can decrease wear as much as the anti-wear containing fully-formulated oil.

Thus, this study showed that the polymers exhibited behavior better than the base oil without polymer and comparable to that of the benchmarks. This indicates that the polymers are able to moderately decrease friction, without the need for friction modifiers that are present in most lubricant formulations. Lastly, the wear results showed the polymers were not able to decrease wear as much as the fully-formulated oil which contained an anti-wear additive. However, several of the polymers exhibited better wear than the base oil alone. Further, comparison of the results between the various polymers suggests that lower molecular weight and enhanced polarity was beneficial for wear reduction. This indicates that the analogs may be further tuned to exhibit wear performance comparable to that of the fully-formulated benchmark.

## Chapter 5. Dry Film Lubricants

### 5.1 Introduction

Dry films are solid state lubricants that are used as lubricating media when the operating environment is extreme i.e., very high or very low temperature, vacuum or highly corrosive for liquid lubricants to function effectively or simply because it is not feasible. Examples of applications range from consumer devices like disk drives to industrial components like bearings and engine parts. Another area of application is in deep space missions to outer solar system planets where there is little source of energy to spare towards maintaining liquid lubricants at their normal operating temperatures. There are several solid lubricants currently in use including soft metals like Ag, Au, Sn, Cr and Ni, transition metal dichalcogenides (TMDs) like  $\text{MoS}_2$ ,  $\text{WS}_2$ , Graphite, polymer composites of PTFE and PE, Diamond Like Carbon (DLC), carbides of Ti and W, oxides of Al, Ti, Zn [123] etc. Most of these can be applied on surfaces in the form of coatings with a few exceptions, for example, PTFE, owing to its high wear rate. In the following we will discuss some of these lubricants and their respective categories.

### 5.2 Carbon-based lubricants

Graphite is one of the most well-known examples of solid lubricants, exhibiting a low coefficient of friction due to its stacked-sheets like crystal-structure with weak van der Waals forces holding the stack together [35]. These sheets are in a hexagonal lattice structure, with the carbon atoms at each vertex of the hexagonal rings held together by strong covalent bonds, see Figure 5.1.

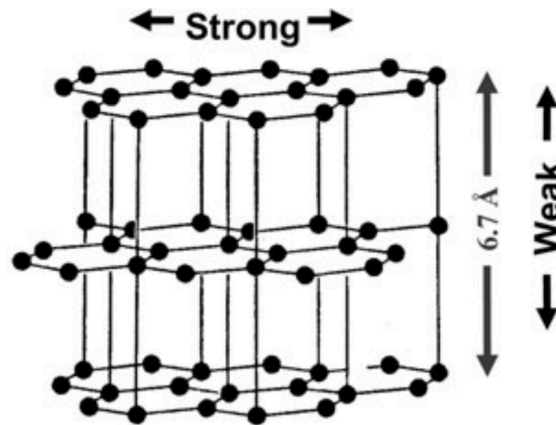


**Figure 5. 1.** Crystal structure of graphite showing ABAB stacking [35].

Presence of humidity and oxygen are known to benefit interlamellar shear particularly when these basal planes get damaged during sliding. Cleaved



basal planes create highly reactive edge sites, resulting in increased adhesion with the counter-body, causing increased friction. It has been proposed that presence of water vapor helps counter this friction increase due adsorption of water molecules passivating such edge sites [124, 125].

Diamond-like carbon (DLC), in contrast to graphite, is an amorphous carbon material having high hardness, wear resistance, elastic modulus and in some specific conditions, low friction. DLCs exhibit a large range of friction coefficients from 0.01 to 0.5 depending on conditions including contact pressure, speed, temperature, and environment. For example, hydrogen-free DLCs perform with low friction coefficient of 0.1 in humid conditions, whereas hydrogenated DLCs perform best in dry conditions. Pure DLCs exhibit very high compressive residual stresses, and low toughness and are thus doped with light weight elements including hydrogen, nitrogen, silicon and silicon oxide, and some transition metals including Cr, W and Ti which form metal carbides to improve strength, wear resistance and hardness.

### 5.3 Polymers

One of the most popular low friction polymers is polytetrafluoroethylene, referred to as PTFE with a typical coefficient of friction of 0.1 on steel surfaces [126]. It lubricates the contact by forming a transfer film on the counter-body and slides over itself with low friction. However, in neat form, it has poor wear characteristics with a high wear rate of  $K \sim 7 \times 10^{-4} \text{ mm}^3/(\text{N} \cdot \text{m})$  [127] making it difficult to achieve both low friction and wear. It has low surface energy and thermal conductivity that causes melting due to heat build-up, limiting its use to low-speed applications. To address its poor wear resistance, fillers of metallic oxides are generally added to the PTFE matrix which improve its wear performance by forming a strongly adhering tribo-film on the counter-body. PTFE is also used in the form of filler material itself, as fibers or powder, in composites, for example Ni-PTFE composite films are used as dry film lubricant [128].

### 5.4 Transition metal dichalcogenides (TMDs)

TMDs are known for their unique properties due to their high degree of anisotropy of layered crystal structures. These materials exist in the form  $\text{MX}_2$ , where M is a transition metal (Mo, W, Nb) and X can be any chalcogen from S, Se and Te [129]. Their layered crystal structure is especially suitable for tribological applications in the form of solid lubricants or DFLs, where, weakly held basal planes are able to slide over one another without much resistance. Of these,  $\text{MoS}_2$  and  $\text{WS}_2$  are more popular for their low friction characteristics

than for example,  $\text{NbS}_2$  and  $\text{NbSe}_2$ , as they suffer from poor lubrication properties due to a different electronic structure compared to  $\text{MoS}_2$  [130]. Both  $\text{MoS}_2$  and  $\text{WS}_2$  exhibit very low friction and long wear life in vacuum or dry oxygen free conditions and suffer from poor performance in the presence of oxygen and water vapor. Often TMDs are doped with other elements, for example, Au,  $\text{Sb}_2\text{O}_3$ , Ni, Ti, Co etc., to increase their useability in different environments. However, the mechanisms through which dopants improve the host properties are still unclear and are an active area of research.

Due to its excellent friction and wear life characteristics in vacuum, sputtered  $\text{MoS}_2$  is still widely preferred for lubricating space components. Examples of some aerospace components coated with  $\text{MoS}_2$  based DFL (Microseal 200-1) are shown in Figure 5.2. However, mechanical systems used in spacecraft, containing these coated components, are stored or ground-tested in lab or transported to launch site, sometimes in fully assembled condition. These activities are known to degrade the tribological performance of DFLs coated on these components exacerbated by exposure to atmospheric oxygen and humidity [131]. Due to the unavoidable nature of these activities, it is crucial to quantify the extent of coating degradation that has a direct effect on the functional life of the coating in space where it is expected to perform.

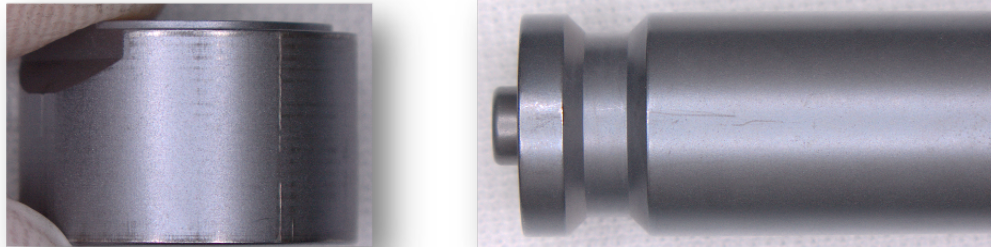


**Figure 5. 2.** Showing aerospace components coated with  $\text{MoS}_2$  based DFL, Microseal 200-1.

To do this, it is imperative to first study the wear behavior of  $\text{MoS}_2$  experimentally, in earth-ambient environment at application specific load and speed conditions. This is a necessary first step towards the ultimate goal of being able to estimate the loss of ‘useful’ coating life during ground operations and developing a cumulative coating damage model for a duty cycle consisting of a combination of ambient and vacuum operations. This would help us effectively predict the failure of these coatings during their operation in space after a given number of cycles of operations on earth.

## 5.5 Undoped and Ni-doped MoS<sub>2</sub> Wear Mechanism Study

### 5.5.1 Introduction

MoS<sub>2</sub> has a long history as a lubricant [132] and is currently used both in space and terrestrial applications as an additive in greases and lubricating oils, and as a DFL [133]. The lubricity of MoS<sub>2</sub> is provided by its crystal structure where stacked layers of MoS<sub>2</sub> basal planes (002) are held together by weak interplanar van der Waals attraction which is easily overcome when the layers experience shear [134]. There are various techniques of fabricating MoS<sub>2</sub> dry films, including burnishing, sputtering, resin bonding and impingement. However, sputtered MoS<sub>2</sub> coatings are preferred for space applications [135] due to their tribologically superior performance in the absence of oxygen and humidity [136], good adhesion to substrates [137, 138] and absence of any binding agent that can outgas in vacuum conditions [139]. In a lab environment, the vacuum of space is often approximated by testing in dry nitrogen [140–147]. Dry nitrogen simulates space vacuum conditions that are devoid of oxygen, water vapor and other elements that might affect the tribochemical processes occurring at the sliding interface [148]. Sputtered MoS<sub>2</sub> films exhibit excellent tribological performance in dry nitrogen with very low coefficient of friction (CoF) [149] and long wear life [141].

Despite the outstanding properties of sputtered MoS<sub>2</sub> coatings in environmental conditions devoid of oxygen and humidity, its tribological performance degrades significantly in ambient conditions [146, 150–154]. This degradation is often attributed to oxidation resulting in MoO<sub>3</sub> and MoO<sub>2</sub> byproducts which impede the smooth sliding of MoS<sub>2</sub> basal planes. However, the topic is still a subject of debate and other mechanisms have been proposed, including water-restricted-growth of shear-induced highly ordered tribo-films [146, 155] and viscous friction due to water molecules between basal planes [156, 157]. Further, it was shown that water and oxygen in the atmosphere affected friction differently [142]. At room temperature, atmospheric oxygen had very little impact due to a low rate of oxidation, whereas physisorption and diffusion of water molecules increased friction. However, the opposite was observed at higher temperatures (>100 °C) where the thermal energy-driven oxidation rate exceeded the wear-driven surface oxide depletion rate, resulting in a net increase in oxidation byproducts and higher friction, whereas water molecules desorbed readily and had little role to play [142].

The microstructure of sputtered MoS<sub>2</sub> is understood to play a significant role in its tribological behavior as well as its resistance to environmental conditions. Sputtered MoS<sub>2</sub> is known to have two possible morphologies,

referred to as Types I and II, depending on the sputtering technique employed [158]. Type II consists of basal planes oriented parallel to the substrate resulting in dense packing and a low fraction of exposed edge sites. Type I morphology consists of basal planes oriented perpendicular to the substrate surface resulting in high porosity and exposed reactive edge sites. This Type I growth morphology is believed to have three distinct zones: starting from the substrate, there is a ridge structure, followed by a dense equiaxed zone, and finally a region of vertically oriented crystallites or columnar structures [159].

Most commercially produced MoS<sub>2</sub> DFLs are expected to exhibit Type I morphology due to the Direct Current (DC) sputtering technique used to produce them.

Many previous studies have characterized the friction and wear performance of Type I MoS<sub>2</sub>. The Type I microstructure causes an oxidation-driven friction increase, beginning during the run-in period when the columnar crystallites are oriented perpendicular to the substrate, before being forced to reorient in the direction of sliding, trapping the oxidation byproducts between the crystallites and impeding shear [159, 160]. The friction after run-in depends on the rate of thermally driven formation of surface oxides and the rate of depletion of these oxides due to wear from the contact zone [142]. The wear behavior of Type I sputtered MoS<sub>2</sub> coating was studied by Spalvins [161] who showed that, at the onset of sliding, the vertical MoS<sub>2</sub> lamellae are first reoriented in the sliding direction and then later fracture at the base where they are attached to the equiaxed zone. Another study showed that basal plane reorientation occurs early in the sliding process, within 5% of the total wear life of the coating [139]. Based on this, it was proposed that the detached lamellae were depleted from the contact zone and subsequently did not contribute to the operational life of the coating. Lubrication after that point was therefore proposed to be provided by a thin ( $\approx 200$  nm) lubricating film remaining on substrate after the lamellae detached [161].

Co-depositing or doping certain metals with MoS<sub>2</sub> is known to affect the coating microstructure and can alleviate the detrimental effects of humidity and oxygen on the tribological behavior of sputtered coatings. Dopants are believed to improve the tribological properties of sputtered MoS<sub>2</sub> films through different mechanisms, including increased oxidation resistance [141, 162, 163] and increased hardness, [164–170] depending on the dopant material used. In an early study, Stupp [171] evaluated multiple transition metal dopants and found Cr, Co, Ni and Ta to be the best overall performers in terms of friction, wear life, ease of co-deposition and aging-related degradation.

Particularly for space applications, Ni is a preferred dopant [172] due to its ability to mitigate the increase of friction at low temperatures [173] and its low cost and availability [171]. In one study, [141] higher concentrations of Ni dopant (up to 20% by weight) were investigated and it was found that, above 11%, the coating becomes brittle and fails prematurely. For maximum coating life and stable friction, 5-7% Ni was recommended [171]. Co-depositing MoS<sub>2</sub> with Ni has been found to affect the morphology of the film as well. Specifically, pure MoS<sub>2</sub> and MoS<sub>2</sub> with 3% Ni showed Type I morphology, whereas doping with 9% or more Ni resulted in a "Zone T" microstructure which has a non-porous fibrous interior and flat tops [174]. However, how these changes in morphology due to Ni doping affect coating life is not known.

In summary, sputtered MoS<sub>2</sub> DFLs are preferred for space applications due to their excellent tribological performance in vacuum conditions devoid of oxygen and humidity. Sputtering results in MoS<sub>2</sub> microstructures that are believed to provide long life through processes that occur during run-in. Also, MoS<sub>2</sub> DFL performance, particularly friction at low temperatures, has been shown to improve with Ni doping. Although this improvement is attributed to the microstructure, the effect of Ni dopant on the morphological changes that occur during run-in is not understood. To address this, in the present study, we characterized the friction and wear behavior of sputtered doped and undoped MoS<sub>2</sub> films at different pressure and speed conditions. Long tests were run to determine coating life, as characterized by a drastic friction increase reflecting complete coating failure. Then, short tests were run to characterize and understand the run-in period during which it has been proposed that microstructural evolution occurs that plays a critical role in determining coating life. Results were analyzed in terms of both coating thickness, which is often assumed to correspond to life, and friction, reflecting actual useful life. Finally, findings were interpreted by analysis using microstructural and material characterization tools, including scanning electron microscopy (SEM) and energy dispersive spectroscopy (EDS).

### 5.5.2 Methodology

#### *Materials*

Two coatings were investigated in this study: undoped MoS<sub>2</sub> and  $\approx 7\%$  wt Ni-doped MoS<sub>2</sub>. Both types of coatings were fabricated via DC sputter deposition with electron beam assist. Stainless steel (440C) disks of 0.25" thickness, hardness 45–50 HRC or 58–62 HRC with average surface roughness of 80 nm were used as substrates. The coating thickness varied slightly from disk to disk but was in the range of 0.8–2.0  $\mu\text{m}$  for all disks. A burnishing process was

applied to the coated disks to obtain a smooth reflective surface finish. Burnishing involved sliding a wool-like material against the sputtered disks until coated surface had a uniform appearance and there was no more loose debris coming off the surface onto the wool.

### *Test Conditions*

Tribological testing to measure friction and wear was performed using an Rtec Instruments tribometer and white light interferometer. Unidirectional sliding tests using a ball-on-disk set-up as described by the ASTM G-99 standard were performed to measure CoF. 440C stainless steel balls with Rockwell C60 hardness were used as the counter-body. The radius of the circular sliding path on the disks was between 15 and 30 mm. All tests were carried out at room temperature and ambient air conditions with relative humidity ranging between 30% and 50%.

Table 4 shows the load and speeds used in the testing and the calculated maximum Hertz contact pressures. Note that the sliding speed was also varied to simulate the inverse stress (analogous to torque) and speed relationship typical in a gear-driven system. Two types of sliding tests were performed in this work, end-of-life and run-in. End-of-life tests were used to determine the wear life in terms of number of revolutions/cycles to failure. This test involved sliding on the coated disk until the CoF increased above  $\approx 0.4$ , became characteristically noisy and did not drop back to lower values. Run-in tests were short duration sliding tests (between 5 and 250 cycles) used to study the evolution of wear and wear mechanisms. Only 300 and 1100 MPa contact pressures were studied for run-in. Another distinction between the end-of-life and run-in tests is that, in the former, the disk was already rotating before the ball was pressed against it whereas in the latter, the disk was rotated after loading. Three repeat end-of-life tests and four repeat run-in tests were performed per case.

**Table 4.** Experimental parameters used in the ball-on-disk tests. High pressures are matched with low speed, and vice versa, to mimic the operating conditions of a gearing system.

Normal Load (N)	Contact Pressure (MPa)	Sliding Speed ( $\text{ms}^{-1}$ )
0.27	300	1
2.5	500	0.77
5.1	800	0.44
13.3	1100	0.1

## Analysis

3D surface images of the wear tracks were obtained using a white light interferometer. The interferometer was calibrated to be within 1% of reference values. Wear depth was measured from 2D profiles taken at different positions on the wear track using the image processing software Gwyddion. The mean wear depth at four angular positions on each wear track was calculated and reported with error bars representing the standard deviation from the mean. EDS using EDAX Genesis spectrometer attached to a FEI Quanta 200 Environmental scanning electron microscope (SEM) was used to obtain elemental composition in wear tracks. The microstructure of the coating before and after sliding was characterized using a Zeiss Gemini 500 SEM.

### 5.5.3 Results and Discussion

The microstructures of undoped and Ni-doped MoS<sub>2</sub> coating surfaces were characterized before tribological testing. The burnishing process applied after sputtering flattened the tops of the coatings, so images were taken at scratches on the burnished layer to reveal the microstructure of the material. The SEM micrographs in Figure 5.3 show that the undoped and Ni-doped coatings have similar microstructures, with highly columnar crystallites consistent with Type I coatings. The microstructures shown here are representative of images taken on multiple samples imaged at several different locations on the surface.

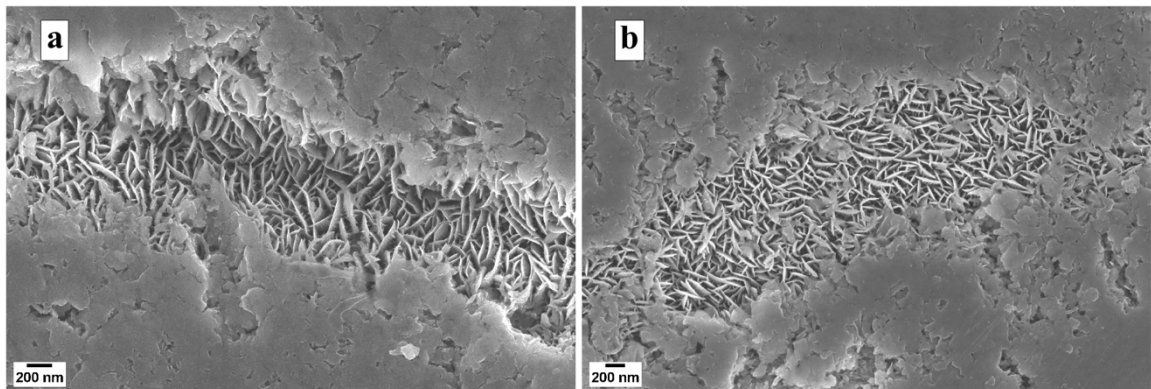


**Figure 5. 3.** SEM micrographs of a) undoped and b) Ni-doped MoS<sub>2</sub> coating morphologies showing columnar structures consistent with Type I coatings and flat tops resulting from burnishing.

The performance of the undoped and doped MoS<sub>2</sub> coatings was measured at four different pressure/speed conditions. In the end-of-life tests, the CoF during sliding was tracked until the coating failed completely. Representative traces of the CoF as a function of number of cycles of rotation of the disk for undoped and Ni-doped coatings are shown in Figure 5.4. For these cases, the number of cycles until failure, that is, wear life, is greater for the lower contact

pressure/higher speed conditions. Also, the results indicate that Ni-doped coatings have longer life than the undoped coatings and that difference appears to be most significant at the lower contact pressures.

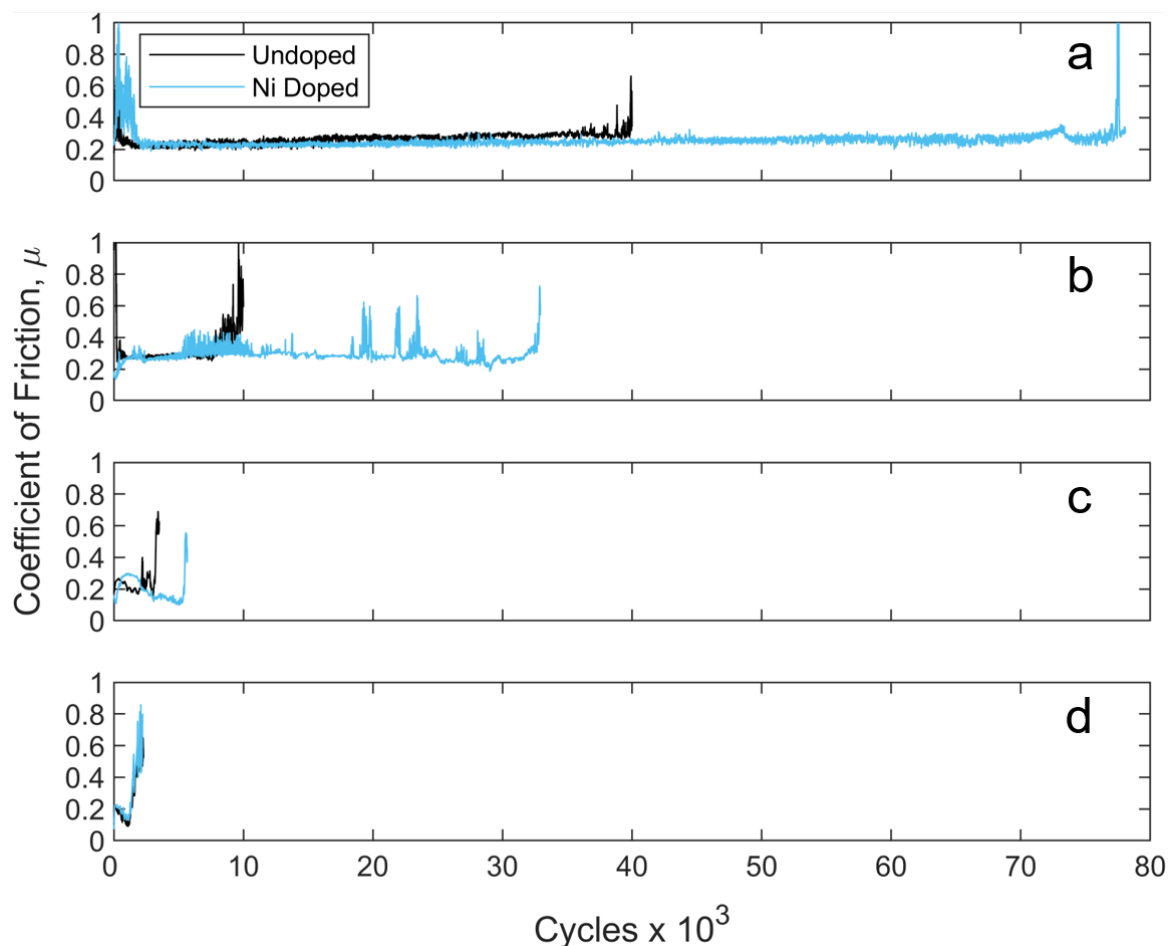


**Figure 5. 4.** Representative CoF traces at a) 300 MPa and 1 ms<sup>-1</sup>, b) 500 MPa and 0.77 ms<sup>-1</sup>, c) 800 MPa and 0.44 ms<sup>-1</sup>, and d) 1100 MPa at 0.1 ms<sup>-1</sup> for undoped and Ni-doped MoS<sub>2</sub> coatings run until coating failure.

Coating failure was identified as the CoF exceeding and remaining above  $\approx 0.4$ . We confirmed that the coating life identified using this criterion was reasonable by analysis of the elemental composition of unworn, partially worn and fully worn regions on the surfaces using EDS. The results for an undoped coating are shown in Figure 5.5. In this case there are two wear tracks shown: the track on the left corresponds to midway through a test (prior to failure) and the one on the right was taken at the end of a test (after failure). It is clear from the compositional maps of molybdenum (Mo) and sulfur (S) that the MoS<sub>2</sub> coating is fully worn on the right wear track with negligible Mo and S signal, while both Mo and S are observed on the left wear track obtained prior to



failure. This is confirmed by observation of prominent iron (Fe) and chromium (Cr) signals from the steel substrate on the right wear track, after failure. A similar EDS compositional map of unworn and full worn (after coating failure) regions of Ni-doped coating is shown in Figure 5.6.

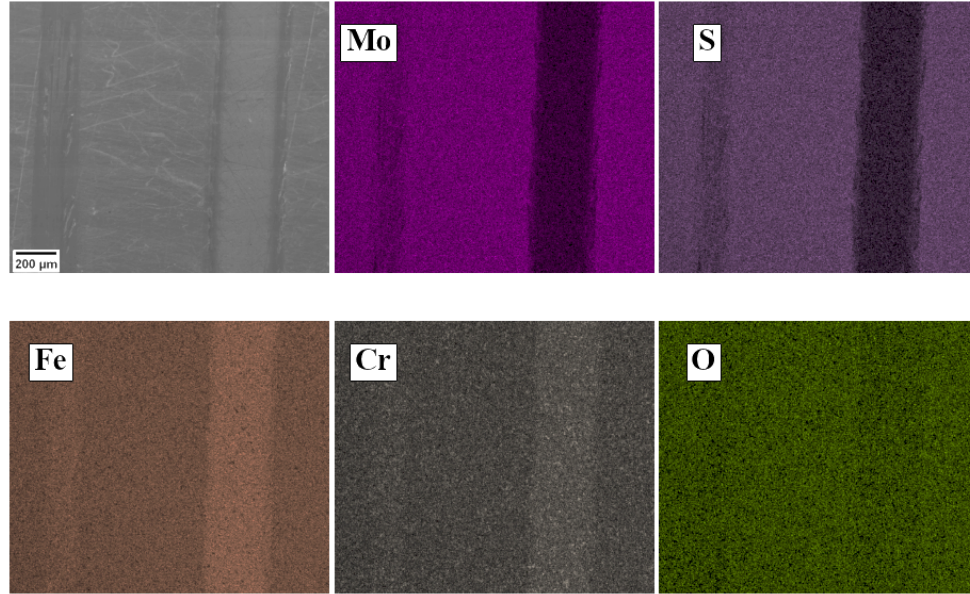


**Figure 5. 5.** EDS compositional maps showing partially worn (left wear track), unworn (center region), and fully worn (right wear track) regions of undoped MoS<sub>2</sub> coating. The partial and fully worn tracks were generated in sliding tests at 300 MPa contact pressure after 18000 and 80000 cycles, respectively.

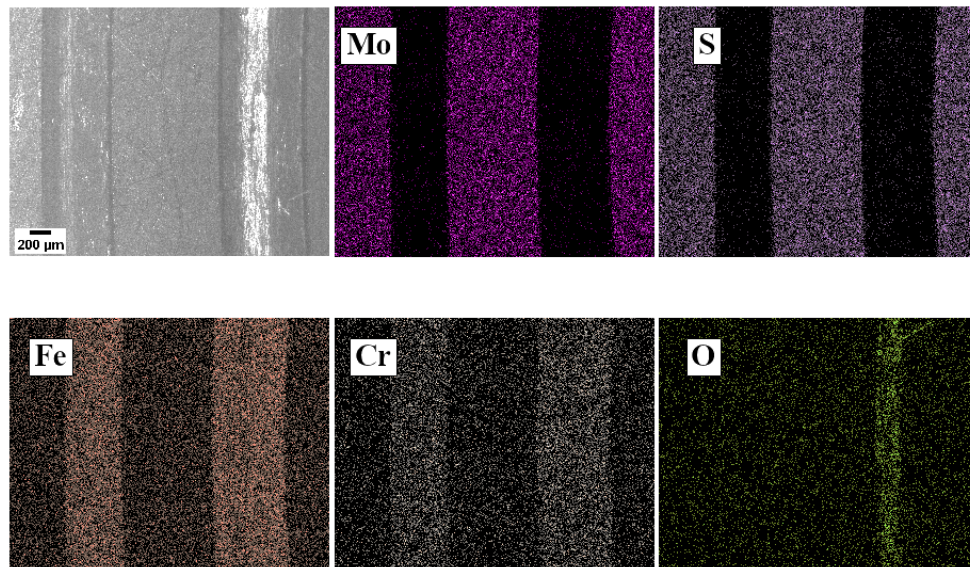


**Figure 5. 6.** EDS compositional maps showing two fully worn wear tracks and unworn regions on a Ni-doped MoS<sub>2</sub> coating. The left and right tracks were generated in sliding tests at 500 MPa contact pressure after 34 000 and 43 000 cycles, respectively.

As expected, both fully worn tracks show have negligible Mo and S signals, indicating the coating has been removed and indicating prominent Fe and Cr signals from the steel substrate.

Wear life was measured from long duration tests at each pressure/speed condition for undoped and Ni-doped MoS<sub>2</sub> coatings. The results are shown in Figure 5.7, where the symbols represent the mean of three tests and the error bars reflect the standard deviation. The results indicate that Ni dopant improves the life of the MoS<sub>2</sub> coating at the lower contact pressures of 300 and 500 MPa, but the difference between doped and undoped coating life is not statistically significant at the higher contact pressures of 800 and 1100 MPa. Also, the life of the Ni-doped coatings exhibits higher variability than the undoped coatings, particularly at the lower pressures. This may be attributed to non-uniformity in the distribution of Ni dopant in the coating on individual samples or from sample to sample, or greater variability in coating thickness for the doped samples.

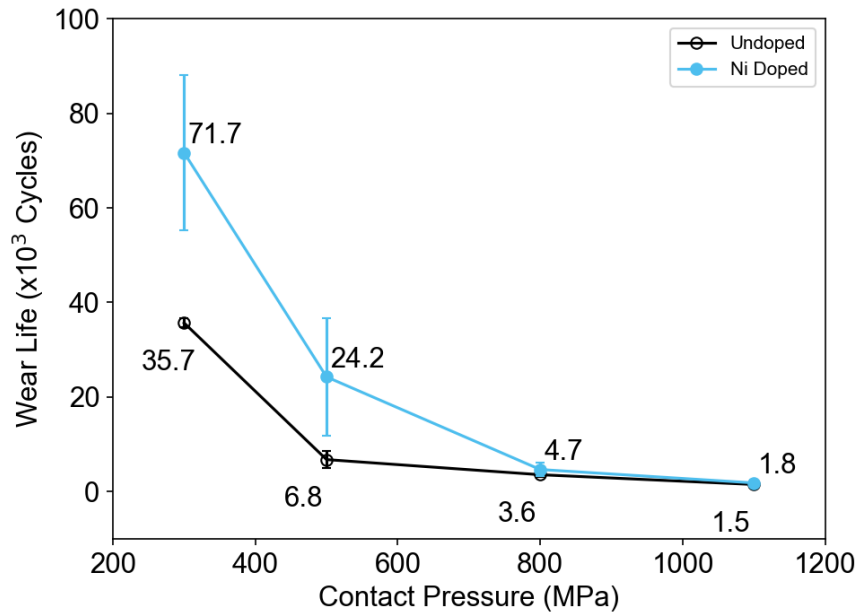


**Figure 5. 7.** Wear life of undoped and Ni-doped MoS<sub>2</sub> at different contact pressure/sliding speed conditions. The results are plotted against pressure on the abscissa, but the speed is also different for each case. Ni dopant improves wear life compared to the undoped samples at low pressures.

Short duration tests were performed to study coating wear during run-in as a means of understanding wear mechanisms and how they are affected by the Ni dopant. For this, the rotating disk was stopped at different intervals of sliding and the 3D surface topography of the wear track at a fixed angular position was measured using an interferometer. Then, the sliding was restarted from the location at which it was stopped. This technique enabled

tracking of the evolution of the coatings during the wear process. In these tests, the coatings did not fail, as determined by the friction coefficient criterion used in the end-of-life tests. Representative cross-sections of the wear track obtained from the interferometer images at different number of cycles during run-in at the highest and lowest pressure are shown in Figure 5.8.

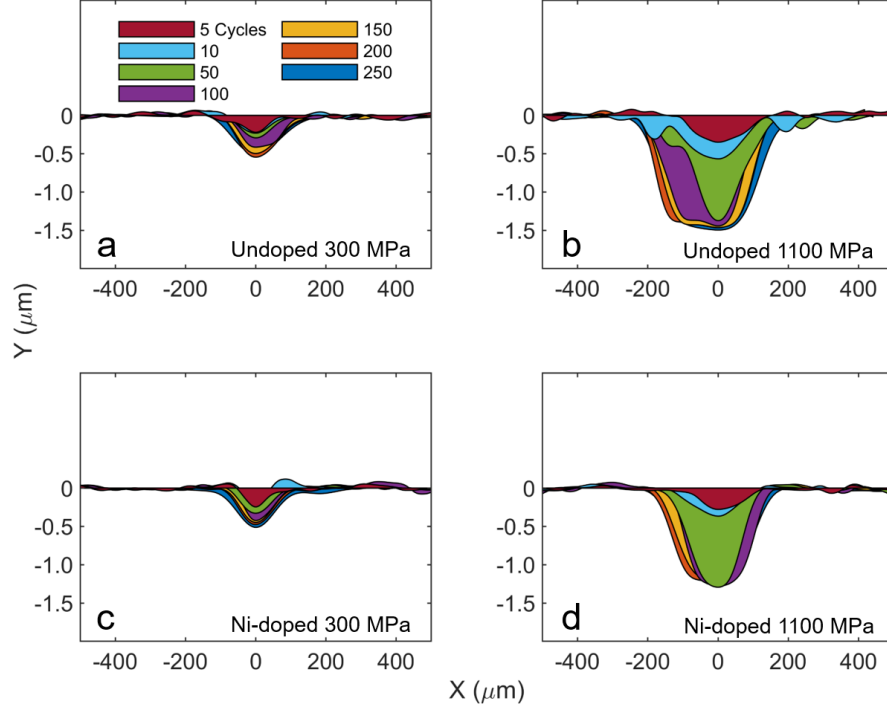


**Figure 5. 8.** Wear profiles for (a) undoped MoS<sub>2</sub> at 300 MPa and 1 ms<sup>-1</sup>, b) undoped MoS<sub>2</sub> at 1100 MPa and 0.1 ms<sup>-1</sup>, c) Ni-doped MoS<sub>2</sub> at 300 MPa and 1 ms<sup>-1</sup>, and d) Ni-doped MoS<sub>2</sub> at 1100 MPa and 0.1 ms<sup>-1</sup> showing the evolution of the wear tracks during the run-in tests.

These results indicate that wear depth generally increases with number of cycles and is greater for the higher pressure. The wear depth was measured as the maximum depth of wear profiles such as those in Figure 5.8 from four tests on two different samples. The wear depth was then normalized by the coating thickness for each disk such that a normalized wear depth of 1 indicates that the coating has been completely removed. The average normalized wear depth is plotted as a function of number of cycles in Figure 5.9, where error bars represent the standard deviation. As expected, in all cases, the wear depth increases with number of cycles and is larger at the higher pressure. Also, notably, at either pressure, the wear tracks on the Ni-doped MoS<sub>2</sub> are shallower than those on the undoped MoS<sub>2</sub>. This agrees qualitatively with the longer life of the Ni-doped coatings observed in the end-of-life tests at low pressure.

Figure 5.9 also reveals different run-in behavior at low and high pressures. Specifically, the wear rate, that is, rate of change of depth with cycles, is nearly constant throughout run-in at the low contact pressure. In contrast, at high pressure, the wear rate is initially very rapid but then decreases after about 100–150 cycles to a value similar to that observed at the low pressure. For the undoped coating at 1100 MPa, the normalized wear depth is unity (depth = coating thickness) after only 180 cycles. For the other cases, we used the rate of decrease of normalized wear depth with cycles after 150 cycles to estimate the number of cycles at which the normalized wear depth would reach unity. It was found that the wear depth would be equal to the coating thickness after  $940 \pm 374$  cycles for the undoped coating at low pressure and  $1226 \pm 787$  and  $725 \pm 274$  cycles for the Ni-doped coating at low and high pressure, respectively. This approximation assumes a linear wear rate, but we confirmed that the trend remained linear with additional tests to 1000 cycles on undoped coatings at high stress. Further, even if the rate becomes slightly sub-linear, these results predict that the wear depth would still exceed the coating thickness after hundreds of cycles, whereas the wear life was on the order of tens of thousands of cycles in Figure 5.7. This means that, for most of the life of the coating, very little of the “bulk” material is present in the wear track.

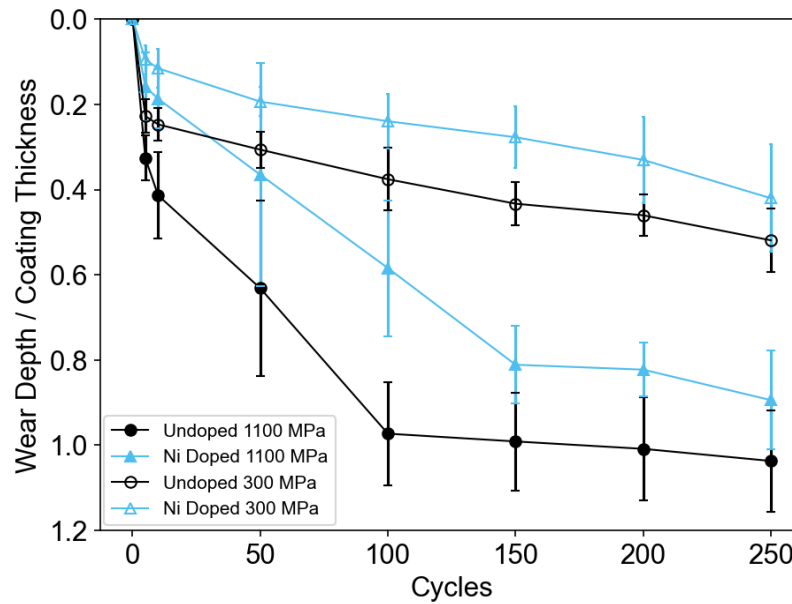


**Figure 5. 9.** Wear depth as a function of cycle during run-in tests at 300 and 1100 MPa contact pressures on undoped and Ni-doped MoS<sub>2</sub>. Wear tracks are shallower (less wear) on the Ni-doped sample at both pressures.

The implication of the above analysis is that the sliding contact is lubricated by local MoS<sub>2</sub> flakes or debris that form as the coating is worn. This was



supported by the observation of MoS<sub>2</sub> on the ball observed via optical microscopy (not shown) after tens of thousands of cycles. We also characterized the coatings using SEM at the initial stages of run-in. Representative SEM micrographs of the wear tracks on the undoped and Ni-doped MoS<sub>2</sub> films after 10 cycles at 1100 MPa and 0.1 ms<sup>-1</sup> are shown in Figure 5.10. On both the doped and undoped samples, we observe significant wear, even after only 10 cycles. However, the wear mechanism appears to differ between doped and undoped. Specifically, while both coatings exhibit cracking, there is also delamination in the case of the Ni-doped sample (Figure 5.10b) that is not observed on the undoped sample (Figure 5.10a). Based on the microstructure of these Type I coatings, it is presumed that the columnar zone is cracking and/or delaminating. This difference in failure mode has also been reported in a previous study where sputtered MoS<sub>2</sub> with 9% Ni exhibited more delamination in indentation tests than pure or low Ni concentration MoS<sub>2</sub> [175].

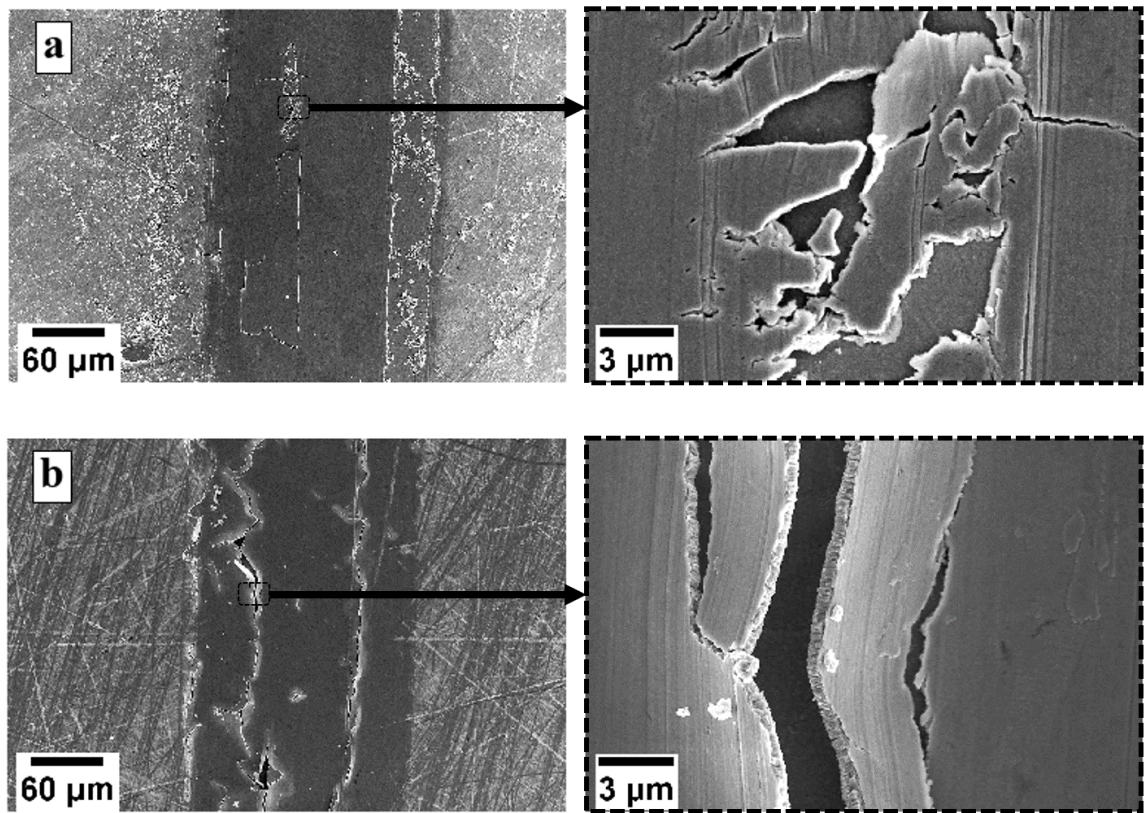


**Figure 5. 10.** SEM micrographs of (a) undoped and (b) doped MoS<sub>2</sub> coatings after 10 cycles at 1100 MPa and 0.1 ms<sup>-1</sup>. The images on the right show close-up views of the partially worn material. These images show representative features where the undoped coatings exhibit cracking and delamination.

It has been suggested that the columnar zone of Type I MoS<sub>2</sub> sits on a lower layer of material, called the equiaxed zone [159]. SEM images of the regions between the cracks on the doped and undoped coatings after 10 cycles are shown in Figure 5.11. These examples, that are representative of images taken at various locations on the worn surfaces, exhibit clear differences between the coatings. Notably, the material under the cracked or delaminated columnar zone for the undoped coating is smooth while that for the Ni-doped coating is rough. This may be attributable to differences in the microstructure of the doped coating that arise during sputtering. Alternatively, it could be related to the delamination that was observed only for Ni-doped coatings and may have occurred through breaking of columnar structure, leaving partial columns on the surface.

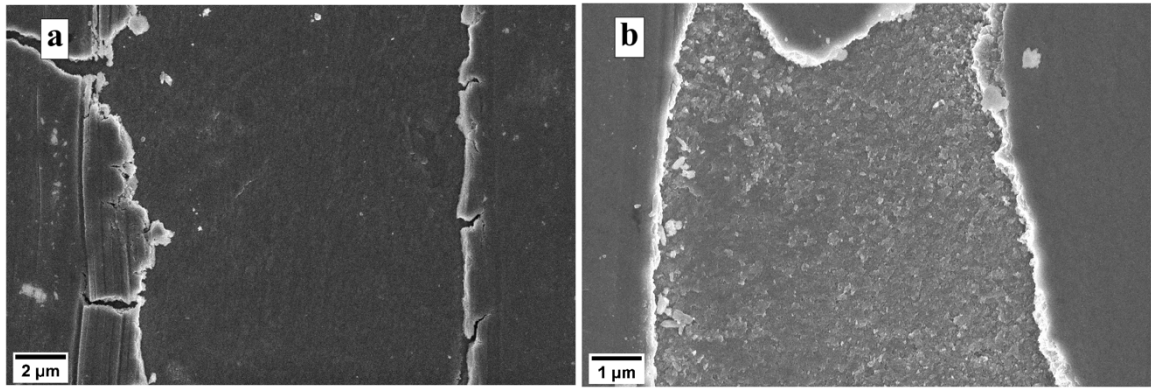


**Figure 5. 11.** SEM micrographs of the regions between the cracked or delaminated columnar zone for (a) undoped and (b) Ni-doped MoS<sub>2</sub> coating after 10 cycles at 1100 MPa and 0.1 ms<sup>-1</sup>. The material underneath the failed columnar zone is distinctly rougher for the Ni-doped coating.

The fact that the wear depth appeared to exceed the coating thickness after very few cycles (compared to the wear life) suggested the contact was lubricated by localized MoS<sub>2</sub> flakes or debris. Based on the images in Figure 5.10 these flakes could have formed through cracking or delamination of the columnar zone. Representative images of some of flakes from tests run to 10 or 250 cycles are shown in Figure 5.12. First, in all cases, the thickness of the flakes (as approximated from these images) is on the order of a few hundred nanometers. This is less than the expected coating thickness, suggesting that the columnar zone gets denser due to the contact pressure. Also, the flakes at 10 cycles (Figure 5.12a, b) appear to retain more of the original columnar structure (Figure 5.3) than the flakes imaged at 250 cycles (Figure 5.12c, d). This difference may be attributable to crystalline reorientation suggested in previous studies [139, 159, 160]. However, there is no obvious difference between the cross-sections of the flakes from the undoped (Figure 5.12c) and Ni- doped (Figure 5.12d) coatings.

The SEM evidence supports the hypothesis that most of the life of the coating is provided by flakes of material. However, these flakes must be supplied continuously throughout the life of the coating. Since the depth of the wear track exceeds the coating thickness at the high pressure, the flakes cannot be coming from the bottom of the wear track. Rather, it is likely that they are replenished from the sides of the wear track, that is, as the width of the worn region increases, additional cracking, and/or delamination provides newly available lubricious material. We tested this hypothesis by measuring the wear track width (full width at half maximum) during the run-in tests.

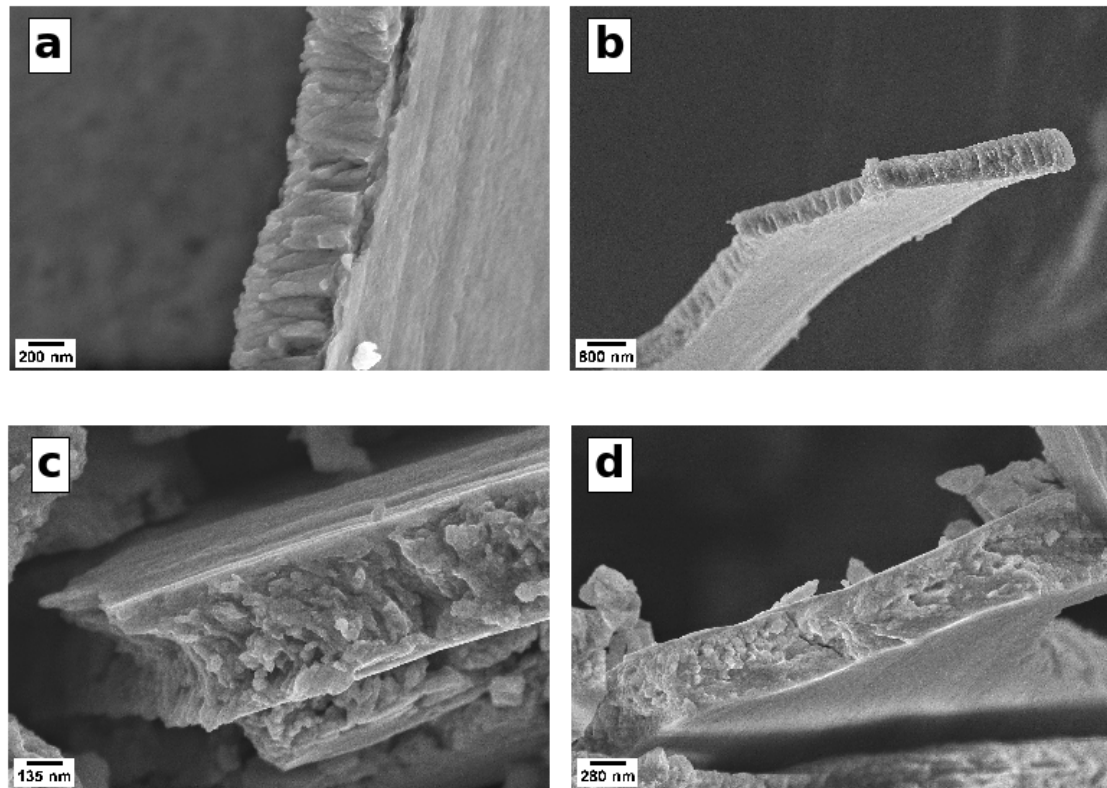


**Figure 5. 12.** SEM micrographs of dense flakes of MoS<sub>2</sub> within or near the wear track from run-in tests of (a, b) Ni-doped coatings after 10 cycles, (c) an undoped coating after 250 cycles, and (d) a Ni-doped coating after 250 cycles. All images from tests at 1100 MPa and 0.1 ms<sup>-1</sup>.

The results shown in Figure 5.13 indicate that wear width increases with cycles, but at a much slower rate than the wear depth in Figure 5.9. Note that, although the wear width appears to plateau after a few hundred cycles at 300 MPa, in fact the width continues to increase throughout the test (e.g., the widths of the wear tracks in the EDS images in Figure 5.5 are several times larger than the apparent plateau in Figure 5.13). Generally, the observation of increasing wear width is consistent with the hypothesis that worn material is gradually removed from the sides of the wear track to lubricate the contact.



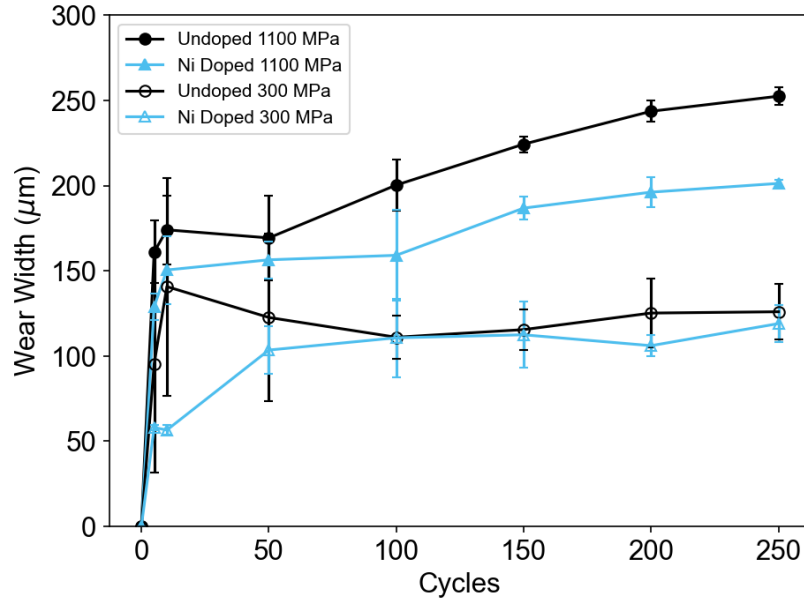


**Figure 5. 13.** Wear width as a function of cycle during run-in tests at 300 and 1100 MPa contact pressures on undoped and Ni-doped MoS<sub>2</sub>. Wear tracks widths are larger at the higher pressures. In all cases, the width increases gradually with sliding cycles.

All of the above suggests a mechanism by which MoS<sub>2</sub> coatings provide low friction and wear by generating flakes of lubricious material at the edges of the wear track. The remaining question is why Ni-doped coatings wear more slowly during run-in and have longer wear life at low pressures. One explanation is the Ni-doped coatings are harder, since increased hardness is one mechanism by which dopants have been proposed to improve the tribological performance of MoS<sub>2</sub> [171, 176]. However, the different failure modes observed in Figure 5.10 as well as the differences in the material underneath the cracked/delaminated columnar zone in Figure 5.11 suggest there may be another contributing factor. The observation that coating performance is enabled by flakes of worn material suggests that the Ni-doped coating generates more lubricious and/or longer-lasting flakes. Specifically, it is likely that delamination yields more and potentially larger and denser flakes of columnar material than cracking.

To investigate this hypothesis, we performed progressive load scratch testing following the ASTM C1624-05 standard. This test involves scratching the surface using a sphero-conical diamond indenter of radius 200 μm at normal load progressively increased from 5 to 80 N at a sliding speed of 10 mm min<sup>-1</sup>. The lateral force on the indenter was recorded and plotted against time as shown in Figure 5.14a. There is no abrupt change in the lateral force during any of these tests, indicating that either there was no “damage event” due to



coating failure or the coating failed at the onset of sliding. Also, the lateral force on the Ni-doped coating is slightly (although statistically significantly) lower than that on the undoped coating.

This difference was investigated using SEM and EDS of the scratched region. Representative images taken from the beginning of the scratch (around 5 N load) are shown in Figure 5.14b, c. From the SEM images, the difference in the wear modes of these coatings is apparent: the undoped coating is almost fully worn in the contact zone, whereas Ni-doped coating is still partly intact with some signs of delamination. This was confirmed by the elemental composition maps that show Mo remains in the scratched region only in the case of the Ni-doped coating; similarly, the Fe signal is much stronger for the undoped coating.

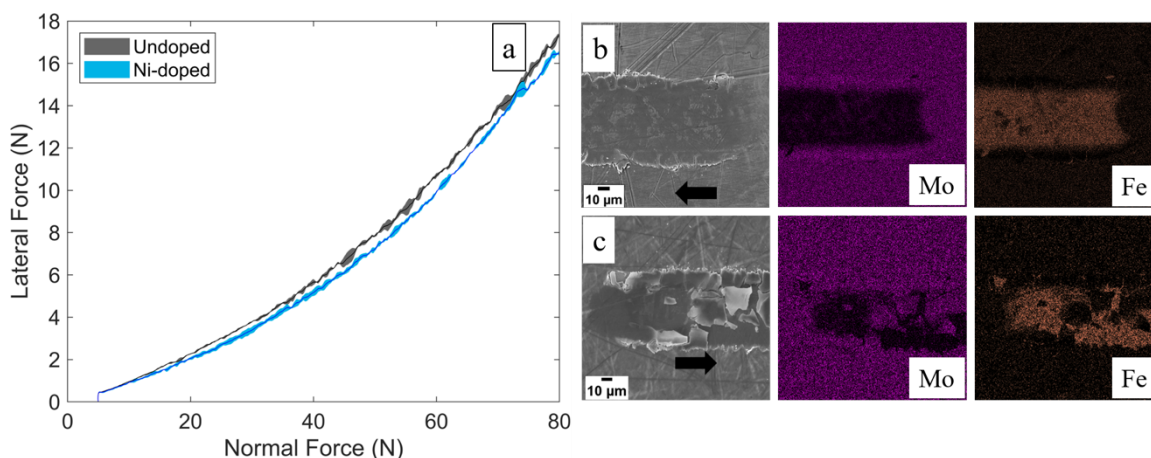


**Figure 5. 14.** (a) Average lateral force during progressive load scratch tests on doped and undoped samples. Lines represent the average of three tests and the band represents standard deviation. SEM images and Mo/Fe signals from EDS taken at the start of the test on (b) undoped (c) Ni-doped coatings.

SEM images taken later in the test at higher loads (about 62 N) are shown in Figure 5.15. These results confirm both the coatings are fully worn. In the middle of the wear track, both surfaces have semi-circular features oriented in the sliding direction that are the result of conformal accumulation of plastically deformed substrate material. However, the two surfaces differ at the edge of the wear track where there is more spallation and delamination for the Ni-doped coating. This corroborates the hypothesis that the Ni-doped coating generates more material from the sides of the wear track.

The evidence presented strongly suggests that the Ni-doped MoS<sub>2</sub> coatings have longer wear life because of their ability to generate more lubricious material from the sides of wear track. This mechanism is likely complemented

by increased hardness, as observed for doped MoS<sub>2</sub> coatings in previous studies.

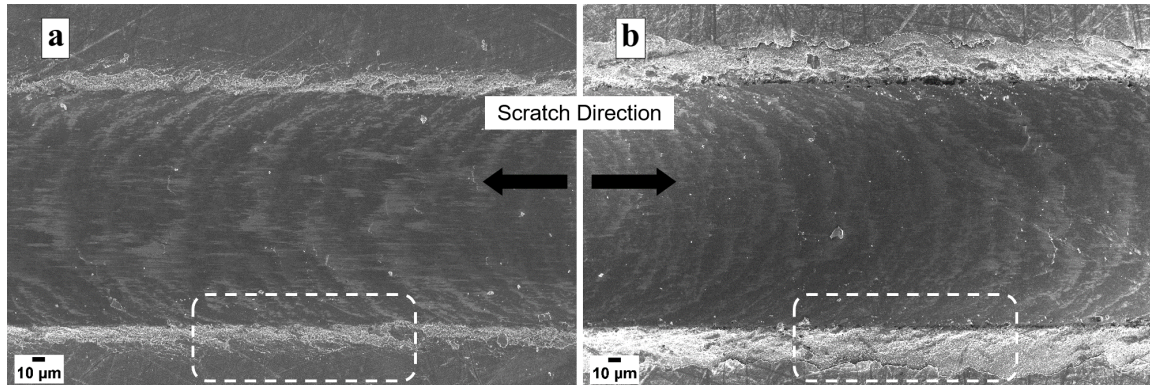


**Figure 5. 15.** SEM micrographs of (a) undoped and (b) Ni-doped MoS<sub>2</sub> coatings during a representative progressive load scratch test (at  $\approx 62$  N load). The doped and undoped coatings are distinctly different at the edges of the wear tracks (e.g., the regions identified by the dashed lines).

The complete proposed mechanism is illustrated in Figure 5.16. The columnar zone is compressed in the first few cycles and then begins cracking (undoped) or delaminating (Ni-doped), leading to the formation of lubricious flakes. Although the coating is worn through in the center of the wear track, the track width gradually increases with cycles, resupplying lubricating flakes to the contact over the remaining life of the coating.

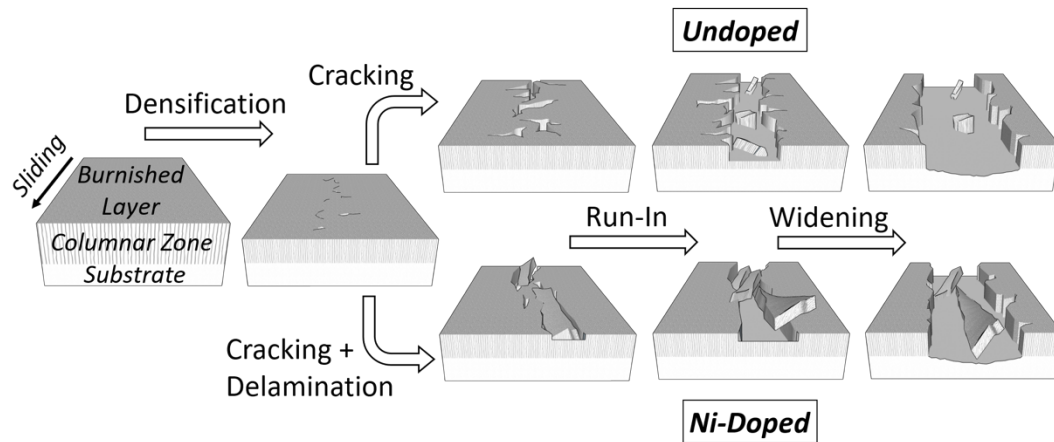


**Figure 5. 16.** Schematic illustration of the proposed wear process that occurs through densification followed by cracking and, for Ni-doped MoS<sub>2</sub>, delamination. The flakes generated during the cracking and/or delamination process lubricate the contact subsequently as they are continuously supplied as the wear track widens and more flakes are made available to facilitate sliding.

### 5.5.4 Conclusion

In this study, the effect of Ni dopant on wear life and morphological evolution of sputtered MoS<sub>2</sub> coatings was investigated. Tribological experiments at

different pressure and speed conditions were performed to measure and compare the wear life of Ni-doped and undoped MoS<sub>2</sub> coatings. The results showed that Ni dopant at  $\approx 7\%$  by weight concentration improved wear life of MoS<sub>2</sub> coatings significantly at low contact pressures. However, Ni-doped coatings exhibited higher variability in wear life than undoped coatings, possibly due to non-uniformity in Ni distribution or coating thickness in doped samples.

Similar tests were performed for short duration (5–250 cycles) at low and high-pressure conditions to study the evolution of wear during run-in. This process was characterized in terms of wear depth, wear width, and coating microstructure. At both low and high-pressure conditions, the wear depth either exceeded or was expected to exceed (based on extrapolation of the wear rate) the coating thickness early in the run-in process, suggesting that very little of the “bulk” material was left in the wear track for most of the life of the coating. This result implied that the contact was being lubricated by detached MoS<sub>2</sub> debris or flakes, which was supported by SEM micrographs showing cracked and/or delaminated coating in the wear track after the first 10 cycles. The gradual increase of wear width of the coating suggested that lubricious flakes of MoS<sub>2</sub> were supplied to the contact from the sides of the wear track as the width of the worn region increased.

SEM imaging suggested that the undoped and Ni-doped coatings exhibited different wear mechanisms, with the former wearing by cracking while the latter demonstrated cracking and delamination. Analysis of progressive load scratch tests confirmed that wear behavior differed between the doped and undoped coatings, particularly at the edges of the worn regions. The delamination exhibited by the Ni-doped coatings may explain its longer wear life since delamination yields more and possibly larger and denser flakes than those generated by cracking of undoped coatings.

More generally, the findings of this study illustrate that the wear life of MoS<sub>2</sub> coatings cannot be correlated to wear track depth, in contrast to the usual concept of wear for traditional engineering materials. Further, the results suggest a new mechanism by which dopants can extend MoS<sub>2</sub> DFL life, that is, facilitating delamination, that might be leveraged to further understand and then improve the performance of these materials. Lastly, the coating life estimates from this study can be further used in studying the consumption of ‘useful’ coating life during earth-ambient testing, which can allow us to estimate the remaining coating life in space operations.

## Chapter 6. Summary and Future Work

### 6.1 Summary

Novel friction and wear reducing strategies in different tribological contacts were studied in this work using experimental tools including tribometry, surface, material/microstructure, and mechanical characterization. Different approaches were utilized including surface engineering, new materials, multifunctional additives in base oil and, dry film lubricants.

In the surface engineering approach, the effectiveness of Ultrasonic Nanocrystalline Surface Modification (UNSM) as a pretreatment process for gas nitriding for improved scratch resistance was investigated. The scratch resistance of Ti6Al4V specimens, gas-nitrided at two temperatures (700 °C and 800 °C) with and without UNSM treatment was measured using scratch hardness tests. The results revealed that the scratch hardness of Ti6Al4V after nitriding at 800 °C with UNSM pretreatment was higher than that of the sample without pretreatment which possibly originated from a thicker nitride layer assisted by nano-grains formed due to UNSM process.

In a related study, wear resistance improvements of electropulsing-assisted UNSM (EP-UNSM) process were studied on NiTi alloy using ball-on-flat sliding wear experiments. The wear performance was compared with an UNSM specimen fabricated without electropulsing and a specimen without any surface treatment used as control. It was found that both UNSM and EP-UNSM resulted in higher wear resistance, however, electropulsing did not improve wear resistance over UNSM process. This is explained by the formation of fine local recrystallized grains in EP-UNSM specimen corroborated by optical microscopy images of NiTi cross-section. These local recrystallized fine grains, known to increase ductility due to high-density electrical pulses are the likely source of reduced wear resistance.

In the novel materials approach, a relatively new material known as 60NiTi was investigated for its friction and wear behavior sliding against itself in the presence of terrestrial and aerospace greases for space applications. A terrestrial general-purpose grease, and 4 aerospace greases were characterized using linear reciprocating sliding ball-on-flat tests and interferometry, optical microscopy and scanning electron microscopy tools were used to explain their tribological behavior. It was found that PFPE-based vacuum greases (Braycote 601 and 602 EF) performed the best with lowest friction and wear, the PAO-based high temperature grease, Rheolube 374A was moderate and MAC-based vacuum grease, Rheolube 2000 and the general-purpose terrestrial grease,

SKF LGMT2) performed the worst. The results from this study are a first step towards a comprehensive evaluation of the tribological performance of 60NiTi as a potential new bearing material for space applications with much better set of properties.

In the liquid lubricants approach, functionalized polyalkylmethacrylates (PAMAs) are investigated as multifunctional additives, i.e., as viscosity improvers, friction modifiers and anti-wear additives along with shear stability. Homopolymers of dodecyl methacrylate, 2-ethylhexyl methacrylate and co-polymers of functional methacrylates (polar) were studied for their friction and wear performance using unidirectional sliding friction and wear tests in a ball-on-disk configuration. It was found that these polymers were not only better than neat base oil but also were comparable to fully-formulated commercial benchmarks. Also, low molecular weight and enhanced polarity was found to be beneficial for wear reduction.

In the solid lubricant approach, the wear life of sputtered MoS<sub>2</sub> dry film lubricants, both undoped and Ni-doped, were evaluated and compared using unidirectional sliding friction tests and the wear mechanisms possibly responsible for the improved performance of Ni-doped MoS<sub>2</sub> were investigated using SEM, EDS, interferometry, and scratch adhesion testing. The results showed that Ni dopant at  $\approx 7\%$  by weight concentration improved wear life of MoS<sub>2</sub> coatings significantly at low contact pressures. SEM micrographs captured during the run-in process and scratch adhesion tests, strongly suggested that delamination driven wear in Ni-doped coatings provided longer lasting lubricious MoS<sub>2</sub> flakes as compared to cracked wear debris produced in undoped MoS<sub>2</sub> coating. Also, interestingly, irrespective of coating type, contact pressure and speed conditions, the wear depth was found to either exceed or was expected to exceed the coating thickness much earlier than the coating life values. Interferometry performed during run-in cycles indicated that, although the wear depth exceeded coating thickness quickly, the wear width wore much slowly, suggesting the lubrication was maintained by the sides of the wear track. The findings of this study illustrated that the wear life of MoS<sub>2</sub> coatings cannot be correlated to wear track depth, in contrast to the usual concept of wear for traditional engineering materials. Further, the results suggest a new mechanism by which dopants can extend MoS<sub>2</sub> DFL life, that is, facilitating delamination, that might be leveraged to further understand and then improve the performance of these coatings.

In summary, this dissertation aimed to employ different engineering techniques and fundamental studies to understand and improve the friction

and wear behavior of sliding contacts. The strategies discussed here targeted the three most important constituents of a tribo-contact i.e., the surfaces, the bulk material and lubricants that determine the mechanical efficiency of a system consisting of such contacts and in doing so, was able to discover that novel surface engineering techniques including UNSM and EP-UNSM, new materials including 60NiTi, multifunction liquid lubricant additives including low molecular weight PAMAs, dry film lubricants including Ni-doped MoS<sub>2</sub> are promising new avenues of further research that can push the boundaries of energy efficiency.

## 6.2 Future Work

### Damage Accumulation Model for MoS<sub>2</sub> DFLs

As discussed earlier, it is crucial to quantify the extent of coating degradation in DFL coated components during ground testing, which has a direct effect on the functional life of coating in space where it is expected to last the entire mission. The investigative study of the wear life of undoped and Ni-doped MoS<sub>2</sub> discussed in previous section, provided a close look at the wear behavior of these coatings in earth-ambient conditions at application specific load and speed parameters. More specifically, this study provided substantial evidence of cracking and delamination driven wear mode of sputtered undoped and Ni-doped MoS<sub>2</sub> coatings in the presence of atmospheric humidity and oxygen. Since these coatings are eventually used in vacuum of space, the effect of in-air testing on the subsequent wear performance in vacuum must be estimated in vacuum and their wear mechanisms investigated in order to potentially develop a coating damage model that can reliably predict coating wear life for a combined duty cycle of in-air and vacuum operation. Some work in this direction has been performed by European Space Agency (ESA) [131]. In this, the damage on MoS<sub>2</sub> coating due to in-air testing was assessed by measuring the change in coating wear life in vacuum after varying amounts in testing in air and the coating wear life (sputtered MoS<sub>2</sub> in bearings) continuously degraded with increasing operation in air. A hybrid lubrication approach was then proposed, where the coated components are plated with another fluid lubricant to act as a barrier to atmospheric oxygen and water vapor which are the key drivers for coating life degradation in earth ambient conditions. The fluid and solid lubricant complement each other depending on the environment, where the fluid protects the DFL and provides lubrication in ambient air conditions and the MoS<sub>2</sub> DFL takes over in vacuum of space.

However, a predictive model of coating life for in-air-followed-by-vacuum operations is much needed for a more reliable estimation of coating failure



which will advise better design criteria for space missions, where it may not be feasible to service components. To do this, we suggest a more systematic and fundamental tribological study to determine the coating wear modes and damage accumulation in vacuum after being subjected to sliding in air.



**Figure 6. 1.** (a) CAD Model of the controlled environment chamber. (b) Final assembly after retrofitting on tribometer including all peripherals.

Typically, an inert environment such as gaseous nitrogen, can act as a proxy for vacuum and is often used to perform such tests [140–147]. Since the tribometer used in this study was not readily capable of performing such testing in a controlled environment, we designed and developed an enclosure in-lab for this purpose, as shown in Figure 6.1. A pilot test revealed that the chamber worked as intended and a pin-on-disk sliding test in full nitrogen environment prolonged the coating life as expected (see Figure 6.2).

The interferometry data of the wear track from the nitrogen environment test after more than 200K cycles revealed, only 30% of the coating thickness was worn, see Figure 6.3. This is in stark contrast to the behavior observed earlier during ambient air testing where at the same load and speed conditions (300 MPa and  $1 \text{ ms}^{-1}$ ), the wear depth would be 100% of coating thickness in only  $\approx 1000$  cycles. This is an important observation from a failure prediction standpoint. Two types of damage accumulation can be proposed to occur in this scenario. One is the damage due to continuous and gradual wear of the coating, and the other, simultaneous wear and gradual buildup of fatigue at the coating-substrate interface eventually causing delamination of the coating.

Wear damage accumulation can be modeled by tracking the wear depth with increasing number of cycles.

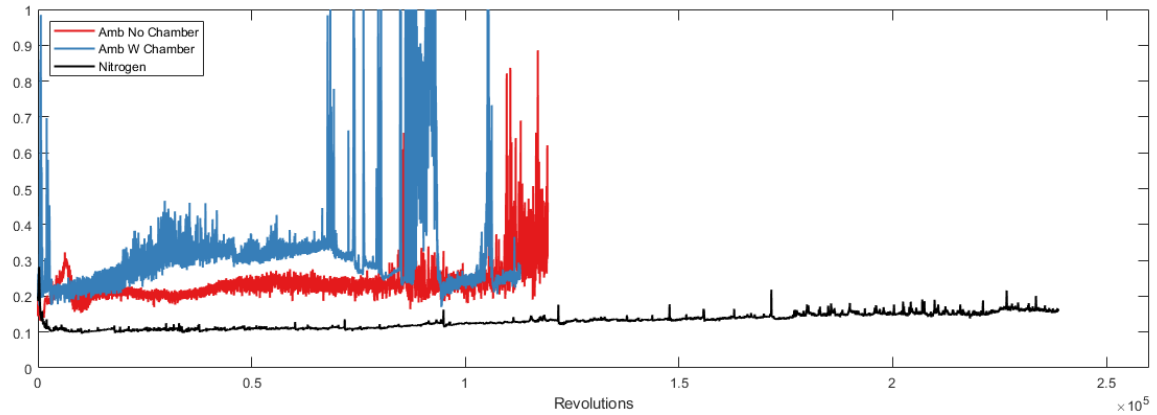


**Figure 6. 2.** Pin-on-disk sliding tests on Ni-doped MoS<sub>2</sub> showing the effect of nitrogen environment on the friction coefficient compared with ambient air tests with and without the chamber.

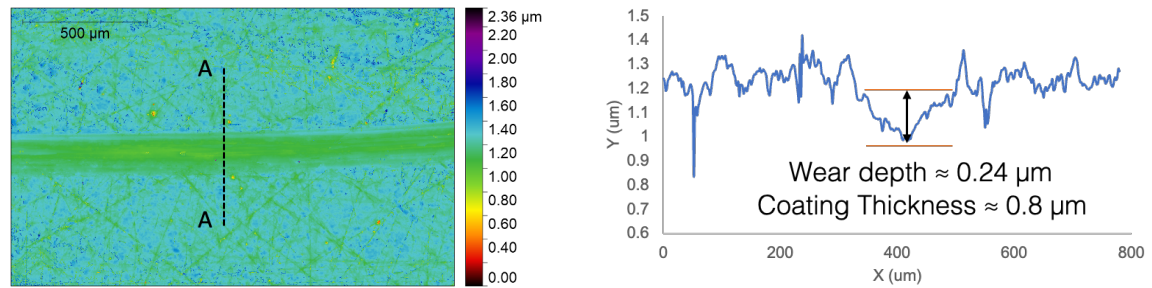


**Figure 6. 3.** Interferometry data of the wear track from nitrogen environment test showing wear depth after 200K cycles, in comparison to the coating thickness.

Fatigue damage accumulation on the other hand can be modeled using cumulative fatigue damage models used for metallic components. One of the most widely used fatigue damage models is the Palmgren-Miner's Rule [177], which assumes a linear accumulation of fatigue damage with number of stress cycles. The total accumulated damage is the summation of damage at each stress level which is defined as the ratio of number of cycles at a stress level to the number of cycles to failure at that stress level. And when this accumulated damage reaches unity, typically in ideal conditions, the component is predicted to fail.

There is already some ground-work done by another group in University of Florida regarding damage modeling in coatings [178]. It is explained in their work that in a continuous sliding contact, for example, an uncoated ball on a coated substrate, the coating may fail in three scenarios. One, due to interfacial



fatigue alone due to stress at the coating substrate interface, with almost no wear, causing delamination. Two, a combination of interfacial fatigue and gradual wear. And lastly, wear dominated failure with minimal interfacial fatigue, i.e., the coating is still bonded and just wears off like rubber on tires. A numerical model was developed to couple wear and fatigue accumulation to predict coating life using Miner's linear damage accumulation model. However, this model works well with coatings that wear gradually and fail due to fatigue accumulation.

So, we suggest that the failure mechanism of these MoS<sub>2</sub> coatings in nitrogen environment be investigated first, which requires that the coating be tested in nitrogen until failure. If the failure mode in nitrogen is delamination after gradual wear, then cumulative fatigue damage using Miner's rule could be used to predict coating life. The University of Florida study also found that the interfacial fatigue is a function of coating thickness, i.e., at a given contact stress, the interfacial stress exponentially increases with decreasing coating thickness. This is especially relevant because the coating thickness reduction due to sliding is much more gradual in nitrogen environment, so there is enough time for fatigue to buildup. However, if the failure mode is gradual abrasion of the coating without delamination, then the damage accumulation is only due to wear and can be modeled simply by wear rate estimation.

### **6.3 Concluding Remarks**

This dissertation has (a) demonstrated the use of experimental techniques for measuring the friction and wear performance of solid lubricants, liquid lubricants, greases and surface treatments using tribometry and interferometry, (b) demonstrated the use of electron microscopy, energy dispersive spectroscopy and mechanical testing techniques to investigate wear modes, wear mechanisms, and coating microstructure, (c) shown the applicability and viability of different approaches of optimizing a tribo-contact including, using low molecular weight polyalkylmethacrylates as multi-functional liquid lubricant additives that can function as both viscosity and friction modifiers; characterizing the tribological performance of a novel material, 60NiTi, which is stronger, harder and lighter than current bearing materials and doping MoS<sub>2</sub> DFLs with Ni for better coating wear life in space components.

Current materials used in bearings including steels and ceramics suffer from drawbacks which limit their applicability in space vehicles. 60NiTi is a relatively new material with excellent set of properties including corrosion resistance, hardenability, and large elastic range which makes it a potential

alternative to current bearing materials. This dissertation characterizes its friction and wear performance when lubricated with different greases including those used in space and provides a comprehensive set of data for 60NiTi that will facilitate use of this material for more and a wider variety of potential bearing applications.

Liquid lubricants consist of base oil and various additives each of which increase cost and complexity to formulate and make them. Multifunction additives consisting of polyalkylmethacrylates, developed by PNNL were studied in this dissertation and their viability as viscosity index improvers, friction modifiers and anti-wear additives is determined, which can lead to the development of more advanced lubricants with equal or better performance than current benchmarks and still be cheaper and easier to make.

Sputtered MoS<sub>2</sub> coatings are currently one of the most widely used DFLs in space mechanisms. However, these coatings are known to degrade in the presence of oxygen and water vapor, particularly encountered during ground testing, resulting in a reduced wear life in space where they are expected to operate. The tribological studies in this dissertation not only quantify the coating life enhancements achieved by doping MoS<sub>2</sub> with Ni, but also reveal the underlying mechanisms that possibly enable these enhancements. Also, this dissertation outlines a method to develop a damage accumulation model considering a combined in-air and inert environment duty cycle analogous to ground testing and space vacuum operation of coated components. This will allow more accurate prediction of coating life enabling the design and development of more reliable space mechanisms.

Our goals are already set towards a cleaner and greener future, and this requires further advancements in energy efficiency. Tribological interfaces are still a huge contributor to frictional and wear losses in mechanical systems and require novel and multipronged approach to improve mechanical efficiency. Every element of a tribo-contact i.e., the bulk material, lubricant and interacting surfaces is a unique avenue to improve tribological performance and the techniques studied, and potential solutions proposed in this dissertation can be applied in different mechanical systems ranging from automobiles to space vehicles to further improve their energy efficiency.

## References

1. Davison, C.St.C.: Wear prevention in early history. *Wear.* 1, 155–159 (1957). [https://doi.org/10.1016/0043-1648\(57\)90007-8](https://doi.org/10.1016/0043-1648(57)90007-8)
2. Fall, A., Weber, B., Pakpour, M., Lenoir, N., Shahidzadeh, N., Fiscina, J., Wagner, C., Bonn, D.: Sliding friction on wet and dry sand. *Physical Review Letters.* 112, (2014). <https://doi.org/10.1103/PhysRevLett.112.175502>
3. Holmberg, K., Erdemir, A.: Influence of tribology on global energy consumption, costs and emissions. *Friction.* 5, 263–284 (2017). <https://doi.org/10.1007/s40544-017-0183-5>
4. Bhushan, B.: Solid Surface Characterization. In: *Introduction to Tribology.* pp. 14–16. Wiley (2013)
5. Raja, J., Muralikrishnan, B., Fu, S.: Recent advances in separation of roughness, waviness and form. *Precision Engineering.* 26, 222–235 (2002). [https://doi.org/https://doi.org/10.1016/S0141-6359\(02\)00103-4](https://doi.org/https://doi.org/10.1016/S0141-6359(02)00103-4)
6. Bowden, F.P., Tabor, D.: *The Friction and Lubrication of Solids.* Oxford university press (2001)
7. Hokkirigawa, K., Kato, K.: *The Effect of Hardness on the Transition of the Abrasive Wear Mechanism of Steels.* (1988)
8. Archard, J.F.: Contact and rubbing of flat surfaces. *Journal of Applied Physics.* 24, 981–988 (1953). <https://doi.org/10.1063/1.1721448>
9. Wear patterns and laws of wear – a review | Zmitrowicz | *Journal of Theoretical and Applied Mechanics*, <http://www.ptmts.org.pl/jtam/index.php/jtam/article/view/v44n2p219/469>
10. Llavori, I., Zabala, A., Urchegui, M.A., Tato, W., Gómez, X.: A coupled crack initiation and propagation numerical procedure for combined fretting wear and fretting fatigue lifetime assessment. *Theoretical and Applied Fracture Mechanics.* 101, 294–305 (2019). <https://doi.org/10.1016/j.tafmec.2019.03.005>
11. Callister, W.D., David G. Rethwisch: *Surface Treatments.* In: *Material Science and Engineering: An Introduction.* pp. 263–undefined. Wiley (2009)

12. Faraji, G., Kim, H.S.: Review of principles and methods of severe plastic deformation for producing ultrafine-grained tubes, (2017)
13. Kramer, B.M.: Requirements For Wear-Resistant Coatings. (1983)
14. Luo, W., Selvadurai, U., Tillmann, W.: Effect of Residual Stress on the Wear Resistance of Thermal Spray Coatings. *Journal of Thermal Spray Technology*. 25, 321–330 (2016). <https://doi.org/10.1007/s11666-015-0309-0>
15. Korshunov, L.G., Noskova, N.I., Korznikov, A. v., Chernenko, N.L., Vil'Danova, N.F.: Effect of severe plastic deformation on the microstructure and tribological properties of a babbitt B83. *Physics of Metals and Metallography*. 108, 519–526 (2009). <https://doi.org/10.1134/S0031918X0911012X>
16. La, P., Ma, J., Zhu, Y.T., Yang, J., Liu, W., Xue, Q., Valiev, R.Z.: Dry-sliding tribological properties of ultrafine-grained Ti prepared by severe plastic deformation. *Acta Materialia*. 53, 5167–5173 (2005). <https://doi.org/10.1016/j.actamat.2005.07.031>
17. Rabinowicz, E.: Influence of surface energy on friction and wear phenomena. *Journal of Applied Physics*. 32, 1440–1444 (1961). <https://doi.org/10.1063/1.1728375>
18. Bhushan, B.: Free Surface Energy Theory of Adhesion. In: *Introduction to Tribology*. pp. 164–165. Wiley (2013)
19. Stott, F.H., Wood, G.C.: The influence of oxides on the friction and wear of alloys. *Tribology International*. 11, 211–218 (1978)
20. Khajeh, A., He, X., Yeon, J., Kim, S.H., Martini, A.: Mechanochemical Association Reaction of Interfacial Molecules Driven by Shear. *Langmuir*. 34, 5971–5977 (2018). <https://doi.org/10.1021/acs.langmuir.8b00315>
21. Friedrich, K.: Polymer composites for tribological applications. *Advanced Industrial and Engineering Polymer Research*. 1, 3–39 (2018). <https://doi.org/10.1016/j.aiepr.2018.05.001>
22. The adhesion of clean metals. *Proceedings of the Royal Society of London. Series A. Mathematical and Physical Sciences*. 233, 429–442 (1956). <https://doi.org/10.1098/rspa.1956.0001>

23. Ishigaki, H., Kawaguchi, I., Iwasa, M., Toibana, Y.: Friction and Wear of Hot Pressed Silicon Nitride and Other Ceramics. (1986)
24. Evans, A.G., Marshall, D.B.: Wear Mechanisms in Ceramics. In: Fundamentals of Friction and Wear of Materials. pp. 439–452. ASM International, Metals Park (1981)
25. Gesser, H.D.: Lubrication and Lubricants. In: Applied Chemistry: A Textbook for Engineers and Technologists. Springer US, Boston, MA (2002)
26. Booser, E.R.: CRC handbook of lubrication. Theory and practice of tribology. CRC Press Inc., Boca Raton, FL (1984)
27. Jones, M.H., Scott, D.: Industrial tribology: the practical aspects of friction, lubrication and wear. Elsevier, New York (1983)
28. Martini, A., Ramasamy, U.S., Len, M.: Review of Viscosity Modifier Lubricant Additives, (2018)
29. Wen, S., Huang, P.: Properties of Lubricants. In: Principles of Tribology. pp. 1–21. John Wiley & Sons, Ltd (2017)
30. Nosonovsky, M., Bhushan, B.: Multiscale friction mechanisms and hierarchical surfaces in nano- and bio-tribology, (2007)
31. Patton, S.T., Zabinski, J.S.: Failure mechanisms of a MEMS actuator in very high vacuum. (2002)
32. Borruto, A., Crivellone, G., Marani, F.: Influence of surface wettability on friction and wear tests. (1998)
33. Shizhu, W., Ping, H.: Solid Lubricants. In: Principles of Tribology. John Wiley & Sons, Ltd (2017)
34. Bowden, F.P., Tabor, D.: The Friction and Lubrication of Solids. Clarendon Press, Oxford (1986)
35. Scharf, T.W., Prasad, S. v.: Solid lubricants: a review. Journal of Materials Science. 48, 511–531 (2013). <https://doi.org/10.1007/s10853-012-7038-2>
36. Stoyanov, P., Strauss, H.W., Chromik, R.R.: Scaling effects between micro- and macro-tribology for a Ti-MoS<sub>2</sub> coating. Wear. 274–275, 149–161 (2012). <https://doi.org/10.1016/j.wear.2011.08.021>

37. Stoyanov, P., Chromik, R.R., Goldbaum, D., Lince, J.R., Zhang, X.: Microtribological performance of Au-MoS<sub>2</sub> and Ti-MoS<sub>2</sub> coatings with varying contact pressure. *Tribology Letters*. 40, 199–211 (2010). <https://doi.org/10.1007/s11249-010-9657-6>
38. Chromik, R., Wahl, K.: World tribology congress III. American Society of Mechanical Engineers. 829–830 (2005)
39. Wahl, K.J., Sawyer, W.G.: Observing Interfacial Sliding Processes in Solid-Solid Contacts.
40. Strauss, H.W., Chromik, R.R., Hassani, S., Klemberg-Sapieha, J.E.: In situ tribology of nanocomposite Ti-Si-C-H coatings prepared by PE-CVD. *Wear*. 272, 133–148 (2011). <https://doi.org/10.1016/j.wear.2011.08.001>
41. Singer, I.L., Dvorak, S.D., Wahl, K.J., Scharf, T.W.: Role of third bodies in friction and wear of protective coatings. *Journal of Vacuum Science & Technology A: Vacuum, Surfaces, and Films*. 21, S232–S240 (2003). <https://doi.org/10.1116/1.1599869>
42. Erdemir, A., Donnet, C.: Tribology of diamond-like carbon films: Recent progress and future prospects, (2006)
43. Rabinowicz, E.: Variation of friction and wear of solid lubricant films with film thickness. *ASLE Transactions*. 10, 1–9 (1967). <https://doi.org/10.1080/05698196708972159>
44. Smith, W.F., Hashemi, J.: Foundations of Materials Science and Engineering. McGraw-Hill (2006)
45. Valiev, R.Z., Islamgaliev, R.K., Alexandrov, I. v: Bulk nanostructured materials from severe plastic deformation.
46. Valiev, R.Z., Langdon, T.G.: Principles of equal-channel angular pressing as a processing tool for grain refinement, (2006)
47. Xu, C., Xia, K., Langdon, T.G.: The role of back pressure in the processing of pure aluminum by equal-channel angular pressing. *Acta Materialia*. 55, 2351–2360 (2007). <https://doi.org/10.1016/j.actamat.2006.11.036>
48. Zehetbauer, M.J., Stüwe, H.P., Vorhauer, A., Schafler, E., Kohout, J.: The role of hydrostatic pressure in severe plastic deformation. *Advanced Engineering Materials*. 5, 330–337 (2003). <https://doi.org/10.1002/adem.200310090>

49. Langdon, T.G.: The processing of ultrafine-grained materials through the application of severe plastic deformation. In: *Journal of Materials Science*. pp. 3388–3397 (2007)
50. Amanov, A., Cho, I.S., Pyoun, Y.S., Lee, C.S., Park, I.G.: Micro-dimpled surface by ultrasonic nanocrystal surface modification and its tribological effects. *Wear*. 286–287, 136–144 (2012). <https://doi.org/10.1016/J.WEAR.2011.06.001>
51. Wu, B., Wang, P., Pyoun, Y.S., Zhang, J., Murakami, R. ichi: Effect of ultrasonic nanocrystal surface modification on the fatigue behaviors of plasma-nitrided S45C steel. *Surface and Coatings Technology*. (2012). <https://doi.org/10.1016/j.surfcoat.2012.10.063>
52. Cao, X.J., Pyoun, Y.S., Murakami, R.: Fatigue properties of a S45C steel subjected to ultrasonic nanocrystal surface modification. *Applied Surface Science*. (2010). <https://doi.org/10.1016/j.apsusc.2010.04.007>
53. Ye, C., Zhou, X., Telang, A., Gao, H., Ren, Z., Qin, H., Suslov, S., Gill, A.S., Mannava, S.R., Qian, D., Doll, G.L., Martini, A., Sahai, N., Vasudevan, V.K.: Surface amorphization of NiTi alloy induced by Ultrasonic Nanocrystal Surface Modification for improved mechanical properties. *Journal of the Mechanical Behavior of Biomedical Materials*. 53, 455–462 (2016). <https://doi.org/10.1016/J.JMBBM.2015.09.005>
54. Liu, J., Suslov, S., Li, S., Qin, H., Ren, Z., Doll, G.L., Cong, H., Dong, Y., Ye, C.: Electrically Assisted Ultrasonic Nanocrystal Surface Modification of Ti6Al4V Alloy. *Advanced Engineering Materials*. (2018). <https://doi.org/10.1002/adem.201700470>
55. Amanov, A., Cho, I.S., Kim, D.E., Pyun, Y.S.: Fretting wear and friction reduction of CP titanium and Ti-6Al-4V alloy by ultrasonic nanocrystalline surface modification. *Surface and Coatings Technology*. (2012). <https://doi.org/10.1016/j.surfcoat.2012.06.046>
56. Gujba, A.K., Ren, Z., Dong, Y., Ye, C., Medraj, M.: Effect of ultrasonic nanocrystalline surface modification on the water droplet erosion performance of Ti[*sbnd*]6Al[*sbnd*]4V. *Surface and Coatings Technology*. (2016). <https://doi.org/10.1016/j.surfcoat.2016.08.054>
57. Zhang, H., Chiang, R., Qin, H., Ren, Z., Hou, X., Lin, D., Doll, G.L., Vasudevan, V.K., Dong, Y., Ye, C.: The effects of ultrasonic nanocrystal surface modification on the fatigue performance of 3D-printed Ti64.

- International Journal of Fatigue. (2017).  
<https://doi.org/10.1016/j.ijfatigue.2017.05.019>
58. Hou, X., Qin, H., Gao, H., Mankoci, S., Zhang, R., Zhou, X., Ren, Z., Doll, G.L., Martini, A., Sahai, N., Dong, Y., Ye, C.: A systematic study of mechanical properties, corrosion behavior and biocompatibility of AZ31B Mg alloy after ultrasonic nanocrystal surface modification. *Materials Science and Engineering C*. (2017).  
<https://doi.org/10.1016/j.msec.2017.04.128>
  59. Amanov, A., Penkov, O. v., Pyun, Y.S., Kim, D.E.: Effects of ultrasonic nanocrystalline surface modification on the tribological properties of AZ91D magnesium alloy. *Tribology International*. (2012).  
<https://doi.org/10.1016/j.triboint.2012.04.024>
  60. Ma, C., Qin, H., Ren, Z., O'Keeffe, S.C., Stevick, J., Doll, G.L., Dong, Y., Winiarski, B., Ye, C.: Increasing fracture strength in bulk metallic glasses using ultrasonic nanocrystal surface modification. *Journal of Alloys and Compounds*. (2017).  
<https://doi.org/10.1016/j.jallcom.2017.05.056>
  61. Farokhzadeh, K., Edrisy, A.: Fatigue improvement in low temperature plasma nitrided Ti-6Al-4V alloy. *Materials Science and Engineering A*. (2014). <https://doi.org/10.1016/j.msea.2014.10.008>
  62. Jamesh, M., Sankara Narayanan, T.S.N., Chu, P.K.: Thermal oxidation of titanium: Evaluation of corrosion resistance as a function of cooling rate. *Materials Chemistry and Physics*. (2013).  
<https://doi.org/10.1016/j.matchemphys.2012.12.020>
  63. Atar, E., Kayali, E.S., Cimenoglu, H.: Characteristics and wear performance of borided Ti6Al4V alloy. *Surface and Coatings Technology*. 202, 4583–4590 (2008).  
<https://doi.org/10.1016/J.SURFCOAT.2008.03.011>
  64. Malinov, S., Zhecheva, A., Sha, W.: Relation between the microstructure and properties of commercial titanium alloys and the parameters of gas nitriding. In: *Metal Science and Heat Treatment* (2004)
  65. Tokaji, K., Ogawa, T., Shibata, H.: The Effects of Gas Nitriding on Fatigue Behavior in Titanium and Titanium Alloys. *Journal of Materials Engineering and Performance*. (1999).  
<https://doi.org/10.1361/105994999770346990>



66. Lee, H.W., Kong, J.H., Lee, D.J., On, H.Y., Sung, J.H.: A study on high temperature gas nitriding and tempering heat treatment in 17Cr-1Ni-0.5C. *Materials and Design*. (2009). <https://doi.org/10.1016/j.matdes.2008.07.023>
67. Sarma, B., Ravi Chandran, K.S.: Recent advances in surface hardening of titanium. *JOM*. (2011). <https://doi.org/10.1007/s11837-011-0035-0>
68. Liu, J., Suslov, S., Vellore, A., Ren, Z., Amanov, A., Pyun, Y.S., Martini, A., Dong, Y., Ye, C.: Surface nanocrystallization by ultrasonic nanocrystal surface modification and its effect on gas nitriding of Ti6Al4V alloy. *Materials Science and Engineering A*. (2018). <https://doi.org/10.1016/j.msea.2018.08.089>
69. ASTM standards: G171 – 03:Standard Test Method for Scratch Hardness of Materials Using a Diamond Stylus. ASTM international. (2009). <https://doi.org/10.1520/G0171-03R09E02.2>
70. Ye, X., Yang, Y., Song, G., Tang, G.: Enhancement of ductility, weakening of anisotropy behavior and local recrystallization in cold-rolled Ti-6Al-4V alloy strips by high-density electropulsing treatment. *Applied Physics A*. 117, 2251–2264 (2014). <https://doi.org/10.1007/s00339-014-8655-1>
71. Tang, G., Zhang, J., Zheng, M., Zhang, J., Fang, W., Li, Q.: Experimental study of electroplastic effect on stainless steel wire 304L. *Materials Science and Engineering: A*. (2000). [https://doi.org/10.1016/S0921-5093\(99\)00708-X](https://doi.org/10.1016/S0921-5093(99)00708-X)
72. Xu, Z., Tang, G., Tian, S., Ding, F., Tian, H.: Research of electroplastic rolling of AZ31 Mg alloy strip. *Journal of Materials Processing Technology*. (2007). <https://doi.org/10.1016/j.jmatprotec.2006.07.019>
73. Stolyarov, V. V.: Structure Refinement and Electropulse Current Effect on Mechanical Properties of Shape Memory TiNi Alloy. *Materials Science Forum*. (2009). <https://doi.org/10.4028/www.scientific.net/msf.633-634.595>
74. Ye, Y., Kuang, J., Kure-Chu, S.Z., Song, G., Sun, Z., Tang, G.: Improvement of microstructure and surface behaviors of welded S50C steel components under electropulsing assisted ultrasonic surface modification. *Journal of Materials Research*. (2016). <https://doi.org/10.1557/jmr.2016.127>

75. Gromov, V.E., Ivanov, Y.F., Stolboushkina, O.A., Konovalov, S. V.: Dislocation substructure evolution on Al creep under the action of the weak electric potential. *Materials Science and Engineering A*. (2010). <https://doi.org/10.1016/j.msea.2009.10.045>
76. Ye, X., Liu, T., Ye, Y., Wang, H., Tang, G., Song, G.: Enhanced grain refinement and microhardness of Ti-Al-V alloy by electropulsing ultrasonic shock. *Journal of Alloys and Compounds*. (2015). <https://doi.org/10.1016/j.jallcom.2014.09.192>
77. Kato, K., and Adachi, K.: Wear Mechanisms. In: *Modern Tribology Handbook*, Bharat Bhushan. pp. 273–299 (2001)
78. Atkins, A.G.: Slice-push, formation of grooves and the scale effect in cutting. *Interface Focus*. 6, (2016). <https://doi.org/10.1098/rsfs.2016.0019>
79. Moore, M.A.: The relationship between the abrasive wear resistance, hardness and microstructure of ferritic materials. *Wear*. 28, 59–68 (1974). [https://doi.org/10.1016/0043-1648\(74\)90101-X](https://doi.org/10.1016/0043-1648(74)90101-X)
80. Reshetnyak, H., Kuybarsepp, J.: Mechanical properties of hard metals and their erosive wear resistance. *Wear*. 177, 185–193 (1994). [https://doi.org/10.1016/0043-1648\(94\)90244-5](https://doi.org/10.1016/0043-1648(94)90244-5)
81. Farhat, Z.N., Ding, Y., Northwood, D.O., Alpas, A.T.: Effect of grain size on friction and wear of nanocrystalline aluminum. *Materials Science and Engineering: A*. 206, 302–313 (1996). [https://doi.org/10.1016/0921-5093\(95\)10016-4](https://doi.org/10.1016/0921-5093(95)10016-4)
82. Haque, M.M., Sharif, A.: Study on wear properties of aluminium–silicon piston alloy. *Journal of Materials Processing Technology*. 118, 69–73 (2001). [https://doi.org/10.1016/S0924-0136\(01\)00869-X](https://doi.org/10.1016/S0924-0136(01)00869-X)
83. Ye, H.: An Overview of the Development of Al-Si-Alloy Based Material for Engine Applications. *Journal of Materials Engineering and Performance*. 12, 288–297 (2003). <https://doi.org/10.1361/105994903770343132>
84. Dienwiebel, M., Pöhlmann, K., Scherge, M.: Origins of the wear resistance of AlSi cylinder bore surfaces studies by surface analytical tools. *Tribology International*. 40, 1597–1602 (2007). <https://doi.org/10.1016/J.TRIBOINT.2007.01.015>
85. Voevodin, A.A., Zabinski, J.S.: Nanocomposite and nanostructured tribological materials for space applications. *Composites Science and*

- Technology. 65, 741–748 (2005).  
<https://doi.org/10.1016/J.COMPSCITECH.2004.10.008>
86. Ingole, S.: 60NiTi Alloy for Tribological and Biomedical Surface Engineering Applications. *J. Miner, Met. Mater. Soc.* 65, 792–798 (2013).  
<https://doi.org/10.1007/s11837-013-0610-7>
  87. DellaCorte, C., Noebe, R.D., Stanford, M.K., Padula, S.A.: Resilient and Corrosion-proof Rolling Element Bearings Made from Superelastic Ni-Ti Alloys for Aerospace Mechanism Applications. In: *Rolling Element Bearings*. pp. 143–166. ASTM International (2012)
  88. DellaCorte, C., Pepper, S. V., Noebe, R., Hull, D.R., Glennon, G.: Intermetallic Nickel-Titanium Alloys for Oil-Lubricated Bearing Applications. NASA Technical Reports Server. (2009)
  89. ZENG, Q., DONG, G.: Superlubricity behaviors of Nitinol 60 alloy under oil lubrication. *Transactions of Nonferrous Metals Society of China.* 24, 354–359 (2014). [https://doi.org/10.1016/S1003-6326\(14\)63068-5](https://doi.org/10.1016/S1003-6326(14)63068-5)
  90. Zeng, Q., Dong, G., Martin, J.M.: Green superlubricity of Nitinol 60 alloy against steel in presence of castor oil. *Scientific Reports.* 6, 29992 (2016).  
<https://doi.org/10.1038/srep29992>
  91. Zeng, Q., Dong, G.: Influence of Load and Sliding Speed on Super-Low Friction of Nitinol 60 Alloy under Castor Oil Lubrication. *Tribology Letters.* 52, 47–55 (2013). <https://doi.org/10.1007/s11249-013-0191-1>
  92. Walters, N., Martini, A.: Friction Dependence on Surface Roughness for Castor Oil Lubricated NiTi Alloy Sliding on Steel. *Tribology Transactions.* 1–5 (2018).  
<https://doi.org/10.1080/10402004.2018.1520949>
  93. Zeng, Q., Zhao, X., Dong, G., Wu, H.: Lubrication properties of Nitinol 60 alloy used as high-speed rolling bearing and numerical simulation of flow pattern of oil-air lubrication. *Transactions of Nonferrous Metals Society of China.* 22, 2431–2438 (2012). [https://doi.org/10.1016/S1003-6326\(11\)61481-7](https://doi.org/10.1016/S1003-6326(11)61481-7)
  94. Khanlari, K., Ramezani, M., Kelly, P., Cao, P., Neitzert, T.: Comparison of the reciprocating sliding wear of 58Ni39Ti-3Hf alloy and baseline 60NiTi. *Wear.* 408–409, 120–130 (2018).  
<https://doi.org/10.1016/j.wear.2018.05.011>

95. Khanlari, K., Ramezani, M., Kelly, P., Cao, P., Neitzert, T.: Reciprocating Sliding Wear Behavior of 60NiTi As Compared to 440C Steel under Lubricated and Unlubricated Conditions. *Tribology Transactions*. 1–11 (2018). <https://doi.org/10.1080/10402004.2018.1460434>
96. Khanlari, K., Ramezani, M., Kelly, P., Cao, P., Neitzert, T.: An Investigation on Reasons Causing Inferiority in Unlubricated Sliding Wear Performance of 60NiTi as Compared to 440C Steel. *Tribology Transactions*. 1–14 (2018). <https://doi.org/10.1080/10402004.2018.1516326>
97. DellaCorte, Christopher: Nickel-Titanium Alloys: Corrosion. NASA Technical Reports Server. (2010)
98. Pepper, S. V., DellaCorte, C., Noebe, R.D., Hall, D.R., Glennon, G.: Nitinol 60 as a Material For Spacecraft Triboelements. NASA Technical Reports Server. (2009)
99. Pepper, S. V., DellaCorte, C., Glennon, G.: Lubrication of Nitinol 60. NASA Technical Reports Server. (2010)
100. Stanford, M.K.: Friction and Wear of Unlubricated NiTiHf With Nitriding Surface Treatments. NASA Technical Reports Server. (2018)
101. Bhushan, B.: Types of Wear Mechanism. In: *Introduction to Tribology*. pp. 372, 2nd Edition
102. Roberts, R.W., Owens, R.S.: Titanium Lubrication. *Nature*. 200, 357–358 (1963). <https://doi.org/10.1038/200357a0>
103. Poon, S.Y.: An Experimental Study of Grease in Elastohydrodynamic Lubrication. *Journal of Lubrication Technology*. 94, 27 (1972). <https://doi.org/10.1115/1.3451631>
104. Wilson, A.R.: The Relative Thickness of Grease and Oil Films in Rolling Bearings. *Proceedings of the Institution of Mechanical Engineers*. 193, 185–192 (1979). [https://doi.org/10.1243/PIME\\_PROC\\_1979\\_193\\_019\\_02](https://doi.org/10.1243/PIME_PROC_1979_193_019_02)
105. Wikström, V., Jacobson, B.: Loss of lubricant from oil-lubricated near-starved spherical roller bearings. *Proceedings of the Institution of Mechanical Engineers, Part J: Journal of Engineering Tribology*. 211, 51–66 (1997). <https://doi.org/10.1243/1350650971542318>

106. Lugt, P.M.: A Review on Grease Lubrication in Rolling Bearings. *Tribology Transactions*. 52, 470–480 (2009). <https://doi.org/10.1080/10402000802687940>
107. Pirro, D.M., Wessol, A.A.: *Lubrication Fundamentals*, Second Edition. (2001)
108. Spikes, H.: Friction Modifier Additives. *Tribology Letters*. 60, (2015). <https://doi.org/10.1007/s11249-015-0589-z>
109. Munch, M.R., Gast, A.P.: A study of block copolymer adsorption kinetics via internal reflection interferometry. *Journal of the Chemical Society, Faraday Transactions*. 86, 1341 (1990). <https://doi.org/10.1039/ft9908601341>
110. Chevalier, Y., Fixari, B., Brunel, S., Marie, E., De Guio, P.: Review: The adsorption of functional polymers from their organic solutions: applications to fuel additives. *Polymer International*. 53, 475–483 (2004). <https://doi.org/10.1002/pi.1438>
111. Chen, M., Briscoe, W.H., Armes, S.P., Cohen, H., Klein, J.: Polyzwitterionic brushes: Extreme lubrication by design. *European Polymer Journal*. 47, 511–523 (2011). <https://doi.org/10.1016/J.EURPOLYMJ.2010.10.007>
112. Cosimbescu, L., Robinson, J.W., Zhou, Y., Qu, J.: Dual functional star polymers for lubricants. *RSC Advances*. 6, 86259–86268 (2016). <https://doi.org/10.1039/C6RA17461B>
113. Kim, C.A., Kim, J.T., Lee, K., Choi, H.J., Jhon, M.S.: Mechanical degradation of dilute polymer solutions under turbulent flow. *Polymer*. 41, 7611–7615 (2000)
114. Jeong, S.H., Kim, J.M., Baig, C.: Rheological Influence of Short-Chain Branching for Polymeric Materials under Shear with Variable Branch Density and Branching Architecture. *Macromolecules*. 50, 4491–4500 (2017). <https://doi.org/10.1021/acs.macromol.7b00544>
115. Thomas, J.Z., He, Y., Delferro, M., Shiller, P., Doll, G., Dehkordi, B.L., Ren, N., Lockwood, F., Marks, T.J., Chung, Y.W., Greco, A., Erdemir, A., Wang, Q.: Investigation of shear-Thinning behavior on film thickness and friction coefficient of polyalphaolefin base fluids with varying olefin copolymer content. *Journal of Tribology*. 139, (2017). <https://doi.org/10.1115/1.4033716>

116. Marx, N., Ponjavic, A., Taylor, R.I., Spikes, H.A.: Study of Permanent Shear Thinning of VM Polymer Solutions. *Tribology Letters*. 65, 106 (2017). <https://doi.org/10.1007/s11249-017-0888-7>
117. Wang, J., Ye, Z., Zhu, S.: Topology-engineered hyperbranched high-molecular-weight polyethylenes as lubricant viscosity-index improvers of high shear stability. *Industrial and Engineering Chemistry Research*. 46, 1174–1178 (2007). <https://doi.org/10.1021/ie0613624>
118. Covitch, M.J.: How Polymer Architecture Affects Permanent Viscosity Loss of Multigrade Lubricants. In: *International Fall Fuels and Lubricants Meeting and Exposition*. SAE International (1998)
119. Singh, R.K., Kukrety, A., Kumar, A., Chouhan, A., Saxena, R.C., Ray, S.S., Jain, S.L.: Synthesis, characterization, and performance evaluation of N,N-Dimethylacrylamide–alkyl acrylate copolymers as novel multifunctional additives for lube oil. *Advances in Polymer Technology*. 37, 1695–1702 (2018). <https://doi.org/10.1002/adv.21826>
120. Müller, M., Fan, J., Spikes, H.: Design of Functionalized PAMA Viscosity Modifiers to Reduce Friction and Wear in Lubricating Oils. *Journal of ASTM International*. 4, (2007)
121. Benedet, J., Green, J.H., Lamb, G.D., Spikes, H.A.: Spurious Mild Wear Measurement Using White Light Interference Microscopy in the Presence of Antiwear Films. *Tribology Transactions*. 52, 841–846 (2009). <https://doi.org/10.1080/10402000903180696>
122. Anghel, V., Bovington, C., Spikes, H.A.: Thick-boundary-film formation by friction modifier additives. *Lubrication Science*. 11, 313–335 (1999). <https://doi.org/10.1002/lc.3010110402>
123. Donnet, C., Erdemir, A.: Solid Lubricant Coatings: Recent Developments and Future Trends. *Tribology Letters*. 17, 389–397 (2004). <https://doi.org/10.1023/B:TRIL.0000044487.32514.1d>
124. Braithwaite, E.: Graphite and Molybdenum Disulphide. In: *Solid Lubricants and Surfaces*. pp. 139–undefined. Clarendon Press, Oxford (1964)
125. SKINNER, J., GANE, N., TABOR, D.: Micro-friction of Graphite. *Nature Physical Science*. 232, 195–196 (1971). <https://doi.org/10.1038/physci232195a0>

126. Briscoe, B.J., Tabor, D.: The effect of pressure on the frictional properties of polymers. Elsevier Sequoia S.A (1975)
127. Tanaka, K., Uchiyama, Y., Toyooka, S.: The mechanism of wear of polytetrafluoroethylene. (1973)
128. Liew, K.W., Kong, H.J., Low, K.O., Kok, C.K., Lee, D.: The effect of heat treatment duration on mechanical and tribological characteristics of Ni-P-PTFE coating on low carbon high tensile steel. *Materials and Design*. 62, 430–442 (2014). <https://doi.org/10.1016/j.matdes.2014.05.047>
129. Polcar, T., Cavaleiro, A.: Self-adaptive low friction coatings based on transition metal dichalcogenides. *Thin Solid Films*. 519, 4037–4044 (2011). <https://doi.org/10.1016/j.tsf.2011.01.180>
130. Fleischauer, P.D.: Fundamental aspects of the electronic structure, materials properties and lubrication performance of sputtered MoS<sub>2</sub> films. (1987)
131. Buttery, M., Lewis, S., Kent, A., Bingley, R., Cropper, M.: Long-Term Storage Considerations for Spacecraft Lubricants. *Lubricants*. 8, 32 (2020). <https://doi.org/10.3390/lubricants8030032>
132. Killeffer, D.H., Linz, A.: Molybdenum Compounds, Their Chemistry and Technology. Interscience Publishers (1952)
133. Vazirisereshk, M.R., Martini, A., Strubbe, D.A., Baykara, M.Z.: Solid lubrication with MoS<sub>2</sub>: A review. *Lubricants*. 7, 57 (2019)
134. Song, I., Park, C., Choi, H.C.: Synthesis and properties of molybdenum disulphide: from bulk to atomic layers. *RSC Adv*. 5, 7495–7514 (2015)
135. Lince, J.R.: Solid Lubricants. In: Conley, P.L. (ed.) *Space Vehicle Mechanisms: Elements of Successful Design*. p. 153. John Wiley & Sons (1998)
136. Roberts, E.W.: Ultralow friction films of MoS<sub>2</sub> for space applications. *Thin Solid Films*. 181, 461–473 (1989)
137. Fleischauer, P.D.: Fundamental aspects of the electronic structure, materials properties and lubrication performance of sputtered MoS<sub>2</sub> films. *Thin Solid Films*. 154, 309–322 (1987)
138. Roberts, E.W.: Towards an optimised sputtered MoS<sub>2</sub> lubricant film. NASA. Lewis Research Center 20th Aerospace Mechanics Symposium . 103–119 (1986)

139. Hilton, M.R., Bauer, R., Fleischauer, P.D.: Tribological performance and deformation of sputter-deposited MoS<sub>2</sub> solid lubricant films during sliding wear and indentation contact. *Thin Solid Films*. 188, 219–236 (1990)
140. Li, H., Xu, T., Wang, C., Chen, J., Zhou, H., Liu, H.: Effect of relative humidity on the tribological properties of hydrogenated diamond-like carbon films in a nitrogen environment. *J. Phys. D: Appl. Phys.* 38, 62 (2004)
141. Zabinski, J.S., Donley, M.S., Walck, S.D., Schneider, T.R., McDevitt, N.T.: The effects of dopants on the chemistry and tribology of sputter-deposited MoS<sub>2</sub> films. *Tribol. Trans.* 38, 894–904 (1995)
142. Khare, H.S., Burris, D.L.: The effects of environmental water and oxygen on the temperature-dependent friction of sputtered molybdenum disulfide. *Tribol. Lett.* 52, 485–493 (2013)
143. Voevodin, A.A., O'Neill, J.P., Zabinski, J.S.: Nanocomposite tribological coatings for aerospace applications. *Surf. Coat. Tech.* 116, 36–45 (1999)
144. Voevodin, A.A., Zabinski, J.S.: Nanocomposite and nanostructured tribological materials for space applications. *Compos. Sci. Technol.* 65, 741–748 (2005)
145. Voevodin, A.A., Fitz, T.A., Hu, J.J., Zabinski, J.S.: Nanocomposite tribological coatings with “chameleon” surface adaptation. *J. Vac. Sci. Technol. A* 20, 1434–1444 (2002)
146. Curry, J.F., Argibay, N., Babuska, T., Nation, B., Martini, A., Strandwitz, N.C., Dugger, M.T., Krick, B.A.: Highly Oriented Mo<sub>2</sub> Coatings: Tribology and Environmental Stability. *Tribol. Lett.* 64, 11 (2016)
147. Serles, P., Sun, H., Colas, G., Tam, J., Nicholson, E., Wang, G., Howe, J., Saulot, A., Singh, C.V., Filleter, T.: Structure-Dependent Wear and Shear Mechanics of Nanostructured MoS<sub>2</sub> Coatings. *Advanced Materials Interfaces*. 1901870 (2020)
148. John, P.J., Cutler, J.N., Sanders, J.H.: Tribological behavior of a multialkylated cyclopentane oil under ultrahigh vacuum conditions. *Tribol. Lett.* 9, 167–173 (2001)
149. Donnet, C., Martin, J.M., le Mogne, Th., Belin, M.: Super-low friction of MoS<sub>2</sub> coatings in various environments. *Tribol. Int.* 29, 123–128 (1996)



150. Liang, T., Sawyer, W.G., Perry, S.S., Sinnott, S.B., Phillpot, S.R.: Energetics of oxidation in MoS<sub>2</sub> nanoparticles by density functional theory. *J. Phys. Chem. C*. 115, 10606–10616 (2011)
151. Ross, S., Sussman, A.: Surface oxidation of molybdenum disulfide. *J. Phys. Chem.* 59, 889–892 (1955)
152. Haltner, A.J., Oliver, C.S.: Effect of water vapor on friction of molybdenum disulfide. *Ind. Eng. Chem. Fund.* 5, 348–355 (1966)
153. Pardee, R.P.: The effect of humidity on low-load frictional properties of a bonded solid film lubricant. *ASLE Trans.* 15, 130–142 (1972)
154. Panitz, J.K.G., Pope, L.E., Lyons, J.E., Staley, D.J.: The tribological properties of MoS<sub>2</sub> coatings in vacuum, low relative humidity, and high relative humidity environments. *J. Vac. Sci. Technol. A*. 6, 1166–1170 (1988)
155. Curry, J.F., Wilson, M.A., Luftman, H.S., Strandwitz, N.C., Argibay, N., Chandross, M., Sidebottom, M.A., Krick, B.A.: Impact of microstructure on MoS<sub>2</sub> oxidation and friction. *ACS Appl. Mater. Inter.* 9, 28019–28026 (2017)
156. Uemura, M., Saito, K., Nakao, K.: A mechanism of vapor effect on friction coefficient of molybdenum disulfide. *Tribol. Trans.* 33, 551–556 (1990)
157. Levita, G., Righi, M.C.: Effects of water intercalation and tribochemistry on MoS<sub>2</sub> lubricity: an ab initio molecular dynamics investigation. *Chem. Phys. Chem.* 18, 1475–1480 (2017)
158. Haider, J.: MoS<sub>x</sub> Coatings by Closed-Field Magnetron Sputtering. In: Wang Q. Jane and Chung, Y.-W. (ed.) *Encyclopedia of Tribology*. pp. 2323–2333. Springer US, Boston, MA (2013)
159. Spalvins, T.: Morphological and frictional behavior of sputtered MoS<sub>2</sub> films. *Thin Solid Films*. 96, 17–24 (1982)
160. Buck, V.: Morphological properties of sputtered MoS<sub>2</sub> films. *Wear*. 91, 281–288 (1983)
161. Spalvins, T.: A review of recent advances in solid film lubrication. *J. Vac. Sci. Technol. A*. 5, 212–219 (1987)
162. Simmonds, M.C., Savan, A., Pflüger, E., van Swygenhoven, H.: Mechanical and tribological performance of MoS<sub>2</sub> co-sputtered composites. *Surf. Coat. Tech.* 126, 15–24 (2000)

163. Nainaparampil, J.J., Phani, A.R., Krzanowski, J.E., Zabinski, J.S.: Pulsed laser-ablated MoS<sub>2</sub>-Al films: friction and wear in humid conditions. *Surf. Coat. Tech.* 187, 326–335 (2004)
164. Renevier, N.M., Fox, V.C., Teer, D.G., Hampshire, J.: Coating characteristics and tribological properties of sputter-deposited MoS<sub>2</sub>/metal composite coatings deposited by closed field unbalanced magnetron sputter ion plating. *Surf. Coat. Tech.* 127, 24–37 (2000)
165. Teer, D.G.: New solid lubricant coatings. *Wear.* 251, 1068–1074 (2001)
166. Tedstone, A.A., Lewis, D.J., O'Brien, P.: Synthesis, properties, and applications of transition metal-doped layered transition metal dichalcogenides. *Chem. Mater.* 28, 1965–1974 (2016)
167. Ye, M., Zhang, G., Ba, Y., Wang, T., Wang, X., Liu, Z.: Microstructure and tribological properties of MoS<sub>2</sub>+ Zr composite coatings in high humidity environment. *Appl. Surf. Sci.* 367, 140–146 (2016)
168. Stoyanov, P., Chromik, R.R., Goldbaum, D., Lince, J.R., Zhang, X.: Microtribological performance of Au-MoS<sub>2</sub> and Ti-MoS<sub>2</sub> coatings with varying contact pressure. *Tribol. Lett.* 40, 199–211 (2010)
169. Paul, A., Singh, H., Mutyala, K.C., Doll, G.L.: An improved solid lubricant for bearings operating in space and terrestrial environments. In: 44th Aerospace Mechanisms Symposium. p. 141 (2018)
170. Li, H., Li, X., Zhang, G., Wang, L., Wu, G.: Exploring the Tribophysics and Tribochemistry of MoS<sub>2</sub> by Sliding MoS<sub>2</sub>/Ti Composite Coating Under Different Humidity. *Tribol. Lett.* 65, 38 (2017)
171. Stupp, B.C.: Synergistic effects of metals co-sputtered with MoS<sub>2</sub>. *Thin Solid Films.* 84, 257–266 (1981)
172. Lince, J.R.: Doped MoS<sub>2</sub> Coatings and Their Tribology. In: Wang Q. J. and Chung, Y.-W. (ed.) *Encyclopedia of Tribology*. pp. 782–785. Springer US, Boston, MA (2013)
173. Hamilton, M.A., Alvarez, L.A., Mauntler, N.A., Argibay, N., Colbert, R., Burris, D.L., Muratore, C., Voevodin, A.A., Perry, S.S., Sawyer, W.G.: A possible link between macroscopic wear and temperature dependent friction behaviors of MoS<sub>2</sub> coatings. *Tribol. Lett.* 32, 91–98 (2008)

174. Hilton, M.R., Jayaram, G., Marks, L.D.: Microstructure of cosputter-deposited metal-and oxide-MoS<sub>2</sub> solid lubricant thin films. *J. Mater. Res.* 13, 1022–1032 (1998)
175. Hilton, M.R.: Fracture in MoS<sub>2</sub> solid lubricant films. *Surf. Coat. Tech.* 68, 407–415 (1994)
176. Zabinski, J.S., Donley, M.S., Walck, S.D., Schneider, T.R., McDevitt, N.T.: The effects of dopants on the chemistry and tribology of sputter-deposited MoS<sub>2</sub>films. *Tribology Transactions.* 38, 894–904 (1995). <https://doi.org/10.1080/10402009508983486>
177. Leiva, V., Saunders, S.C.: Cumulative Damage Models. In: Wiley StatsRef: Statistics Reference Online. pp. 1–10. John Wiley & Sons, Ltd, Chichester, UK (2015)
178. McCook, N.L., Burris, D.L., Kim, N.H., Sawyer, W.G.: Cumulative damage modeling of solid lubricant coatings that experience wear and interfacial fatigue. *Wear.* 262, 1490–1495 (2007). <https://doi.org/10.1016/j.wear.2007.01.042>